



**Fakultät für Medizin**

**Molekulare Kardiologie**

**I. Medizinische Klinik und Poliklinik**

**Klinikum rechts der Isar**

# **Advanced hiPSC-based platforms for in vitro modeling of cardiac development, disease, and therapy**

**Anna Béatrice Meier**

Vollständiger Abdruck der von der Fakultät für Medizin der Technischen Universität München zur Erlangung des akademischen Grades eines

**Doctor of Philosophy (Ph.D.)**

genehmigten Dissertation.

**Vorsitzende/r:** Prof. Dr. Stefan Lichtenthaler

**Betreuer/in:** Prof. Dr. Alessandra Moretti

**Prüfer der Dissertation:**

1. Prof. Dr. Karl-Ludwig Laugwitz
2. Prof. Dr. Dieter Saur
3. Prof. Dr. Martin Biel

Die Dissertation wurde am 05.10.2021 bei der Fakultät für Medizin der Technischen Universität München eingereicht und durch die Fakultät für Medizin am 30.12.2021 angenommen.



# Abstract

Cardiovascular disease (CVD) encompasses a group of disorders of the heart and blood vessels that, collectively, are the leading cause of death and a major contributor to disability worldwide. Despite the significant public health burden of CVD, the development of new treatments for both acquired and inherited cardiovascular disorders has stagnated over the past two decades. A recurring issue is the difficulty of translating preclinical findings into safe and effective therapies. This is mainly due to the fact that commonly used preclinical models do not faithfully recapitulate human (patho)physiology. Most studies of cardiac development, function, and disease are based on animals and particularly rodents, but it can be misleading to extrapolate these results to humans. On the other hand, in vitro cell culture models have long suffered from low predictive value.

Human pluripotent stem cells have emerged as a promising alternative to generate in vitro models of higher physiological relevance. In particular, so-called human induced pluripotent stem cells (hiPSCs) that can be reprogrammed from the somatic cells of any healthy or diseased individual allow the study of disease mechanisms in defined genetic contexts. Importantly, hiPSCs have the potential to form organoids, which are self-organized microtissues resembling an organ of the body in terms of cell composition, architecture, and function. Organoids of most organs including the intestine, brain, kidney, lung, liver, and retina have already proved to be powerful tools for disease modeling, drug discovery, and personalized therapy. However, bona fide heart organoids composed of the three cardiac layers of myocardium, endocardium, and epicardium have not yet been reported. In this work, we established the first hiPSC-derived 3D cardiac models showing self-organization of myocardial and epicardial layers, which we named ‘epicardioids’. We could demonstrate that epicardioids contain all key cardiac cell types and recapitulate the morphological and functional self-patterning typical of the ventricular wall. In a proof-of-concept study, the utility of epicardioids for disease modeling was illustrated by the hypertrophic and fibrotic response to endothelin-1 treatment.

Recent advances in CRISPR/Cas9 gene editing have further expanded the spectrum of applications in biomedical research. In particular, there is renewed hope that gene therapy could treat and potentially cure CVDs, including by correction of mutations causing inherited diseases. In collaboration with Prof. Christian Kupatt, we established a novel gene therapy

approach to treat Duchenne muscular dystrophy (DMD), a fatal disease caused by the loss of the dystrophin protein due to frameshift mutations in the *DMD* gene. In DMD, loss of dystrophin leads to progressive muscle degeneration and premature death due to respiratory and cardiac failure. In parallel to investigations in a large animal model, we showed that a dual adeno-associated virus (AAV) system encoding a split-intein Cas9 and two guide RNAs could efficiently edit cardiomyocytes derived from DMD patient hiPSCs, leading to the restoration of dystrophin and the amelioration of calcium handling defects. Having demonstrated the potential therapeutic benefit of this approach, epicardioids would represent an ideal platform for further in vitro testing of efficacy, safety, and cell specificity in a tissue-like context.

More broadly, the converging technologies brought forward in this work – organoids and somatic gene editing – offer new opportunities to push the boundaries of both basic and translational cardiovascular research.

# Zusammenfassung

Herz-Kreislauf-Erkrankungen sind eine Gruppe von Erkrankungen des Herzens und der Blutgefäße, die weltweit die häufigste Todesursache darstellen und in hohem Maße zu Behinderungen beitragen. Trotz der erheblichen Belastung der öffentlichen Gesundheit durch Herz-Kreislauf-Erkrankungen ist die Entwicklung neuer Therapien sowohl für erworbene als auch für vererbte Herz-Kreislauf-Erkrankungen in den letzten zwei Jahrzehnten weitgehend begrenzt geblieben. Ein immer wiederkehrendes Problem ist die Schwierigkeit, präklinische Erkenntnisse in sichere und wirksame Therapien umzusetzen. Dies ist vor allem darauf zurückzuführen, dass die aktuell verwendeten präklinischen Modelle die menschliche (Patho-)Physiologie nicht getreu nachbilden. Die meisten Studien zur Entwicklung, Funktion und Erkrankung des Herzens basieren auf Tieren, insbesondere auf Nagetieren, aber es kann schwierig sein, diese Ergebnisse auf den Menschen zu übertragen. Andererseits hatten In-vitro-Zellkulturmodelle lange Zeit einen geringen Vorhersagewert.

Humane pluripotente Stammzellen haben sich als vielversprechende Alternative zur Erzeugung von In-vitro-Modellen mit höherer physiologischer Relevanz erwiesen. Insbesondere sogenannte humane induzierte pluripotente Stammzellen (hiPSCs), die aus den somatischen Zellen jedes gesunden oder kranken Individuums reprogrammiert werden können, ermöglichen die Untersuchung von Krankheitsmechanismen in definierten genetischen Kontexten. hiPSCs haben außerdem das Potenzial, Organoiden zu bilden, d. h. selbstorganisierte Mikrogewebe, die in Bezug auf Zellzusammensetzung, Architektur und Funktion einem Organ des Körpers ähneln. Organoiden der meisten Organe, darunter Darm, Gehirn, Niere, Lunge, Leber und Netzhaut, haben sich bereits als leistungsfähige Werkzeuge für die Modellierung von Krankheiten, die Entdeckung von Medikamenten und die personalisierte Medizin erwiesen. Herzorganoiden, die aus den drei Herzschichten Myokard, Endokard und Epikard bestehen, konnten aber noch nicht etabliert werden. In dieser Arbeit haben wir die ersten hiPSC-abgeleiteten 3D-Herzmodelle geschaffen, die eine Selbstorganisation von Myokard- und Epikardschichten aufweisen und die wir "Epicardioids" genannt haben. Wir konnten zeigen, dass Epicardioids alle wichtigen Herzzelltypen enthalten und die für die Herzwand typische morphologische und funktionelle Selbststrukturierung rekapitulieren. In einer Proof-of-Concept-Studie wurde der Nutzen von Epicardioids für die

Krankheitsmodellierung anhand der hypertrophen und fibrotischen Reaktion auf eine Endothelin-1-Behandlung veranschaulicht.

Fortschritte bei der CRISPR/Cas9-Genom-Editierung haben das Spektrum der Anwendungen in der biomedizinischen Forschung nochmals erweitert. Insbesondere gibt es neue Hoffnung, dass Gentherapien zur Behandlung und potenziellen Heilung von Herz-Kreislauf-Erkrankungen eingesetzt werden können, unter anderem durch die Korrektur von Mutationen, die vererbte Krankheiten verursachen. In Zusammenarbeit mit Prof. Christian Kupatt haben wir einen neuen gentherapeutischen Ansatz zur Behandlung der Duchenne-Muskeldystrophie (DMD) entwickelt, einer tödlichen Krankheit, die durch den Verlust des Dystrophin-Proteins aufgrund von Frameshift-Mutationen im *DMD* Gen verursacht wird. Bei DMD führt der Verlust von Dystrophin zu fortschreitender Muskeldegeneration und vorzeitigem Tod durch Atem- und Herzversagen. Parallel zu Untersuchungen in einem großen Tiermodell konnten wir zeigen, dass ein duales AAV-System, das für ein Split-Intein-Cas9 und zwei guide RNAs kodiert, Kardiomyozyten, die aus hiPSCs von DMD-Patienten stammen, effizient editieren kann, was zur Wiederherstellung von Dystrophin und zur Verbesserung von Defekten im Kalzium-Handling führt. Nachdem der potenzielle therapeutische Nutzen dieses Ansatzes nachgewiesen wurde, wären Epicardioids eine ideale Plattform für weitere In-vitro-Tests in Bezug auf Wirksamkeit, Sicherheit und Zellspezifität in einem gewebeähnlichen Kontext.

Allgemein bieten die in dieser Arbeit vorgebrachten konvergenten Technologien – Organoide und somatische Gen-Editierung – neue Möglichkeiten, die Grenzen der kardiovaskulären Forschung zu erweitern.

# Table of contents

Abstract .....	i
Zusammenfassung .....	iii
Table of contents .....	v
Abbreviations .....	viii
1 Introduction .....	1
1.1 Cardiovascular disease .....	1
1.1.1 The global burden of cardiovascular disease .....	1
1.1.2 Challenges of clinical development in cardiovascular medicine .....	2
1.2 Cardiac development .....	5
1.2.1 Cell populations and processes of cardiogenesis .....	5
1.2.2 The role of the epicardium in myocardial development and repair .....	7
1.3 In vitro models of human development and disease .....	9
1.3.1 Human pluripotent stem cells .....	9
1.3.2 Organoids .....	12
1.3.3 CRISPR/Cas9 gene editing .....	16
1.4 Aims .....	20
2 Material and methods .....	21
2.1 Cell culture .....	21
2.1.1 Cell lines .....	21
2.1.2 Culture of human pluripotent stem cells .....	21
2.1.3 Differentiation of hiPSCs into FHF- and SHF-enriched cardiac progenitor cells and their derivatives .....	22
2.1.4 Differentiation of hiPSCs into (pro)epicardial cells .....	23
2.1.5 Differentiation of epicardial cells into fibroblasts, smooth muscle cells and endothelial cells .....	24
2.1.6 Differentiation of hiPSCs into cardiomyocytes .....	24
2.1.7 3D cardiac induction of hPSCs .....	25
2.2 Transcriptomic analyses .....	26
2.2.1 RNA isolation and cDNA synthesis .....	26
2.2.2 Quantitative real-time PCR (qRT-PCR) .....	26

2.2.3 Single-cell RNA sequencing.....	28
2.3 Immunofluorescence analysis .....	31
2.3.1 Cryosections.....	31
2.3.2 Immunostaining.....	31
2.4 Functional assays .....	33
2.4.1 Vibratome sectioning.....	33
2.4.2 Calcium imaging .....	33
2.4.3 Optical action potential measurements.....	34
2.4.4 Endothelin-1 treatment .....	34
2.5 Gene editing.....	35
2.5.1 Ribonucleoprotein (RNP)-mediated CRISPR/Cas9 deletion of <i>DMD</i> exon 51 in DMD $\Delta$ 52 hiPSCs.....	35
2.5.2 AAV-mediated CRISPR/Cas9 deletion of <i>DMD</i> exon 51 in DMD $\Delta$ 52 cardiomyocytes.....	36
2.5.3 Genomic PCR.....	36
2.6.4 Capillary Western immunoassay.....	37
2.7 Statistics.....	38
3 Results.....	39
3.1 Generation of epicardioids from human pluripotent stem cells.....	39
3.1.1 Retinoic acid promotes the self-organization of myocardial and epicardial layers in vitro.....	39
3.1.2 The epicardial layer is derived from ISL1 <sup>+</sup> proepicardial progenitors segregating from the myocardial lineage during early epicardioid development.....	48
3.1.3 The epicardial layer is partially formed but not maintained in the absence of retinoic acid.....	53
3.2 Epicardioids recapitulate morphological, functional, and cellular features associated with the epicardium in vivo.....	59
3.2.1 Epicardioids show morphological patterning .....	59
3.2.2 Epicardioids show functional patterning.....	61
3.2.3 The epicardial layer is a source of mesenchymal cells.....	67
3.3 Single-cell time course analysis reveals molecular processes of epicardioid development and maturation.....	72
3.3.1 Time course scRNA-Seq analysis of epicardioids.....	72
3.3.2. First heart field specification is predominant in epicardioids .....	75

---

3.3.3. Transcriptional signatures reflect ventricular patterning and maturation.....	79
3.3.4 Epicardioids uncover human (pro)epicardial fates .....	82
3.3.5 Epicardial cells signal to the myocardium .....	86
3.4 Development of new platforms for in vitro modeling of cardiac disease and therapy .	88
3.4.1 Modeling pathological cardiac hypertrophy in epicardioids .....	88
3.4.2 AAV-mediated somatic gene editing in Duchenne muscular dystrophy .....	90
4 Discussion.....	96
4.1 Retinoic acid promotes the self-organization of myocardial and epicardial layers during 3D cardiac induction of human pluripotent stem cells.....	96
4.2 Epicardioids show unprecedented morphological, molecular, and functional patterning of the myocardial layer.....	98
4.2 Epicardioids as in vitro models of the human (pro)epicardium .....	100
4.3 Applications of epicardioids in disease modeling and drug screening .....	102
4.4 Somatic gene editing: from bench to bedside.....	104
4.3 Limitations and outlook .....	105
References .....	107
Appendix.....	xi
List of figures .....	xi
List of tables .....	xv
List of publications .....	xvi
Acknowledgments .....	xvii

## Abbreviations

AAV	Adeno-associated virus
ALS	Amyotrophic lateral sclerosis
ANOVA	Analysis of variance
AP	Action potential
APD <sub>50</sub>	Action potential duration at 50% repolarization
APD <sub>90</sub>	Action potential duration at 90% repolarization
APS	Anterior primitive streak
ATAC-Seq	Assay for transposable-accessible chromatin using sequencing
BF	Bright field
bp	Base pair
BSA	Bovine serum albumin
CDM	Chemically defined medium
cDNA	Complementary DNA
CHD	Congenital heart disease
CHIR	CHIR-99021
COVID-19	Coronavirus disease 2019
CM	Cardiomyocyte
CPC	Cardiac progenitor cell
CPVT	Catecholaminergic polymorphic ventricular tachycardia
CRISPR	Clustered Regularly Interspaced Short Palindromic Repeats
CRISPRa	CRISPR activation
CRISPRi	CRISPR interference
CVD	Cardiovascular disease
dCas9	Catalytically dead Cas9
DCM	Dilated cardiomyopathy
DEGs	Differentially expressed genes
DMD	Duchenne muscular dystrophy
DNA	Deoxyribonucleic acid
DPBS	Dulbecco's phosphate-buffered saline
DSB	Double-strand break

---

E8	Essential 8 medium
EC	Endothelial cell
EDTA	Ethylenediaminetetraacetic acid
eGFP	Enhanced green fluorescent protein
EHT	Engineered heart tissue
EPDC	Epicardium-derived cell
EMT	Epithelial-mesenchymal transition
ET1	Endothelin-1
FBS	Fetal bovine serum
FHF	First heart field
fps	Frames per second
FRET	Förster resonance energy transfer
GEM	Gel bead-in-emulsion
GMP	Good manufacturing practices
gRNA	Guide RNA
HCM	Hypertrophic cardiomyopathy
HDR	Homology-directed repair
hESC	Human embryonic stem cell
hiPSC	Human induced pluripotent stem cell
HLHS	Hypoplastic left heart syndrome
hPSC	Human pluripotent stem cell
hiPSC-CM	hiPSC-derived cardiomyocyte
Hz	Hertz
Indel	Insertion or deletion
JCF	Juxta-cardiac field
KCl	Potassium chloride
LVNC	Left ventricular non-compaction
LY	LY-294002
mCherry	Monomeric Cherry
MgCl <sub>2</sub>	Magnesium chloride
mRNA	Messenger RNA
NaOH	Sodium hydroxide
NHEJ	Non-homologous end joining

NS-CM	Cardiomyopathy associated with Noonan syndrome
OFT	Outflow tract
PCA	Principle component analysis
PCR	Polymerase chain reaction
PEO	Proepicardial organ
PFA	Paraformaldehyde
Poly-HEMA	Polyhydroxyethylmethacrylate
qRT-PCR	Quantitative real-time PCR
R&D	Research and development
RA	Retinoic acid
RFA	Radiofrequency ablation
RNA	Ribonucleic acid
RNP	Ribonucleoprotein
ROI	Region of interest
RT	Room temperature
SARS-CoV-2	Severe acute respiratory syndrome coronavirus 2
scRNA-Seq	Single-cell RNA sequencing
SHF	Second heart field
SNP	Single nucleotide polymorphism
TALEN	Transcription activator-like effector nuclease
TD <sub>50</sub>	Time to 50% peak decay
TD <sub>90</sub>	Time to 90% peak decay
tracrRNA	Trans-activating CRISPR RNA
TUM	Technical University of Munich
UMAP	Uniform manifold approximation and projection
UMI	Unique molecular identifier
vol	Volume
VSFP	Voltage-sensitive fluorescent protein
ZFN	Zinc finger nuclease
2D	Two-dimensional
3D	Three-dimensional

# 1 Introduction

## 1.1 Cardiovascular disease

### 1.1.1 The global burden of cardiovascular disease

The term cardiovascular disease (CVD) defines a group of disorders of the heart and blood vessels that includes ischemic heart disease, stroke, arrhythmia, cardiomyopathy, and congenital heart disease, among other entities. CVD has been the leading cause of death and a major contributor to disability worldwide for several decades<sup>1</sup>. The number of deaths from CVD has nearly doubled since 1990, collectively representing one-third of all deaths in 2019<sup>1</sup> (Fig. 1a,b). In the United States, increased rates of midlife cardiovascular mortality have contributed to a decline in life expectancy since 2014<sup>2</sup>.

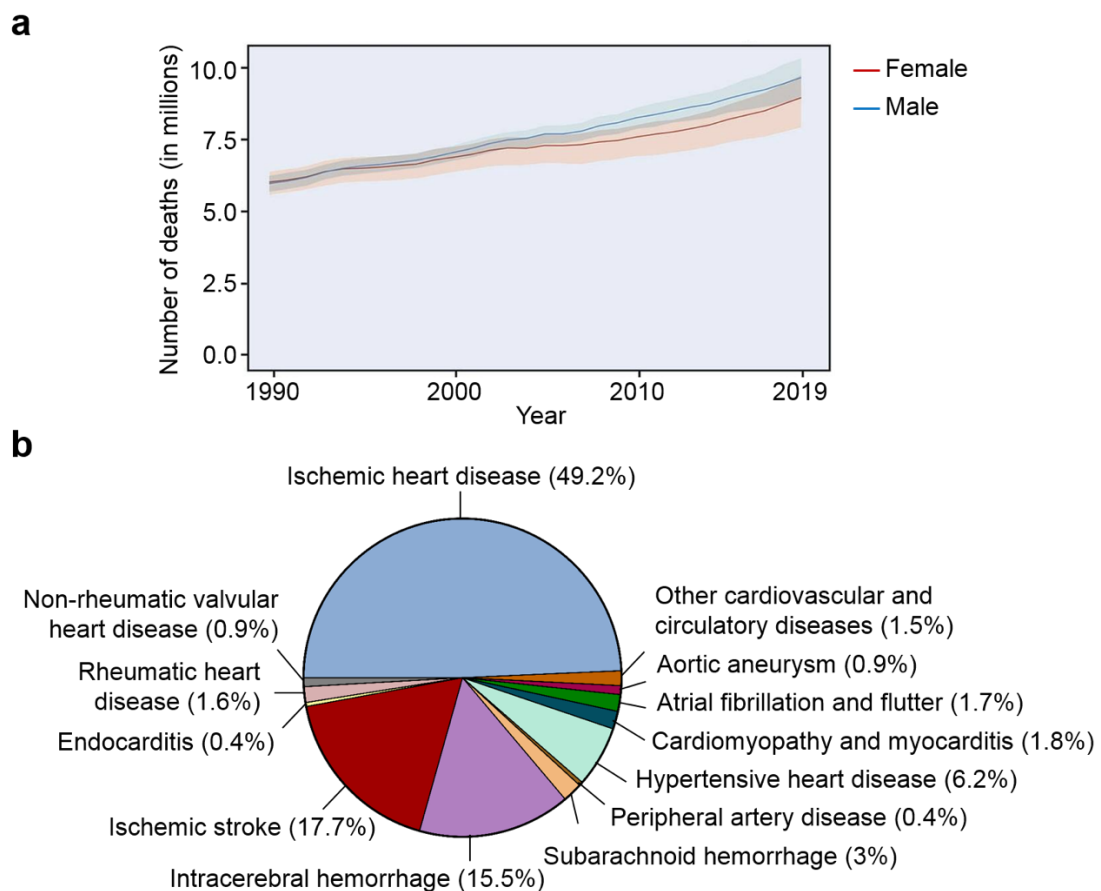


**Figure 1: Global deaths by cardiovascular disease.** (a) Number of worldwide cardiovascular disease (CVD) deaths from 1990 to 2019 by sex. Shaded regions represent 95% uncertainty intervals. (b) Proportion of CVD deaths by cause in 2019. Adapted from Roth et al. 2020, *Journal of the American College of Cardiology*<sup>1</sup>.

A major driver is the rise of risk factors such as poor dietary patterns and physical inactivity leading to obesity<sup>3,4</sup>. The impact of environmental determinants such as geographic location, socioeconomic status, and pollution is also being increasingly recognized<sup>5,6</sup>. In addition, advances in molecular genetics have progressively uncovered a genetic basis in most forms of CVD. More than 100 monogenic diseases – i.e., diseases caused by variants in a single gene – have been characterized, including familial hypercholesterolemia, cardiomyopathies such as hypertrophic cardiomyopathy (HCM) and dilated cardiomyopathy (DCM), and channelopathies such as long QT syndrome and Brugada syndrome<sup>7</sup>. Millions of single nucleotide polymorphisms (SNPs) have also been implicated in polygenic determination of CVDs, notably via genome-wide association studies, but the individual and combinatory effect of SNPs on disease risk remains challenging to determine<sup>8</sup>.

Understanding the molecular and cellular mechanisms underlying disease can facilitate the development of targeted therapies. For example, in HCM associated with hypercontractility due to mutations in sarcomere proteins, a selective inhibitor of cardiac myosin ATPase that reduces myocardial contractility, Mavacamten, is poised to replace non-disease-specific pharmacological treatment<sup>9</sup>. However, innovation is lagging and there is still an enormous clinical need for the development of improved therapies for both inherited and acquired CVDs.

### **1.1.2 Challenges of clinical development in cardiovascular medicine**

Despite the growing public health burden of CVD, the development of new cardiovascular therapies has remained very limited compared to other clinical areas<sup>10</sup>. This is illustrated by the decline in clinical trials for cardiovascular drugs, which accounted for only 6% of new phase III trials in 2015 compared to 21% in 1990<sup>11</sup>. What is even more concerning is that candidate substances showing great promise in preclinical studies fail in clinical trials more often than not, with the probability of launch of a cardiovascular drug entering phase I currently estimated

at 4%, one of the lowest among all disease categories<sup>12,13</sup> (Fig. 2). This is associated with a deprioritization of cardiovascular system disorders in pharmaceutical companies' R&D pipelines<sup>14</sup>. Novel strategies in preclinical and clinical research are needed to overcome this productivity crisis.

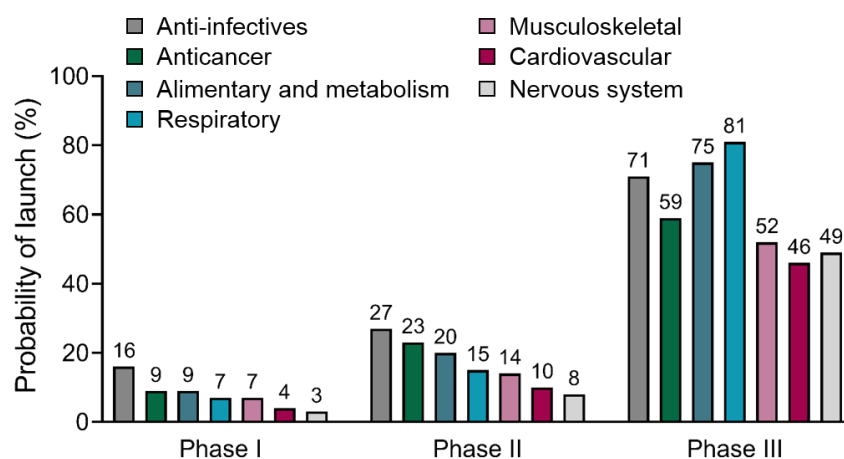


**Figure 2: Probability of launch of new active substances by therapeutic area.** The probability of launch from clinical development phases I, II, and III were calculated for the indicated therapeutic areas by the Center for Medicines Research (CMR) International consortium, based on projects between 2010 and 2017. Adapted from Dowden & Munro 2019, *Nature Reviews Drug Discovery*<sup>12</sup>.

One ambitious goal in the field is to treat and possibly cure patients with gene therapy, which has been an active area of research since the mid-1990s. Most early clinical trials were based on the delivery of transgenes encoding cytokines, growth factors, or enzymes thought to exert a beneficial function<sup>15</sup>. Notably, a series of attempts were made to deliver the gene encoding vascular endothelial growth factor (VEGF) via plasmid DNA or adenoviral vectors with the aim of inducing angiogenesis in patients with ischemic heart disease<sup>16-18</sup>. Due to the low efficiency of plasmid DNA injection and significant immunogenicity of adenoviral vectors, the current gold standard for cardiac gene transfer is the adeno-associated virus (AAV). AAV vectors have several advantages, including broad tropism, ease of production, and low immunogenicity<sup>19</sup>. They infect cells by binding to cell surface receptors, triggering their entry into cells via endocytosis followed by trafficking to the nucleus (Fig. 3). In the nucleus, their

single-stranded DNA genome is released and transcribed into mRNA, allowing translation of the transgenic protein (Fig. 3).

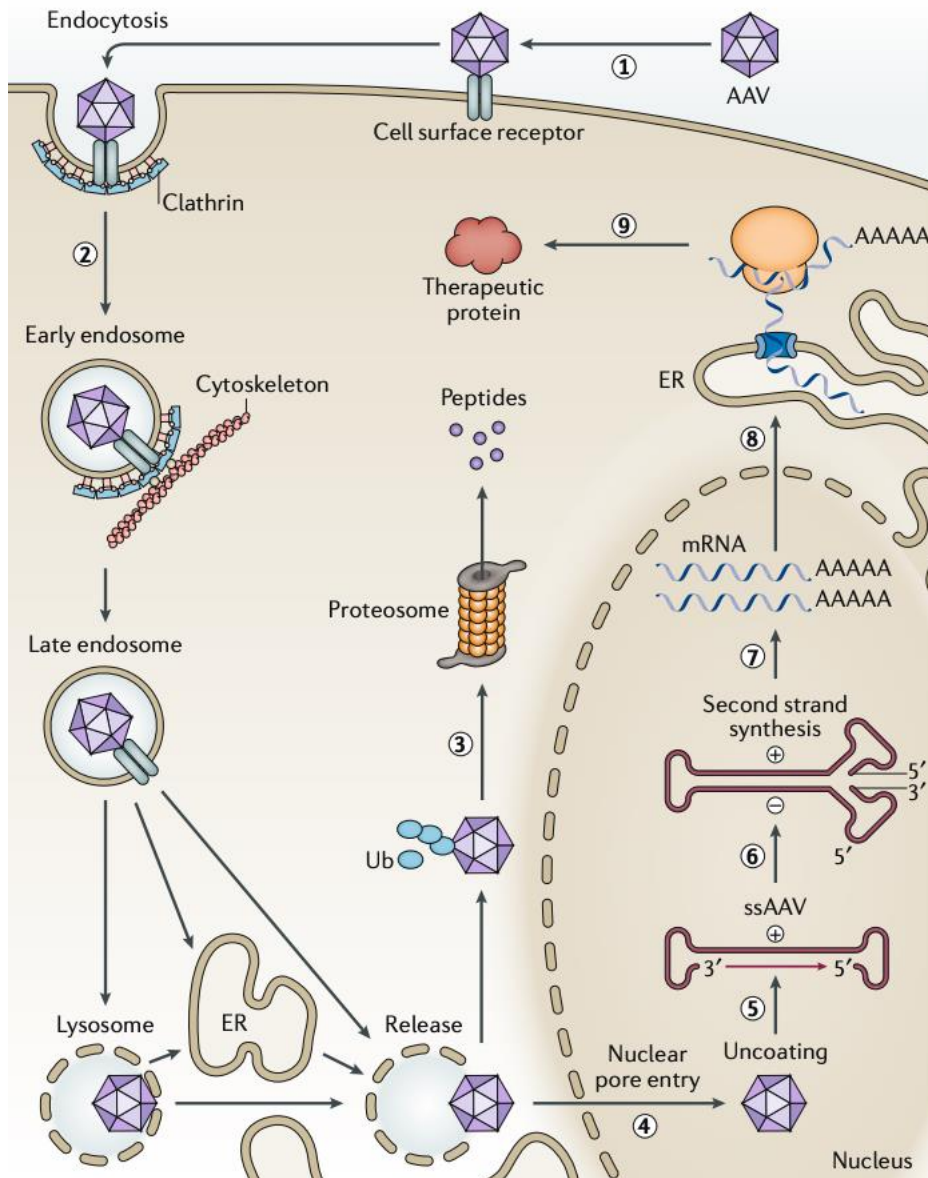


**Figure 3: Mechanisms of AAV-mediated transgene expression.** AAV vectors bind to receptors on the surface of target cells and enter via endocytosis. Following their release from endosomes, AAV virions are either targeted for proteasome-mediated degradation or trafficked into the nucleus. In the nucleus, the single-stranded DNA genome of the virions is released and converted into double-stranded DNA before transcription and export of the mRNA for translation of the transgenic protein. ER: endoplasmic reticulum, Ub: ubiquitin. Adapted from Li & Samulski 2020, *Nature Reviews Genetics*<sup>20</sup>.

The first AAV-based cardiac gene therapy trial consisted in the delivery of the gene encoding the sarcoplasmic reticulum calcium ATPase pump SERCA2a with the aim of increasing its expression levels in patients with heart failure (CUPID; NCT 00454818)<sup>21</sup>. Despite impressive results in rodent and large animal preclinical models, this and all other AAV-based approaches have so far failed to demonstrate definitive clinical benefit in CVD. Success has been achieved in other organs, however, and there are currently two clinically available AAV-based treatments: Luxturna for a rare retinal dystrophy (2017) and Zolgensma for spinal muscular atrophy (2019)<sup>22</sup>. In both cases, the therapy is based on providing the sequence of a gene that is lacking in patients due to mutations. Precise gene modifications, on the other hand, were long considered too inefficient to attempt *in vivo*, especially in postmitotic cells such as cardiomyocytes. However, recent advances in CRISPR/Cas9 gene editing have brought this coveted goal closer to realization (see §1.3.3) and the next generation of cardiac gene therapy aspires to correct the wide spectrum of mutations causing inherited CVDs.

Overall, there is still a great difficulty in translating preclinical research into safe and effective cardiovascular therapies. To identify new targets and improve preclinical cardiac models, a better understanding of the processes of cardiac development and function is essential.

## 1.2 Cardiac development

### 1.2.1 Cell populations and processes of cardiogenesis

The heart is the first functional organ to develop in the human embryo; it starts to beat and pump blood at around 4 weeks of development. Based primarily on studies in mouse and avian embryos, our current understanding is that cardiac specification is initiated at the time of gastrulation, the process by which the single epithelial layer of the early embryo, the epiblast, becomes a multilayered structure composed of the definitive germ layers of endoderm, mesoderm, and ectoderm. The basic helix-loop-helix transcription factor *Mesp1*, expressed in the nascent mesoderm, was identified as the earliest marker of cardiac precursors<sup>23,24</sup>. Fate mapping experiments showed that *Mesp1*<sup>+</sup> cells ingress early through the primitive streak and migrate laterally towards the head folds to form the first cardiac structure, known as the cardiac crescent<sup>25</sup>. This takes place at embryonic day E7.5 in the mouse, corresponding roughly to the

second week of human gestation. The cardiac crescent is composed of progenitors referred to as the first heart field (FHF), which later mainly contribute to the left ventricle (Fig. 4). The cardiac crescent then fuses at the midline to form a beating primitive heart tube that is progressively expanded by the recruitment of cells of the second heart field (SHF) at the arterial and venous poles. These cells originate from the pharyngeal mesoderm posterior to the heart tube and mainly contribute to the right ventricle, the outflow tract, and portions of the atria (Fig. 4)<sup>26,27</sup>. Rightward looping of the heart tube followed by septation eventually results in the four-chambered heart composed of two atria and two ventricles at E10.5 (Fig. 4). The primitive heart tube initially consists of an inner layer of endocardium, which will form the innermost layer of the adult heart, and an outer layer of myocardium, the heart muscle proper. The outermost layer of the adult heart, the epicardium, is formed by cells that migrate from a transient cluster of mesothelial cells protruding from the septum transversum called the proepicardial organ (PEO) around E9.5<sup>28-30</sup>. A distinct population derived from the neural tube, cardiac neural crest cells (CNCCs), contributes both cells and signals to several structures of the heart, including the outflow tract, interventricular septum, valves, and parasympathetic innervation of the heart<sup>31</sup>.

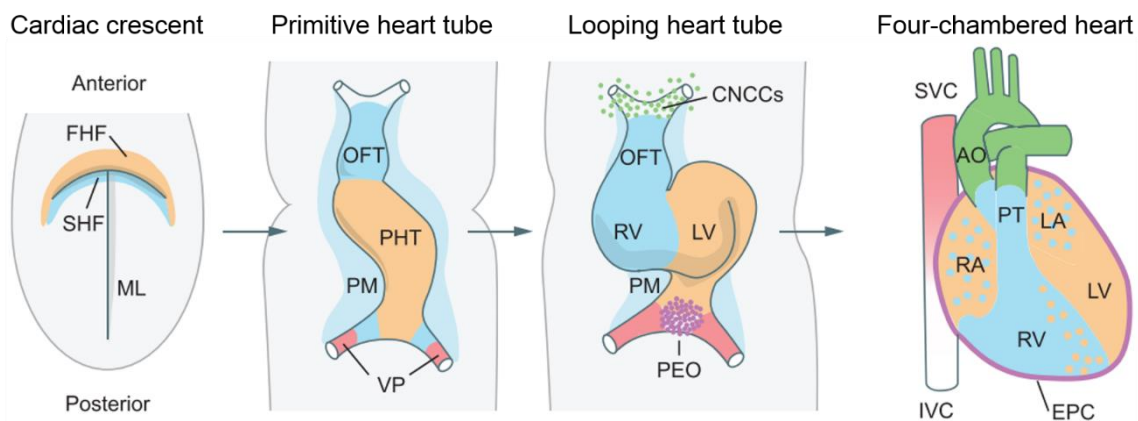


**Figure 4: Stages of heart development and the contribution of cardiac lineages.** Graphical representation of the stages of cardiogenesis from the cardiac crescent to the four-chambered heart and the contribution of the indicated progenitor populations based on mouse development. FHF: first heart field, SHF: second heart field, ML: midline, OFT: outflow tract, PHT: primitive heart tube, PM: pharyngeal mesoderm, VP: venous poles, CNCCs: cardiac neural crest cells, PEO: proepicardial organ, LV: left ventricle, RV: right ventricle, LA: left atrium, RA: right atrium, SVC: superior vena cava, IVC:

inferior vena cava, AO: aorta, PT: pulmonary trunk, EPC: epicardium. Adapted from Später et al. 2014, *Development*<sup>β2</sup>.

The molecular mechanisms driving the differentiation of the diverse cell types of the heart are still incompletely understood. Early differentiation of FHF progenitors towards the myocytic lineage is driven by BMP and FGF signaling concomitant with inhibition of the Wnt pathway, leading to expression of the key cardiac regulators *Nkx2.5*, *Gata4* and *Tbx5*<sup>33–35</sup>. At this time, SHF precursors are marked by expression of the LIM-homeodomain transcription factor *Isl1*, which is part of a complex regulatory network including other transcription factors such as *Tbx1*, *Fgf8* and *Fgf10*<sup>36</sup>. Lineage tracing studies have shown that SHF progenitors give rise to cardiomyocytes as well as smooth muscle cells and endothelial cells<sup>37,38</sup>. They have also been shown to contribute to the proepicardium, marked by expression of *Wt1* and *Tbx18*<sup>39</sup>. In addition, a subset of the FHF referred to as the juxta-cardiac field (JCF), located at the rostral border of the cardiac crescent, was recently described in the mouse as a common progenitor of myocardium and epicardium<sup>40,41</sup>. This points to a more complex mechanism of (pro)epicardial lineage specification than previously thought, and it is unclear how this translates to the human embryo. After the epicardium is formed, a subset of cells undergoes epithelial-to-mesenchymal transition (EMT) to become epicardial-derived cells (EPDCs) that migrate into the myocardial layer. It is well-established that EPDCs give rise to cardiac fibroblasts and vascular smooth muscle cells, and some studies have provided controversial evidence of EPDC differentiation into cardiomyocytes and coronary endothelial cells<sup>42–44</sup>.

### 1.2.2 The role of the epicardium in myocardial development and repair

In addition to the cellular contributions described above, the epicardium significantly influences the maturation of the myocardium during development. Specifically, epicardial cells secrete mitogens such as IGF2, FGF2, and FGF9 that stimulate cardiomyocyte proliferation, contributing to the formation of a subepicardial compact zone distinct from the trabecular myocardium facing the endocardium<sup>45,46</sup>. This is demonstrated by the abnormally thin compact layer resulting from surgical or genetic ablation of the epicardium<sup>47,48</sup>. Studies in avian embryos have suggested that EPDCs also promote the differentiation of Purkinje fibers, the specialized cardiomyocytes of the peripheral conduction system<sup>49</sup>. In turn, signals from the myocardium

including FGF10 promote epicardial EMT and the differentiation of EPDC-derived fibroblasts<sup>50</sup>. An overview of the key signaling pathways implicated in epicardium-myocardium crosstalk during heart development is presented in Figure 5.

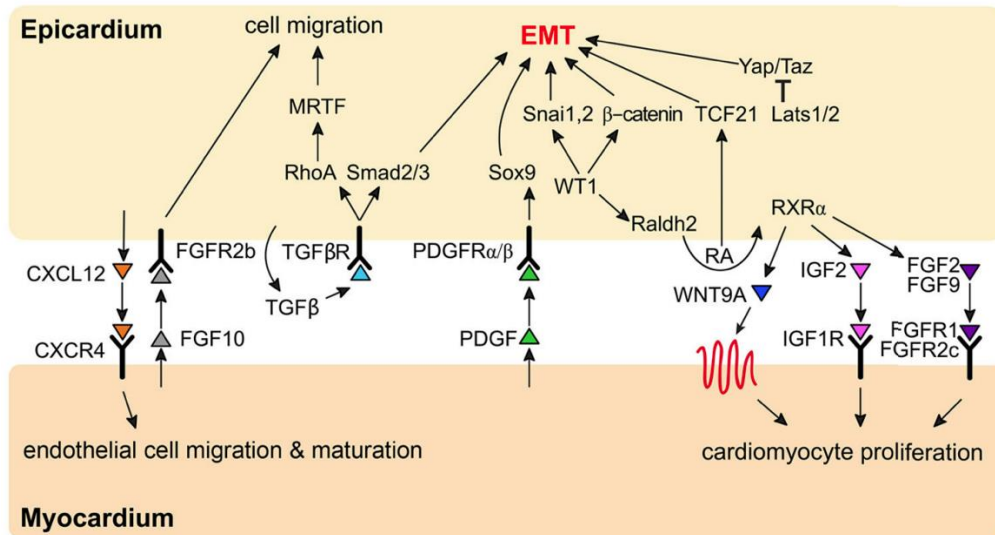


**Figure 5: Signaling pathways involved in epicardium-myocardium crosstalk during cardiogenesis.** EMT: epithelial-to-mesenchymal transition, RA: retinoic acid. Adapted from Quijada et al. 2020, *Circulation Research*<sup>51</sup>.

The epicardium has also become an area of interest with regards to its regenerative potential. In contrast to mammals, zebrafish have the capacity to fully regenerate adult hearts following substantial injury, such as 20% amputation, and the epicardium is central to this process<sup>52</sup>. This is demonstrated by significantly reduced cardiomyocyte proliferation and delayed regeneration when the epicardium is genetically deleted<sup>53</sup>. Epicardial cells have been shown to proliferate at the site of injury and to provide paracrine signaling stimulating cardiomyocyte proliferation, including retinoic acid and IGF2<sup>54,55</sup>. Regeneration is also dependent on epicardial deposition of fibronectin, which promotes cardiomyocyte recruitment to the site of injury via fibronectin-integrin- $\beta 3$  binding<sup>56</sup>. The neonatal mouse heart has a comparable capacity of regeneration, which appears to depend on similar processes as in the adult zebrafish<sup>57</sup>. This includes the re-activation of embryonic epicardial genes, and subsequent proliferation of epicardial cells and cardiomyocytes. However, this capacity is lost just a few days after birth, at which point there is a switch from regeneration to the fibrosis and scarring

that characterize adult wound-healing. Of note, the adult response to injury also involves epicardial activation and signaling. However, in this setting, it is associated with increased fibroblast proliferation and collagen deposition that lead to scarring and progressively impaired heart function<sup>58</sup>. The epicardium was also implicated in the immune and inflammatory response associated with cardiac injury<sup>59</sup>.

A few studies have suggested a higher regenerative capacity in human newborns than in adults. For example, the youngest infants were found to have the best potential for functional recovery following surgical correction of congenital coronary artery defects<sup>60</sup>. Newborns also have the greatest proportion of proliferating cardiomyocytes, with a drop from 0.016% cytokinesis at birth to 0.005% by adolescence<sup>61</sup>. This suggests that there is some evolutionary conservation of early regenerative processes, and that insights from zebrafish and neonatal mammals, including the modulation of epicardial signaling, could lead to new therapeutic approaches in adults.

## **1.3 In vitro models of human development and disease**

### **1.3.1 Human pluripotent stem cells**

As access to human heart tissue is severely limited, studies in animals and particularly mice have been the basis for most of our current knowledge of cardiac development, function, and disease. However, there are unavoidable differences in size and function between human and murine hearts. To accommodate a heart rate that is up to 10 times faster than in humans, mouse cardiomyocytes differ in myofilament expression profile, action potential shape, and contraction kinetics, among other parameters<sup>62</sup>. This has made many findings difficult to extrapolate to the human system. Large animal models such as pigs are closer to humans and therefore better suited to translational research, but they are associated with significantly higher cost and difficulty of handling. In recent years, human pluripotent stem cells have emerged as a promising alternative for the generation of advanced models of the human heart.

Stem cells are defined by their capacity to self-renew indefinitely and to differentiate into other cell types. They are further categorized according to their differentiation potential: *pluripotent* stem cells have the capacity to give rise to any cell type, while *multipotent* stem cells – such as

the adult stem cells found in certain organs – only develop into a limited number of cell types of a certain lineage. The only *totipotent* stem cells in the human body are early blastomeres that give rise to all cells of the embryo as well as to extra-embryonic tissues such as the placenta. The first human pluripotent stem cells available for research were embryonic stem cells, which were isolated from the inner cell mass of preimplantation embryos for the first time in 1998<sup>63</sup>. Although this opened up the exciting possibility of generating any human cell in a dish, the applications of human embryonic stem cells have remained considerably restricted by ethical concerns<sup>64,65</sup>.

The field was transformed in 2006 by the discovery of a method to reprogram murine somatic cells into so-called induced pluripotent stem cells (iPSCs), which was applied to human cells in 2007<sup>66,67</sup>. This was achieved by Shinya Yamanaka and Kazutoshi Takahashi, who found that ectopic expression of 24 regulators of pluripotency in fibroblasts was sufficient to convert them to cells displaying all characteristics of embryonic stem cells. In further experiments, they were able to reduce the required factors to four: Oct3/4, Sox2, Klf4, and c-Myc, sometimes referred to as OSKM. This was heralded as a breakthrough for biomedical research and earned Yamanaka the Nobel Prize in Physiology or Medicine just a few years later in 2012. Since then, the original protocol has been refined in academic and commercial labs worldwide. Alternative reprogramming factors were identified, including Nanog and Lin28<sup>68</sup>. Initially used retroviral and lentiviral vectors were largely replaced with non-integrative delivery systems such as Sendai virus, episomal plasmids, mRNA, proteins or small molecules to avoid disrupting the cells' genome<sup>69</sup>. This is especially relevant in the context of clinical applications, to avoid insertional mutagenesis. Finally, while most early iPSC lines were reprogrammed from dermal fibroblasts, they can now be derived from more easily accessible peripheral blood cells or from any other cell type<sup>70</sup>.

Researchers envisioned that iPSCs would transform cell-based therapy, as they could – in theory – allow unlimited generation of any cell type of interest as well as autologous transplant of a patient's own cells. This has proved more challenging than expected. Since the first clinical trial for transplantation of iPSC-derived retinal cells to treat macular degeneration in 2014<sup>71</sup>, no therapy based on iPSC-derived cells has found its way into the clinic<sup>72</sup>. One of the main concerns is based on the inherent property of pluripotent stem cells: if even a few undifferentiated or immature cells are transplanted, there is a serious risk of uncontrolled

proliferation and tumor formation<sup>73</sup>. Tumorigenicity may also be caused by genetic mutations having occurred during in vitro culture of iPSCs.

Nevertheless, if iPSC-derived cells have not yet revolutionized regenerative medicine, they have already become a powerful tool for in vitro disease modeling and drug discovery (Fig. 6). Crucially, the ability to generate iPSCs from any healthy or diseased individual has opened the possibility to study pathophysiological processes in relevant genetic contexts. This is a significant advancement compared to in vitro models based on immortalized cell lines or heterologous expression systems. There are now several large-scale biobanks aiming to facilitate the global production and supply of well-characterized iPSC lines from diverse healthy and patient donors, such as the European Bank for induced Pluripotent Stem Cells (EBiSC)<sup>74</sup>, the Human induced pluripotent stem cell initiative (HipSci, United Kingdom)<sup>75</sup>, the RIKEN BioResource research center (Japan)<sup>76</sup>, and WiCell<sup>77</sup> (United States), among others<sup>78</sup>.

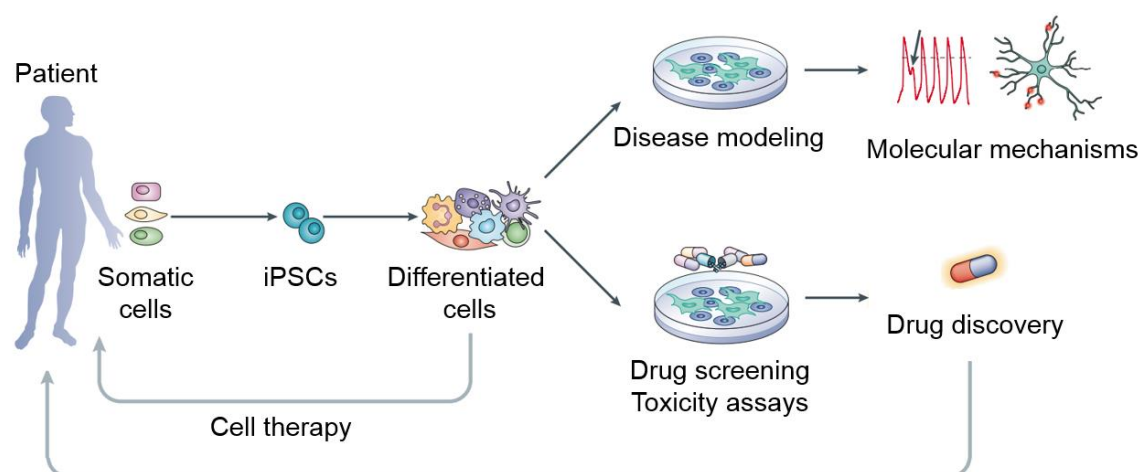


**Figure 6: Applications of human induced pluripotent stem cells (iPSCs) in disease modeling and clinical development.** Adapted from Bellin et al. 2012, *Nature Reviews Molecular Cell Biology*<sup>79</sup>.

The first high-throughput iPSC-based phenotypic screen was performed in 2012 to find a new treatment for familial dysautonomia, a fatal genetic disorder affecting the autonomic nervous system. Close to 7,000 small-molecule compounds were tested on patient iPSC-derived neural crest precursors, leading to the identification of eight drug candidates<sup>80</sup>. Soon after, a discovery made in iPSC-derived motor neurons harboring *SOD1* mutations translated to a phase II

clinical trial for amyotrophic lateral sclerosis (ALS) in less than two years (NCT 02450552)<sup>81</sup>. As recently reported, the candidate compound ezogabine successfully decreased cortical and spinal neuron excitability in ALS, and will be evaluated further<sup>82</sup>. Of note, clinical testing was approved without requiring evidence in the corresponding *SOD1* mouse model, which was historically unreliable in predicting human drug responses<sup>83</sup>. This demonstrates that in some cases, the physiological relevance of human iPSC-based models can match or even surpass that of animal models.

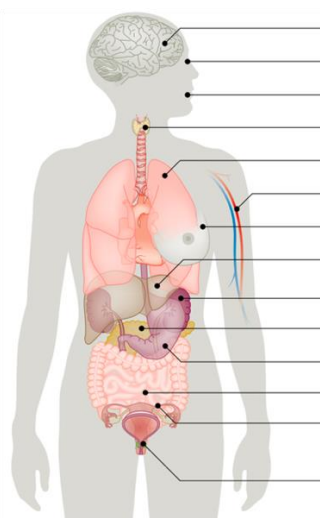
For more than a decade, knowledge of embryonic cardiogenesis has guided the design of protocols for the differentiation of pluripotent stem cells into various cardiac cell types including cardiomyocytes, endothelial cells, epicardial cells, fibroblasts, and smooth muscle cells<sup>84–88</sup>. In 2010, Moretti et al. were the first to demonstrate that hiPSC-derived cardiomyocytes could recapitulate the donor patient's disease phenotype. Specifically, hiPSC-CMs from a patient with long-QT syndrome type I carrying a mutation in the *KCNQ1* gene showed electrophysiological features typical of the disease, including prolonged action potential duration<sup>89</sup>. Since then, disease models based on hiPSC-derived cardiomyocytes have been used to study the mechanisms of various cardiovascular diseases including other channelopathies such as Timothy syndrome<sup>90</sup> and catecholaminergic polymorphic ventricular tachycardia (CPVT)<sup>91,92</sup>, cardiomyopathies such as hypertrophic cardiomyopathy (HCM)<sup>93,94</sup>, dilated cardiomyopathy (DCM)<sup>95,96</sup>, and cardiomyopathy associated with Noonan syndrome<sup>97</sup>, as well as structural defects such as hypoplastic left heart syndrome (HLHS)<sup>98</sup>. In the ongoing COVID-19 pandemic, hiPSC-derived cardiomyocytes have been employed to determine the cytopathic effects of SARS-CoV-2 infection<sup>99,100</sup>.

### 1.3.2 Organoids

It has long been recognized that cells cultured in 2D fail to recapitulate certain features of their *in vivo* counterparts, prompting researchers to grow cells in various 3D settings to imitate tissue formation<sup>101</sup>. Some of the earliest experiments consisted in the reaggregation of dissociated organs from amphibian or chick embryos<sup>102,103</sup>. In 1987, Li and colleagues showed that murine mammary epithelial cells spontaneously formed 3D ducts and lumens when grown in an extracellular matrix gel produced by Engelbreth-Holm-Swarm mouse sarcoma cells (the source of the still commonly used substrate Matrigel)<sup>104</sup>. The first engineered heart tissues

(EHTs) were formed by seeding cardiac cells from chicken embryos or neonatal rodents in extracellular matrix (ECM) hydrogels usually composed of collagen, Matrigel, or fibrin<sup>105–108</sup>. Human cells derived from iPSCs or ESCs are now more commonly used and many different types of culture systems have been designed to promote EHT maturation through medium and matrix composition, mechanical strain, or electrical stimulation<sup>109–113</sup>.

In parallel to these advances in traditional tissue engineering, a new class of stem cell-based 3D models has emerged: organoids. Although the term has historically been applied to various organotypic structures, in the strict sense organoids are defined as stem cell-derived, self-organized microtissues that resemble an organ of the body in terms of cell composition, structure, and function<sup>114</sup>. The first organoids were generated in 2009 from murine intestinal crypts, which contain Lgr5<sup>+</sup> adult stem cells. Hans Clevers and his team discovered that by embedding individual crypts in Matrigel and applying the growth factors EGF and R-spondin 1, they could induce the spontaneous formation of 3D structures containing crypts and villi comprising all major cell types of the intestinal epithelium: enterocytes, goblet cells, enteroendocrine cells, and Paneth cells<sup>115</sup>. This was followed by many other organoids derived from adult stem cells or pluripotent stem cells, notably brain<sup>116</sup>, kidney<sup>117</sup>, and pancreas<sup>118</sup> organoids, among others<sup>119</sup>. As visible in the overview of human organoid systems reported up to date (Fig. 7), a notable exception is the heart. It is an intense area of research and several hPSC-derived cardiac models recapitulating some aspects of heart development have been described<sup>120–122</sup>. Most notably, Hofbauer et al. recently generated so-called cardioids consisting of early myocardium forming an inner cavity lined with an endocardium-like layer<sup>121</sup>. However, cardiac organoids consisting of self-organized myocardium, endocardium, and epicardium have not yet been reported.



	AdSC-derived	PSC-derived
Brain		✓
Optic cup/retina		✓
Salivary gland	✓	✓
Thyroid		✓
Lung	✓	✓
Blood vessel		✓
Mammary gland	✓	✓
Liver	✓	✓
Kidney	✓	✓
Pancreas	✓	✓
Stomach	✓	✓
Intestine	✓	✓
Fallopian tube, endometrium	✓	✓
Bladder, prostate	✓	

**Figure 7: Reported human organoid systems.** Overview of the human organoid systems reported up to date; the establishment of protocols based on adult stem cells (AdSC) or pluripotent stem cells (PSC) is indicated. Adapted from Kim et al. 2020, *Nature Reviews Molecular Cell Biology*<sup>119</sup>.

Universally, organoid formation is based on the self-patterning and differentiation of cells upon modulation of signaling pathways that have been found to control the development of the organ *in vivo*, generally through animal studies. Across the three germ layers, lineage specification and the terminal differentiation of cells from respective precursors is mainly regulated by sequential activation and inhibition of Wnt, Activin A, FGF, EGF, and BMP signaling (Fig. 8)<sup>119</sup>. In the majority of cases, organoid formation is also dependent on ECM embedding, which can be attributed to the instructive signals received by cells from the ECM during development. Although ECM components are not known to directly determine cell fate, they are important regulators of cell migration and proliferation and provide structural support<sup>123</sup>. Matrigel has long been used as a one-size-fits-all ECM, but due to its undefined and variable composition, the field is moving towards matrices that better represent the organ in question in terms of composition and structural properties<sup>124,125</sup>. The protocols used are still far from reproducing the exact spatiotemporal coordination of biochemical and biophysical cues driving organ formation *in vivo*, which illustrates the extraordinary self-organizing capacity of stem cells. However, in the case of the heart, it appears that a key piece of the developmental puzzle is still missing from current differentiation approaches.

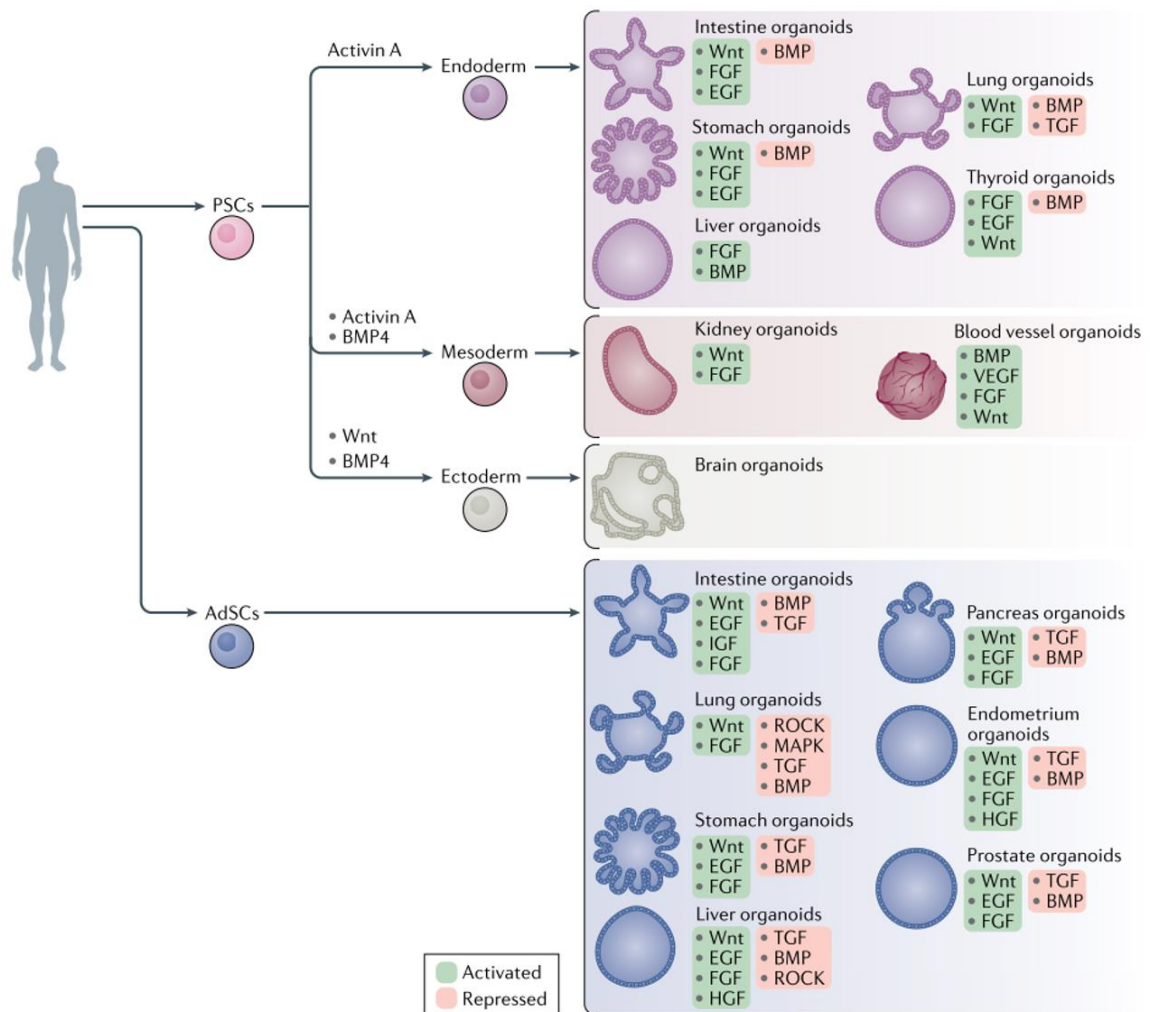


**Figure 8: Signaling pathways involved in the generation of human organoids.** Overview of the signaling pathways activated or repressed to induce the stepwise lineage commitment of pluripotent stem cells (PSCs) or adult stem cells (AdSCs) for the formation of the indicated human organoids. Adapted from Kim et al. 2020, *Nature Reviews Molecular Cell Biology*<sup>119</sup>.

Organoids have rapidly become invaluable tools for studying pathophysiological processes that cannot be adequately modeled in 2D cultures or, in some cases, in animal models. Human cerebral organoids have for example been used to investigate the neurodevelopmental disorder microcephaly, which is not recapitulated in mice due to significant differences in neural progenitor dynamics between mice and humans<sup>116</sup>. Similarly, Freedman et al. showed that kidney organoids derived from iPSCs carrying mutations causing polycystic kidney disease recapitulated pathological cyst formation, which did not occur in 2D layers of kidney cells with

the same genotype<sup>126</sup>. Patient-derived organoids may also facilitate personalized therapy approaches such as genotype-based stratification for drug prescription. In cystic fibrosis, a fatal disease caused by over 2,000 mutations in the *CFTR* gene, it was shown that rectal organoids from patients carrying different mutations accurately predicted the individuals' response to different *CFTR* modulators<sup>127</sup>. The drug response was determined via a functional assay based on organoid swelling as a readout for *CFTR*-dependent ion and fluid transport into the closed organoid lumen<sup>128</sup>. Overall, the strength of organoids as *in vitro* model lies in the combination of tissue architecture and function, which are fundamentally intertwined *in vivo*. In the future, this feature may also make them advantageous candidates for regenerative medicine. If GMP-compliant production can be achieved, pancreatic organoids could for example replace severely damaged pancreatic tissue in type I diabetes<sup>129</sup>. Considering the crucial challenge of replacing damaged tissue after myocardial infarction, this may also be an area of application for cardiac organoids.

### 1.3.3 CRISPR/Cas9 gene editing

Concomitant with the emergence of organoid-based models, biomedical research was revolutionized by the advent of CRISPR/Cas9 gene editing. Derived from a microbial acquired immune system, it is based on the introduction of DNA double-strand breaks (DSBs) at specific loci targeted by the Cas9 nuclease via a small guide RNA<sup>130</sup>. This triggers cells to repair the double-strand break either by the error-prone non-homologous end joining (NHEJ) pathway, leading to frequent indels, or by precise homology-directed repair (HDR) when a template has been provided (Fig. 9). As the CRISPR/Cas9 system is based on Watson-Crick base pairing between the target DNA sequence and the guide RNA, it dramatically simplified gene editing compared to its predecessors based on DNA-protein interactions, such as transcription activator-like effector nucleases (TALENs) and zinc finger nucleases (ZFNs), effectively rendering them obsolete<sup>131</sup>. In recognition of the immense potential of this technology for both basic and translational research, the Nobel Prize in Chemistry was awarded to Jennifer A. Doudna and Emmanuelle Charpentier for its discovery in 2020.

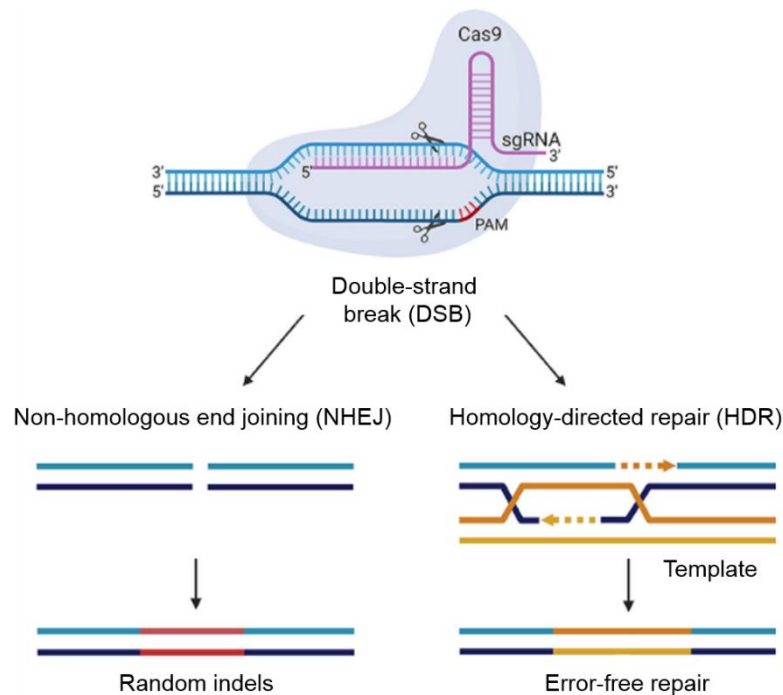


**Figure 9: Mechanisms of CRISPR/Cas9-mediated gene editing.** The Cas9 nuclease forming a complex with the single guide RNA (sgRNA) creates a double-strand break (DSB) 3 base pairs upstream of the protospacer adjacent motif (PAM). The cell's own machinery then repairs the DSB by the error-prone non-homologous end joining (NHEJ) pathway, leading to frequent insertions and deletions (indels), or by the precise homology-directed repair (HDR) pathway if a suitable repair template is available for homologous recombination. Adapted from Uddin et al., 2020 *Frontiers in Oncology*<sup>132</sup>.

The NHEJ pathway is typically exploited to knock out genes by introducing a random indel leading to a premature stop codon, though it can also mediate the deletion of a large sequence following the introduction of two DSBs on either side. By contrast, HDR serves to precisely modify the targeted locus, i.e., to introduce or correct a mutation or to insert a transgene. However, compared to the highly efficient NHEJ pathway, HDR has a low efficiency of only  $\sim 0.1\text{-}5\%$ <sup>133</sup>. As precise gene editing rather than gene disruption is desirable in most biomedical applications, strategies have been developed to increase the efficiency of HDR, for example by inhibiting components of the competing NHEJ pathway or by optimizing the design of sgRNAs and repair templates<sup>134,135</sup>. Considering potential clinical applications, great efforts have also been made to reduce the occurrence of off-target DSBs at sites that match to some degree to the guide RNA, which could cause deleterious mutations including oncogene

activation. One strategy is to replace the Cas9 nuclease with paired Cas9 nickases that introduce single-strand breaks on different DNA strands, which significantly reduces off-target effects<sup>136,137</sup>. Moreover, entirely new classes of CRISPR editors have been developed that allow precise editing without DSBs or donor templates. So-called base editors enable the introduction or correction of point mutations by direct chemical conversion of the target DNA base into another<sup>138,139</sup>. This is based on a catalytically dead Cas9 (dCas9) fused either to a cytidine deaminase enzyme mediating a C-to-T (G-to-A) substitution, in the case of cytosine base editors, or to an adenine deaminase enzyme mediating an A-to-G (T-to-C) substitution, in the case of adenine base editors. An even more recent innovation is prime editing, which directly modifies the target locus via a Cas9 nickase fused to an engineered reverse transcriptase and a guide RNA that both specifies the target site and encodes the desired edit<sup>140</sup>. In contrast to base editing, this can be employed to introduce specific insertions (up to 44 bp) or deletions (up to 80 bp) as well as all types of point mutations including transversion mutations (e.g. C-to-A, C-to-G, T-to-A...). Neither prime nor base editing systems exclude off-target edits, however, and optimizations are still underway.

In the context of PSC-based disease modeling, CRISPR/Cas9 editing has opened the possibility of easily generating isogenic cell lines, i.e., cell lines that differ only in a specific locus of interest, to remove the confounding effects of genetic background. Typically, a disease-causing mutation is corrected in a patient iPSC line to obtain an isogenic “healthy” control line for phenotypical analyses in derived cells or organoids, although many other genetic modifications may be of interest depending on the scientific question<sup>141,142</sup>. Gene editing is also commonly used to knock reporter transgenes such as fluorescent proteins into PSCs to follow populations of interest based on their gene expression. To avoid unwanted effects after transgene insertion, so-called safe harbor loci that can accommodate the insertion of exogenous sequences without repressing their expression or causing alterations to the host genome have been identified<sup>143,144</sup>.

When generating genetically modified lines, undifferentiated PSCs undergo editing and single clones are screened for the desired modification before expansion, so that a homogeneous population is obtained regardless of initial editing efficiency. However, with CRISPR/Cas9 technology transforming the landscape of gene therapy, there is increased interest in establishing methods for gene editing in terminally differentiated cells or organoids, which is significantly more challenging. The rationale is that human PSC-derived models can serve as

platforms to optimize editing efficiency, evaluate phenotypical consequences of editing as well as detect unpredicted side-effects. Brain and lung organoids have for example been used to test AAV-mediated gene therapy by identifying the AAV serotypes with the highest transduction efficiency in the respective cell types<sup>145,146</sup>.

Taking into account these recent advances in organoid and gene editing technologies, Figure 10 summarizes the expanded spectrum of human iPSC-based applications in basic and translational biomedicine today.

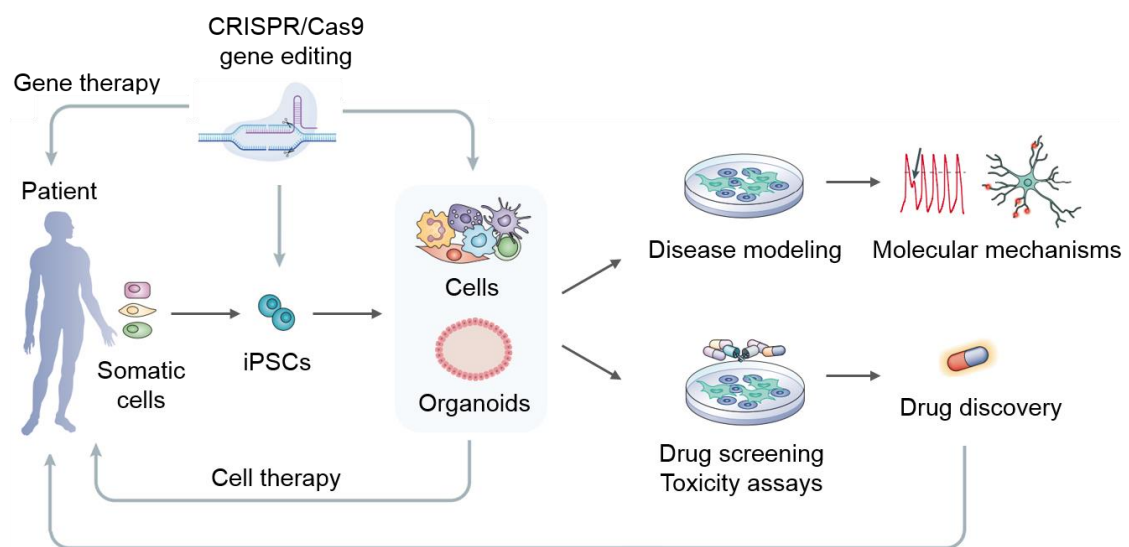


**Figure 10: Intersecting applications of iPSCs, organoids and CRISPR/Cas9 gene editing in basic and translational biomedicine.** Adapted from Bellin et al. 2012, *Nature Reviews Molecular Cell Biology*<sup>79</sup>.

## 1.4 Aims

Considering the unmet needs in cardiovascular biomedicine described above, the work described in this thesis pursued the two following objectives.

1. Based on knowledge of the molecular mechanisms of cardiogenesis as well as the principles of organoid generation, the first objective was to establish the first human pluripotent stem cell-derived cardiac organoids combining morphological self-organization, multicellularity, and functional patterning.
2. In a collaborative effort to bring AAV-based gene therapy closer to clinical application, the second objective was to evaluate the efficacy of a novel AAV system for CRISPR/Cas9-mediated somatic gene editing of cardiac cells for the treatment of Duchenne muscular dystrophy.

## 2 Material and methods

This section details the cell lines, reagents, oligonucleotides, and experimental procedures used in this work. The catalog number of each commercially available reagent is indicated at first mention.

### 2.1 Cell culture

#### 2.1.1 Cell lines

The human pluripotent stem cell lines used in various differentiation experiments are listed in Table 1. Details of cell line generation and validation can be consulted in the Human Pluripotent Stem Cell Registry (hPSCreg) under the indicated IDs. Authorization to use the human embryonic stem cell line HES-3 (hPSCreg ID ESIBIe003-A-3) generated by ES Cell International Pte Ltd in Singapore was granted by the Robert Koch Institute to Prof. Alessandra Moretti, the supervisor of this work (AZ 3.04.02/0131).

**Table 1: Human pluripotent stem cell lines**

Cell type	Human Pluripotent Stem Cell Registry ID	Identifier in this work	Sex	Genotype
hiPSC	MRI003-A	hiPSC1	Male	N/A
hiPSC	MRI001-A	hiPSC2	Female	N/A
hiPSC	MRI003-A-6	hiPSC3	Male	AAVS1-CAG-VSFP
hESC	ESIBIe003-A-3	hESC	Female	N/A
hiPSC	MRI027-A	DMDΔ52	Male	<i>DMD</i> del exon 52
hiPSC	MRI027-A-1	DMDΔ51-52	Male	<i>DMD</i> del exons 51 and 52

Del = deletion

#### 2.1.2 Culture of human pluripotent stem cells

For the culture of hPSCs, tissue culture plates were pre-coated with Geltrex (Gibco; A14133-02) according to the manufacturer's instructions. Cells were maintained in Essential 8 medium

(Gibco; A1517001) containing 0.5% Penicillin/Streptomycin (Gibco; 15140-122) under standard culture conditions (37°C, 5% CO<sub>2</sub>); medium was refreshed every day. Cells were passaged every 4 days with 0.5 mM EDTA (Invitrogen; AM92606) in PBS without Ca<sup>2+</sup> or Mg<sup>2+</sup> (PBS<sup>-/-</sup>; Gibco; 10010023). The ROCK inhibitor Thiazovivin (Sigma-Aldrich; SML1045) was added at a concentration of 2 μM for 24 h after passaging to promote survival. For long-term storage, single cells were frozen in cryopreservation medium consisting of 20% DMEM/F-12 (Gibco; 11320033), 60% FBS (Sigma-Aldrich; F7524), and 20% DMSO (Sigma-Aldrich; D2650) at -80°C before transferring to liquid nitrogen storage. Alternatively, for expansion in colonies, cells were incubated with dispase (STEMCELL Technologies; 07913) for 3 min, washed with DMEM/F-12, detached with a scraper and frozen in serum-free mFreSR cryopreservation medium (Stem Cell Technologies; 05855).

### **2.1.3 Differentiation of hiPSCs into FHF- and SHF-enriched cardiac progenitor cells and their derivatives**

Cardiac progenitor cells were differentiated from hiPSCs using a protocol established by Mendjan and colleagues, with some modifications<sup>147</sup>. On day -1, hiPSCs were dissociated with 0.5 mM EDTA for 4-8 min. After counting with a Neubauer chamber, 200,000 cells were seeded per well of a Geltrex-coated 24-well plate in 1 mL Essential 8 medium containing 2 μM Thiazovivin. The basal differentiation medium – referred to as CDM – was prepared by mixing 247.36 mL DMEM/F-12 with GlutaMAX (Gibco; 31331028), 237.36 mL IMDM (Gibco; 21980032), 5 mL chemically defined lipid concentrate (Gibco; 11905031), 10 mL IMDM containing 10% BSA, 250 μL transferrin (Roche; 10652202001) and 20 μL α-monothioglycerol (Sigma-Aldrich; M6145). On day 0, the medium was replaced with 1 mL APS medium consisting of CDM containing 10 ng/mL BMP4 (R&D; 314-BP), 50 ng/mL Activin A (Sigma-Aldrich; SRP3003), 30 ng/mL bFGF (R&D; 233-FB-025/CF), 5 μM LY-29004 (Tocris; 1130) and 1.5 μM CHIR-99021 (Axon Medchem; 1386). Between 40 and 42 h after d0 (referred to as day 2), the medium was replaced with 1 mL CardMeso medium consisting of CDM containing 10 μg/mL insulin (Sigma-Aldrich; I9278), 10 ng/mL BMP4, 8 ng/mL bFGF, 5 μM IWP2 (Tocris; 3533) and, where indicated, 0.5 μM retinoic acid (Sigma-Aldrich; R2625). This medium was refreshed every 24 h until day 6, at which point the medium was replaced with 1 mL CardMyo medium consisting of CDM containing 10 μg/mL insulin, 10 ng/mL BMP4 and 8 ng/mL bFGF. This medium was refreshed 24 h later on day 7. From day 8, cells were

maintained in 2 mL CDM-maintenance medium consisting of CDM containing 10 µg/mL insulin and 0.5% Penicillin-Streptomycin, refreshed every other day.

#### **2.1.4 Differentiation of hiPSCs into (pro)epicardial cells**

hiPSCs were differentiated into (pro)epicardial cells as previously described by Bao and colleagues<sup>85</sup>. On day -3, hiPSCs were washed with PBS<sup>-/-</sup> and dissociated for 3 min at 37°C with Accutase (Gibco; A1110501), stopping the reaction with 5 vol DMEM/F-12. After centrifugation for 5 min at 300 g, cells were counted with a Neubauer chamber and 0.5x10<sup>6</sup> cells were seeded per well of a Matrigel-coated 12-well plate (Corning; 354277) in 1 mL mTeSR1 medium (STEMCELL Technologies; 85850) containing 5 µM of the ROCK inhibitor Y27632 (Calbiochem; 688000) to promote survival. On day -2, the medium was replaced with 2 mL mTeSR1. On day -1, the cells were pre-treated with 2 mL mTeSR1 containing 0.1 µM CHIR99021 (Axon Medchem; CT99021). On day 0, the medium was replaced with 2 mL RPMI 1640 medium (Gibco; 21875034) with B27 minus insulin supplement (Gibco; A1895601) (referred to as basal medium) containing 6 µM CHIR99021. Exactly 24 h later, the medium was replaced with 2 mL basal medium. On day 3, 72 h after addition of CHIR99021, the medium was replaced with 2 mL combined medium prepared by collecting 1 mL medium per well and mixing it with 1 mL freshly prepared basal medium containing 5 µM IWP2 (Tocris; 3533) (final concentration 2.5 µM). On day 5, the medium was replaced with 2 mL basal medium. On day 6, the cells were dissociated with Accutase as described above and passaged 1:6 into 12-well plates coated with 0.1% gelatin (Sigma-Aldrich; G1393) in 1 mL LaSR medium – consisting of Advanced DMEM/F-12 (Gibco; 12634010) with 1.3% GlutaMAX (Gibco; 35050061) and 100 µg/mL L-ascorbic acid (Sigma-Aldrich; A5960) – containing 5 µM Y27632. On days 7 and 8, the medium was replaced with 1 mL LaSR medium containing 3 µM CHIR99021. On days 9 to 11, the medium was replaced with 1 mL LaSR medium every day. On day 12, proepicardial cells were dissociated with Accutase for maintenance, cryostorage, or characterization. For maintenance, cells were passaged 1:6 into gelatin-coated plates in LaSR medium containing 2 µM SB431542 (R&D; 1614/1) to prevent spontaneous differentiation and 5 µM Y27632. The medium was replaced every day with LaSR medium containing 2 µM SB431542.

### **2.1.5 Differentiation of epicardial cells into fibroblasts, smooth muscle cells and endothelial cells**

hiPSC-derived epicardial cells were differentiated into fibroblasts and smooth muscle cells as previously described by Bao and colleagues<sup>85</sup>. On day -1, epicardial cells were dissociated with Accutase as described above and seeded onto gelatin-coated plates at a density of 30,000 cells/cm<sup>2</sup> in LaSR medium containing 5  $\mu$ M Y27632. From day 0 to day 6, medium was replaced every day with LaSR medium containing 10 ng/mL bFGF (R&D; 233-FB-025/CF) or 5 ng/mL TGF- $\beta$ 1 (R&D; 7754-BH-005) for fibroblast and smooth muscle differentiation, respectively. Epicardial cells were differentiated into endothelial cells as previously described by Bao and colleagues, with some modifications<sup>148</sup>. On day -2, epicardial cells were seeded at a density of 60,000 cells/cm<sup>2</sup> onto gelatin-coated plates in LaSR medium containing 5  $\mu$ M Y27632. From day 0 to day 4, the medium was replaced every day with EGM-2 medium (Lonza; CC-3162) containing 100 ng/mL VEGF (R&D; 293-VE-010). From day 5 to day 9, the medium was replaced every day with EGM-2 medium containing 10  $\mu$ M SB431542.

### **2.1.6 Differentiation of hiPSCs into cardiomyocytes**

For somatic gene editing experiments, hiPSCs were differentiated into cardiomyocytes as previously described<sup>149</sup>. Briefly, hiPSCs were seeded into Geltrex-coated 12-well plates at a density of 200,000 cells per well in Essential 8 medium containing 2  $\mu$ M Thiazovivin. Essential 8 medium was replaced every day until the cells reached 90% confluence, at which point cardiac differentiation was initiated by replacing the medium with RPMI 1640 medium with B27 minus insulin (referred to as basal medium) supplemented with 6  $\mu$ M CHIR-99021 (time point corresponding to day 0). On day 2, the medium was replaced with basal medium containing 5  $\mu$ M IWR1 (Tocris; 3132). Around day 12 of differentiation, beating areas were mechanically isolated with needles and transferred to fibronectin-coated plates for long-term maintenance in EB2 medium consisting of DMEM/F-12 containing 2% FBS, 1% non-essential amino acids (Gibco; 11140050), 1% Penicillin-Streptomycin-Glutamine (Gibco; 10378016) and 0.1 mM  $\beta$ -mercaptoethanol (Sigma-Aldrich; M7522), replaced every 2 to 3 days. Cardiomyocytes were kept in culture for approximately 2 months before performing gene editing and calcium imaging experiments.

### 2.1.7 3D cardiac induction of hPSCs

On day -1, hPSCs were dissociated with 0.5 mM EDTA in PBS<sup>-/-</sup> and 30,000-40,000 cells were seeded into poly-HEMA-coated (Sigma-Aldrich; P3932) U-shaped 96-well plates in 150  $\mu$ L Essential 8 medium containing 2  $\mu$ M Thiazovivin. To promote the formation of a single spheroid per well, the plate was centrifuged for 1 min at 300 g. On day 0 (roughly 24 h after seeding cells on day -1) and every 24 h until day 8, medium was replaced with the differentiation media described for cardiac progenitor cell differentiation in §2.1.3. For epicardioids (also referred to as RA spheroids), retinoic acid was included from days 2 to 5, for control spheroids (also referred to as no RA spheroids) it was omitted. For collagen embedding on day 8, spheroids were carefully transferred into 15 mm x 15 mm x 5 mm molds (Tissue-Tek; 4566) placed in the wells of a 6-well plate after trimming the edges with scissors. After removing the medium, the molds were filled with 400  $\mu$ L collagen I solution consisting of 2.17 mg/mL collagen I (Corning; 354249), 20% distilled water (Gibco; 15230162), 5% 10x DPBS (Gibco; 14080055) and 8.3 mM NaOH in EB20 medium consisting of DMEM/F-12 with 20% FBS, 1% non-essential amino acids, 1% Penicillin-Streptomycin-Glutamine, and 0.1 mM  $\beta$ -mercaptoethanol. After distancing the spheroids from each other using a pipette tip and closing the lid of the 6-well plate, they were placed at 37°C for 30 min until the collagen solidified. The gel sheets obtained were then carefully removed from the molds by adding 2 mL CDM-maintenance medium per well of the 6-well plate and slowly pipetting medium under the sheets to make them slide into the medium. Where indicated, 100 ng/mL VEGF (R&D; 293-VE-010) was freshly added to the medium at each medium change from this point on. On day 10, CDM-maintenance medium was replaced and the plates were placed on a rocking shaker (Assistant, Germany) at 40 rpm to improve oxygen and nutrient diffusion. For long-term culture, CDM-maintenance medium was replaced every 2-3 days. The entire collagen sheet containing organoids could be fixed for immunofluorescence staining; to isolate RNA or cut live sections for calcium imaging, organoids were carefully pushed out of the collagen using 10  $\mu$ L pipette tips.

For 3D culture of cardiac progenitor cells (CPCs) differentiated in 2D, CPCs were differentiated with the protocol described in §2.1.3 – including addition of retinoic acid – until day 6. At this point, they were washed with PBS<sup>-/-</sup> and dissociated for 5 min with Accutase, stopping the reaction with 5 vol DMEM/F-12. After centrifugation for 5 min at 300 g, cells were counted with a Neubauer chamber, and 75,000 cells were seeded per well of a poly-

HEMA-coated U-shaped 96-well plate in 150  $\mu$ L CardMyo medium supplemented with 2  $\mu$ M thiazovivin. From the next day, spheroids formed by aggregation were treated in the same way as spheroids obtained by 3D cardiac induction until analysis on day 15.

## 2.2 Transcriptomic analyses

### 2.2.1 RNA isolation and cDNA synthesis

Total RNA was isolated from cells using the Absolutely RNA Microprep kit (Agilent; 400805) or the Absolutely Nanoprep kit (Agilent; 400753), depending on the amount of starting material, following manufacturer's instructions. cDNA was then prepared using the High Capacity cDNA RT kit (Applied Biosystems; 4368814) according to the manufacturer's instructions, running the reaction in a FlexCycler2 PCR thermal cycler (Analytik Jena, Germany). For long-term storage, RNA was kept at  $-80^{\circ}\text{C}$  and cDNA at  $-20^{\circ}\text{C}$ .

### 2.2.2 Quantitative real-time PCR (qRT-PCR)

Quantitative real-time PCR (qRT-PCR) was performed using the Power SYBR Green PCR Master Mix (Applied Biosystems; 4368706) according to the manufacturer's instructions and the primers listed in Table 2. The reaction was run on a 7500 Fast Real-Time PCR instrument (Applied Biosystems, Germany) using the following program.

Stage	Temperature	Duration	Cycles
Holding stage	50°C	20 s	1
	95°C	10 min	
Cycling stage	95°C	15 s	40
	60°C	1 min	
Melting curve	95°C	15 s	1
	60°C	1 min	
	95°C	30 s	
	60°C	15 s	

The mRNA expression levels of genes of interest were quantified relative to *GAPDH* expression using the  $\Delta C_t$  method unless otherwise indicated.

**Table 2: qRT-PCR primer sequences**

Gene	Species	Sequence	
<i>ACTA1</i>	Human	Forward	5' GTGATCACCATCGGAAATGAA
		Reverse	5' TCATGATGCTGTTGTAGGTGGT
<i>BMP4</i>	Human	Forward	5' CACAGCACTGGTCTTGAGT
		Reverse	5' TGGTCCCTGGGATGTTCT
<i>BRACHYURY</i>	Human	Forward	5' TGTTTATCCATGCTGCAATCC
		Reverse	5' CCGTTGCTCACAGACCACAG
<i>CD31</i>	Human	Forward	5' ATGCCGTGGAAAGCAGATAC
		Reverse	5' CTGTTCTTCTCGGAACATGGA
<i>CDH5</i>	Human	Forward	5' CCTACCAGCCCAAAGTGTGT
		Reverse	5' TGTCCCTGTCTATTGCGGAGA
<i>COL1A2</i>	Human	Forward	5' CCTGGTGCTAAAGGAGAAAGAGG
		Reverse	5' ATCACCACGACTTCCAGCAGGA
<i>COL3A1</i>	Human	Forward	5' TGGTCTGCAAGGAATGCCTGGA
		Reverse	5' TCITTTCCCTGGGACACCATCAG
<i>GAPDH</i>	Human	Forward	5' TCCTCTGACTTCAACAGCGA
		Reverse	5' GGGTCTTACTCCTTGGAGGC
<i>HAND1</i>	Human	Forward	5' AACTCAAGAAGGCGGATGG
		Reverse	5' CGGTGCGTCCITTAATCCT
<i>HOXB6</i>	Human	Forward	5' CATATCTTGATCTGCCTCTCCGTCAG
		Reverse	5' CACTCCGGTCTACCCGTGGATGCA
<i>ISL1</i>	Human	Forward	5' AAAGTTACCAGCCACCTTGGGA
		Reverse	5' ATTAGAGCCCGGTCCTCCTT
<i>MAB21L2</i>	Human	Forward	5' GAGTGCTACTCGCTGACCG
		Reverse	5' CACTGAGAGGCACTTGTTTC
<i>MESP1</i>	Human	Forward	5' GTGCTGGCTCTGTTGGAGA
		Reverse	5' CAGAGACGGCGTCAGTTGT
<i>MYH6</i>	Human	Forward	5' TCAGGATTCTCCGTGAAGGG
		Reverse	5' CTCITCCTTGTCATCGGGCA
<i>MYH7</i>	Human	Forward	5' TGTAGACACACTTGAGTAGCCC
		Reverse	5' ACGGTCACGTCTTGGCCATA
<i>MYH11</i>	Human	Forward	5' GAAGACCTGGTCAGCTCCAA
		Reverse	5' CAGCTGCGTCTTCATCTCCT
<i>MYL2</i>	Human	Forward	5' TACGTTCCGGAAATGCTGAC
		Reverse	5' TTCTCCGTGGGTGATGATG
<i>MYL3</i>	Human	Forward	5'AAGGAGGTCGAGTTTGATGCT

		Reverse	5'TCCTTGAACTCITCAATCTGCTC
<i>NKX2.5</i>	Human	Forward	5' CAAGTGTGCGTCTGCCTTT
		Reverse	5' TTGTCCGCCTCTGTCTTCTC
<i>NPPA</i>	Human	Forward	5' CAACGCAGACCTGATGGATTT
		Reverse	5' AGCCCCGCTTCTTCATTC
<i>NPPB</i>	Human	Forward	5' CAGCCTCGGACTTGGAAAC
		Reverse	5' GCTCCAGGGATGTCTGCTC
<i>SEMA3D</i>	Human	Forward	5' CTCAAGAAGGCAGTACCTCCGA
		Reverse	5' CGTCCACTTGTTTATCAGGCTGC
<i>SNAI2</i>	Human	Forward	5' TGGTTGCTTCAAGGACACAT
		Reverse	5' GTTGCAGTGAGGGCAAGAA
<i>TBX5</i>	Human	Forward	5' GGGCAGTGATGACATGGAG
		Reverse	5' GCTGCTGAAAGGACTGTGGT
<i>TCF21</i>	Human	Forward	5' CCCGAGAGTGACCTGAAAGA
		Reverse	5' GCTCCAGGTACCAAACCTCCA
<i>TNNT2</i>	Human	Forward	5' AGCATCTATAACTTGGAGGCAGAG
		Reverse	5' TGGAGACTTTCTGGTTATCGTTG
<i>WT1</i>	Human	Forward	5' TACACACGCACGGTGTCTTC
		Reverse	5' GGGCGTTTCTCACTGGTCT

### 2.2.3 Single-cell RNA sequencing

On days 2, 3, 4, 5, 7, 10, and 15 of epicardioid differentiation (performed with addition of 100 ng/mL VEGF from day 8), 6 to 13 epicardioids were dissociated to single cells using papain as previously described, with some modifications<sup>150</sup> (Table 3). Briefly, a 2x papain solution consisting of 40 U/mL papain (Worthington Biochemical Corporation; LS003124) and 2 mM L-cysteine (Sigma-Aldrich; C6852) in PBS<sup>-/-</sup> was incubated 10 min at 37°C to activate the papain before 1:2 dilution in PBS<sup>-/-</sup> to obtain the 1x solution. Spheroids were then carefully pushed out of the collagen gel using 10 µL tips if necessary and washed twice with 2 mM EDTA in PBS<sup>-/-</sup>. They were then dissociated in 750 µL 1x papain solution at 37°C and 750 rpm on a Thermomixer (Eppendorf, Germany). The optimal dissociation time was previously determined for each time point to consistently obtain a single cell suspension with the lowest possible proportion of dead cells and cell clumps, as both can negatively affect the quality of the resulting sequencing library (Table 3). The enzymatic reaction was stopped with 750 µL stop solution consisting of 1 mg/mL trypsin inhibitor (Sigma-Aldrich; T9253) in PBS<sup>-/-</sup>. After pipetting up and down approximately 30 times to obtain a single cell suspension, cells were

passed through a 40  $\mu\text{m}$  strainer washed with 5 mL 1% BSA (Gibco; 15260037) in PBS<sup>-/-</sup>. After centrifugation for 3 min at 200 g, cells were resuspended in 500  $\mu\text{L}$  0.5% BSA in PBS<sup>-/-</sup>. A 6  $\mu\text{L}$  sample of the suspension was then mixed with 6  $\mu\text{L}$  Trypan blue and 10  $\mu\text{L}$  were loaded into a Neubauer chamber to determine the cell number and percentage of dead cells. On days 2 to 10, the percentage of dead cells was below 3%. On day 15, it exceeded 10% and dead cells were immediately depleted using the Dead Cell Removal Kit (Miltenyi Biotec; 130-090-101) according to the manufacturer's instructions before proceeding further.

**Table 3: Conditions of single-cell dissociation for scRNA-Seq**

Time point	Number of epicardioids	Dissociation time
Day 2	13	45 min
Day 3	11	45 min
Day 4	10	45 min
Day 5	8	45 min
Day 7	8	50 min
Day 10	6	50 min
Day 15	6	55 min

After dissociation, the volume of cell suspension needed for a targeted cell recovery of 8,000 cells was collected for library preparation with the Chromium Single Cell 3' Reagent Kit v3 (10x Genomics; discontinued), the Chromium Single Cell 3' GEM, Library & Gel Bead Kit v3 (10x Genomics; PN-1000092), the Chromium Chip B Single Cell Kit (10x Genomics; PN-1000073), and the Chromium i7 Multiplex Kit v2 (10x Genomics; PN-120262) according to the manufacturer's instructions. Quality control of cDNA samples was performed by Dr. Rupert Öllinger on a Bioanalyzer (Agilent, Germany) using a High Sensitivity DNA kit (Agilent; 5067-4626) at the TranslaTUM (Munich, Germany). Library quantification was performed with the KAPA quantification kit (KAPA Biosystems; KK4824) following the manufacturer's instructions and a pool containing 5 nM of each library was sequenced on a NovaSeq 6000 (Illumina, San Diego, CA) with a read depth of 35,000 reads per cell at the German Research Center for Environmental Health (Helmholtz Zentrum Munich, Germany). Bioinformatical analysis of scRNA-Seq data was performed by Dr. Gianluca Santamaria. The Cell Ranger pipeline (v6.1.1) was used to perform sample demultiplexing, barcode processing

and generate the single-cell gene counting matrix. Briefly, samples were demultiplexed to produce a pair of FASTQ files for each sample. Reads containing sequence information were aligned using the reference provided with Cell Ranger (v6.1.1) based on the GRCh37 reference genome and ENSEMBL gene annotation. PCR duplicates were removed by matching the same UMI, 10x barcode and gene were collapsed to a single UMI count in the gene-barcode UMI count matrix. All the samples were aggregated using Cell Ranger with no normalization and treated as a single dataset. The R statistical programming language (v3.5.1) was used for further analysis.

Count data matrix was read into R and used to construct a Seurat object (v4.0.1). The Seurat package was used to produce diagnostic quality control plots and select thresholds for further filtering. Filtering method was used to detect outliers and high numbers of mitochondrial transcripts. These pre-processed data were then analyzed to identify variable genes, which were used to perform principal component analysis (PCA). Statistically significant PCs were selected by PC elbow plots and used for UMAP analysis. Clustering parameter resolution was set to 1 for the function `FindClusters()` in Seurat. For sub-clustering analysis, we used the `clustree` package (v0.4.3). All DEGs were obtained using Wilcoxon rank sum test using as threshold p-value  $\leq 0.05$ . We used adjusted p-value based on Bonferroni correction using all features in the dataset. For cell type-specific analysis, single cells of each cell type were identified using `FindConservedMarkers` function as described within the Seurat pipeline. Analysis of cell-cell interactions was performed with CellPhoneDB v2.0<sup>151</sup> by Dr. med. Alexander Gödel.

## 2.3 Immunofluorescence analysis

### 2.3.1 Cryosections

To prepare cryosections, spheroids were washed with DPBS with  $\text{Ca}^{2+}$  and  $\text{Mg}^{2+}$  (DPBS<sup>+/+</sup>; Sigma-Aldrich; D8662) and fixed with 4% PFA (Sigma-Aldrich; 158127) for 1 h at room temperature (RT). After washing 3 times for 5 min with DPBS<sup>+/+</sup>, they were kept in 30% sucrose at 4°C overnight (or for up to 3 days). For embedding, the bottom of 15 x 15 x 5 mm cryomolds was covered with 400  $\mu\text{L}$  10% sucrose/7.5% gelatin in DPBS<sup>+/+</sup> pre-warmed to 37°C and left to solidify at 4°C for 15 min. During this time, the organoids were covered with warm sucrose/gelatin solution and left to equilibrate at 37°C. The organoids were then carefully transferred to the cryomold with as little carryover of sucrose/gelatin solution as possible and placed at 4°C for 5 min. The molds were then filled with 500  $\mu\text{L}$  warm sucrose/gelatin solution and placed at 4°C for 20 min to solidify. For freezing, 2-methyl-butane (Sigma-Aldrich; M32631) was placed in a liquid nitrogen bath and cooled down for 2-3 min before immersing the cryomolds for 1-2 min until frozen. The samples were stored at -80°C before cutting 16  $\mu\text{m}$ -thick cryosections transferred onto poly-L-lysine slides (Thermo Fisher Scientific; J2800AMNT) with a Microm HM 560 cryostat (Thermo Fisher Scientific, Germany). Slides were left to dry for 30 min at RT before long-term storage at -80°C.

### 2.3.2 Immunostaining

For immunostaining, live cells were washed with DPBS<sup>+/+</sup> and fixed with 4% PFA for 15 min at RT, while cryosections were equilibrated at RT for 30 min after cutting or storage at -80°C and fixed with 4% PFA for 10 min at RT. After washing 3 times with DPBS<sup>+/+</sup>, cells or cryosections were permeabilized with 0.25% Triton X-100 (Sigma-Aldrich; X100) in DPBS<sup>+/+</sup> for 15 min at RT. After washing another 3 times with DPBS<sup>+/+</sup>, samples were blocked with 3% BSA in PBST, consisting of 0.05% Tween 20 (Sigma-Aldrich; P2287) in DPBS<sup>+/+</sup>, for at least 1 hour at RT. Primary antibodies (Table 4) were then added at the indicated dilutions in 0.5% BSA in PBST and incubated overnight at 4°C. After washing 3 times for 5 min (cells) or 5 times for 10 min (cryosections) with PBST, appropriate secondary antibodies diluted in 0.5% BSA (Sigma-Aldrich; A9647) in PBST were added for 1 hour (cells) or 2 hours (cryosections)

at RT, protected from light (Table 5). After repeating the previous washing steps, Hoechst 33258 (Sigma-Aldrich; 94403) was added at a final concentration of 5  $\mu\text{g}/\text{mL}$  in DPBS<sup>+/+</sup> for 15 min at RT, protected from light. After washing once with DPBS<sup>+/+</sup>, cells were then covered with fluorescence mounting medium (Dako; S3023) and (in the case of cryosections) with a cover slip and stored at 4°C until imaging with an inverted or confocal laser scanning microscope (DMI6000B and TCS SP8; Leica Microsystems, Wetzlar, Germany).

**Table 4: Primary antibodies used for immunostaining**

Target	Host species	Manufacturer	Catalog number	Concentration
CD31	Sheep	Miltenyi Biotec	130-106-503	1:200
CK-18	Mouse	Abcam	ab668	1:100
Collagen III	Rabbit	Invitrogen	MA1-26771	1:100
cTnT	Mouse	Thermo Fisher Scientific	MA512960	1:300
cTnT	Rabbit	Abcam	ab92546	1:300
E-cadherin	Mouse	Abcam	ab1416	1:100
Fibronectin	Rabbit	Abcam	ab2413	1:400
Ki67	Mouse	BD Biosciences	556003	1:300
ISL1	Mouse	Developmental Studies Hybridoma bank	39.4D5	1:100
MESP1	Rabbit	Thermo Fisher Scientific	PA5-67086	1:100
NKX2.5	Rabbit	Novus Biologicals	NBP1-31558	1:100
TCF21	Rabbit	Sigma-Aldrich	HPA013189	1:100
TBX18	Rabbit	Abcam	ab115262	1:100
Vimentin	Chicken	Abcam	ab24525	1:400
WT1	Rabbit	Merck	CA1026	1:100
ZO-1	Mouse	Thermo Fisher Scientific	33-9100	1:100

**Table 5: Secondary antibodies used for immunostaining**

Target species	Host species	Conjugate	Manufacturer	Catalog number	Concentration
Rabbit	Goat	Alexa Fluor 488	Invitrogen	A11008	1:500
Rabbit	Goat	Alexa Fluor 647	Invitrogen	A32733	1:500
Mouse	Goat	Alexa Fluor 594	Invitrogen	A11005	1:500
Mouse	Goat	Alexa Fluor 488	Invitrogen	A11001	1:500
Mouse	Goat	Alexa Fluor 647	Invitrogen	A21235	1:500
Chicken	Goat	Alexa Fluor 594	Invitrogen	A11042	1:500
Sheep	Donkey	Alexa Fluor 488	Invitrogen	A11015	1:500

## 2.4 Functional assays

### 2.4.1 Vibratome sectioning

To prepare live sections, spheroids were first carefully pushed out of the collagen gel using 10  $\mu$ L tips. An embedding solution consisting of 4% agarose was prepared by dissolving agarose (Biozym; 840004) in sterile DPBS<sup>+/+</sup> in a microwave and letting it cool down to approximately 50°C at RT. The spheroids were then transferred to a 3.5 mm dish, any residual medium was removed and the dish was filled with the agarose solution. Once the agarose had solidified, it was trimmed down to a block of approximately 1 cm x 1 cm x 1 cm with a scalpel and 250  $\mu$ m-thick slices were cut with a vibratome (VT1200S, Leica Biosystems, Germany) in a DPBS<sup>+/+</sup> bath following the manufacturer's instructions. The spheroid slices were then kept in CDM-maintenance medium for 3-5 days before functional assays.

### 2.4.2 Calcium imaging

Calcium imaging was performed as previously described, with some modifications<sup>149</sup>. Briefly, cardiomyocytes cultured in 2D or 250  $\mu$ m-thick spheroid slices were loaded with 1  $\mu$ M Fluo-4-AM (Thermo Fisher Scientific; F14201) in Tyrode's solution (135 mM NaCl, 5.4 mM KCl, 1 mM MgCl<sub>2</sub>, 10 mM glucose, 1.8 mM CaCl<sub>2</sub> and 10 mM HEPES, pH 7.35) containing 0.01% Pluronic F-68 (Gibco; 24040-032) for 50 min at 37°C. The solution was replaced with Tyrode's solution for 30 min at 37°C for de-esterification of the dye before imaging at 100 fps on an inverted epifluorescence microscope (DMI6000B, Leica Microsystems) equipped with a Zyla V sCMOS camera (Andor Technology, Germany). Pacing was performed with field stimulation electrodes (RC-37FS; Warner Instruments) connected to a stimulus generator (HSE Stimulator P; Hugo-Sachs Elektronik) providing depolarizing pulses at the indicated frequencies. The fluorescence of regions of interest relative to background regions was quantified in ImageJ (National Institutes of Health) and subsequent analysis was performed in RStudio<sup>152</sup> using custom-written scripts to determine the transient duration at 50% (TD<sub>50</sub>) or 90% decay (TD<sub>90</sub>).

### **2.4.3 Optical action potential measurements**

For optical action potential measurements, 250  $\mu\text{m}$ -thick slices of epicardioids derived from the AAVS1-CAG-VSFP hiPSC line were transferred to Tyrode's solution (see §2.4.2) before imaging at 100 fps on an inverted epifluorescence microscope (DMI6000B, Leica Microsystems) equipped with a Zyla V sCMOS camera (Andor Technology, Germany). The VSFP was excited at 480 nm and the emitted GFP and RFP fluorescence signals were separated using an image splitter (OptoSplit II, Caim Research, UK). The fluorescence of regions of interest relative to background regions was quantified in ImageJ (National Institutes of Health) and subsequent analysis was performed in RStudio<sup>152</sup> using custom-written scripts to determine the duration at 50% ( $\text{APD}_{50}$ ) or 90% repolarization ( $\text{APD}_{90}$ ).  $\text{APD}_{50}$  and  $\text{APD}_{90}$  maps were generated by aligning the split image stacks with a custom algorithm in MatLab (The MathWorks Inc), denoising them with the CANDLE algorithm<sup>153</sup> and calculating the ratio between the two. For each action potential, the APD was calculated directly based on the amplitude on each pixel. Maps were generated by Dr. Qinghai Tian (Saarland University, Germany).

### **2.4.4 Endothelin-1 treatment**

To induce a hypertrophic response, epicardioids generated as described in §2.1.7 were treated with 100 nM endothelin-1 (Sigma-Aldrich; E7764) in CDM-maintenance medium for 6 days, replacing the medium every day. At the end of the treatment, they were dissociated with TrypLE Express (Gibco; 12605010) for 15 min at 37°C for RNA extraction (see §2.2.1) or fixed for cryosectioning (see §2.3.1).

## 2.5 Gene editing

### 2.5.1 Ribonucleoprotein (RNP)-mediated CRISPR/Cas9 deletion of *DMD* exon 51 in DMD $\Delta$ 52 hiPSCs

CRISPR/Cas9-mediated deletion of *DMD* exon 51 in DMD $\Delta$ 52 patient hiPSCs was performed via the Alt-R CRISPR-Cas9 system (IDT) following the manufacturer's instructions, as previously described<sup>149</sup>. Briefly, CRISPR RNA oligonucleotides targeting the human *DMD* exon 51 locus (Table 6) were purchased from IDT and duplexed with fluorescently labeled tracrRNA (IDT; 1075927). The derived gRNAs were then each used to generate equimolar ribonucleoprotein (RNP) complexes with the *S. pyogenes* Cas9 protein (IDT; 1074181) in Opti-MEM medium (Gibco; 31985062). For transfection, DMD $\Delta$ 52 hiPSCs were washed with PBS<sup>-/-</sup> and dissociated to single cells with TrypLE Express for 5 min at 37°C, stopping the reaction with 5 vol DMEM/F-12. After centrifugation for 5 min at 300 g, cells were resuspended in mTeSR1 supplemented with 10  $\mu$ M Y27632 and counted with a Neubauer chamber. Transfection was performed with Lipofectamine Stem Transfection reagent (Invitrogen; STEM00003), applying a final RNP concentration of 10 nM for  $4 \times 10^5$  cells per well of a Matrigel-coated 96-well plate. Transfected cells were dissociated into single cells 24 hours later with a 10-minute Accutase treatment, and 1,000 cells were seeded into a Matrigel-coated 10 cm plate in mTeSR1 containing 10  $\mu$ M Y27632. mTeSR1 was replaced every day until colonies were large enough to cut in half for clone screening and passaging. Deletion of exon 51 was verified by genomic PCR (see §2.5.3) and Sanger sequencing by Eurofins Genomics (Germany). The generated DMD $\Delta$ 51-52 line was confirmed to have a normal karyotype by the Institute of Human Genetics of the Klinikum rechts der Isar, Technical University of Munich.

**Table 6: CRISPR RNA nucleotide sequences for the deletion of *DMD* exon 51**

Gene	Species	Name	Sequence
<i>DMD</i> (exon 51)	Human	gRNA 5-3	5' TAATTTGAAGCTGGACCCTA
		gRNA 3-1	5' GTCTAGGAGAGTAAAGTGAT

### 2.5.2 AAV-mediated CRISPR/Cas9 deletion of *DMD* exon 51 in *DMD* $\Delta$ 52 cardiomyocytes

AAV-mediated somatic gene editing was performed as previously described<sup>149</sup>. Briefly, cardiomyocytes differentiated from *DMD* $\Delta$ 52 patient hiPSCs with the protocol described in §2.1.6 were transduced with two adeno-associated viruses (AAVs) each carrying either the N-terminal or C-terminal sequence of a split-intein Cas9 protein and one of two gRNAs targeting *DMD* exon 51 (Table 6), referred to as AAV6-Cas9/gE51. Both AAVs were added to the cells at a concentration of  $10^6$  particles per cell and removed after 20 hours. Where indicated, cells were transduced with an equivalent dual AAV system additionally encoding either eGFP or mCherry (AAV6-N-Cas9-eGFP and AAV6-C-Cas9-mCherry).

### 2.5.3 Genomic PCR

For colony screening after CRISPR/Cas9 editing in *DMD* $\Delta$ 52 hiPSCs, isolated colonies were transferred in 2-3  $\mu$ L medium into PCR tubes containing 30  $\mu$ L colony screening buffer. Colony screening buffer was prepared by mixing 300  $\mu$ L Tris 1 M (Sigma-Aldrich; 1185-53-1) pH 8.0, 60  $\mu$ L EDTA 0.5 M (Invitrogen; AM9260G), 1.5 mL KCl 1 M (Sigma-Aldrich; 7447-40-7), 60  $\mu$ L MgCl<sub>2</sub> 1 M (Sigma-Aldrich; M8266), and 28 mL H<sub>2</sub>O; this solution was filter sterilized and 200  $\mu$ g/mL RNase A (Qiagen; 19101) and 670  $\mu$ g/mL Proteinase K (Sigma-Aldrich; P2308) were freshly added before use. Colonies were incubated for 3 h at 60°C and 2 min at 90°C in a FlexCycler2 PCR thermal cycler. The resulting cell lysate was used for colony PCR with the Platinum Taq DNA polymerase High Fidelity (Invitrogen; 11304011) and primers listed in Table 7, using the following program.

Stage	Temperature	Duration	Cycles
Initial denaturation	94°C	2 min	1
Denaturation	94°C	15 s	35
Annealing	67°C	15 s	
Extension	72°C	1 min	
Final extension	72°C	5 min	1

To detect the deletion of *DMD* exons 52 and 51 in *DMD* $\Delta$ 52 hiPSCs and AAV-treated hiPSC-CMs, respectively, total DNA was extracted from cells with the Genra Puregene kit (Qiagen; 158722) according to the manufacturer's instructions. Genomic PCR was performed with the Q5 High-Fidelity DNA Polymerase (NEB; M0491S) and the primers listed in Table 7, using the following program.

Stage	Temperature	Duration	Cycles
Initial denaturation	94°C	2 min	1
Denaturation	94°C	15 s	35
Annealing	61.1°C	30 s	
Extension	68°C	1 min	
Final extension	68°C	5 min	1

**Table 7: PCR primer sequences**

Gene	Species	Sequence	
<i>DMD</i> exon 51	Human	Forward	5' ATGCTTCCCACCTTTCCTTG
		Reverse	5' CCCCTTACTCTGTCTGCCTC
<i>DMD</i> exon 52	Human	Forward	5' TGGTCCACTCCGTTTTAGCCAT
		Reverse	5' TTAGCACACGCCTGTAATCCCA

PCR products were evaluated by agarose gel electrophoresis separation at 230 V in 1% agarose gels containing the DNA intercalator ethidium bromide followed by imaging with a Biovision 3000 WL transilluminator (Peqlab, Germany). The percentage of *DMD* exon 51 deletion after CRISPR/Cas9 editing was quantified based on PCR band intensity using ImageJ (National Institutes of Health).

#### 2.6.4 Capillary Western immunoassay

After gene editing, levels of dystrophin protein were quantified by capillary Western immunoassay as previously described<sup>149</sup>. Briefly, cardiomyocytes were lysed in RIPA buffer (Sigma-Aldrich; R0278) containing proteinase inhibitor (Roche; 11836170001). The total protein concentration was determined by Pierce BCA assay (Thermo Fisher Scientific; 23225). Dystrophin levels were quantified via the size-based Wes system (ProteinSimple, Germany) following the manufacturer's instructions, using an antibody targeting the C-terminus of

human dystrophin (Abcam; ab15277; concentration 1:12.5) and an antibody targeting  $\alpha$ -actin as a loading control (Abcam; ab3280; concentration 1:25). Samples were loaded at a protein concentration of 0.1 mg/mL.

## 2.7 Statistics

Statistical analysis was performed with GraphPad Prism version 9.1.0. (La Jolla California, USA). Results are presented in dot plots indicating the mean  $\pm$  SEM or in box-and-whiskers plots indicating the median, 25<sup>th</sup> and 75<sup>th</sup> percentile, with whiskers extending to the 5<sup>th</sup> and 95<sup>th</sup> percentiles, unless otherwise indicated. Normally distributed data from two experimental groups were compared by Student's t-test, otherwise a Mann-Whitney-Wilcoxon test was applied. Normally distributed data from more than two experimental groups were compared using one- or two-way analysis of variance (ANOVA). In the case of multiple comparisons, an appropriate post hoc test was applied as indicated. A p-value  $< 0.05$  was considered statistically significant.

## 3 Results

### 3.1 Generation of epicardioids from human pluripotent stem cells

#### 3.1.1 Retinoic acid promotes the self-organization of myocardial and epicardial layers in vitro

The generation of organoids relies on the self-patterning of cells upon minimal addition of signaling factors that drive developmental processes in vivo. During early cardiogenesis, a key regulator of anteroposterior patterning is retinoic acid (RA)<sup>154–156</sup>. Specifically, studies in murine and avian embryos have shown that retinoic acid limits the posterior expansion of the SHF by downregulating *Isl1* and activates the expression of *Tbx5*<sup>156,157</sup>.

In line with this, work from our lab and others has shown that retinoic acid modulation is sufficient to control the enrichment of first vs second heart field progenitors in vitro (Zawada et al., in preparation)<sup>147</sup>. This could be observed during 2D differentiation of hiPSCs with a protocol driving the sequential induction of anterior primitive streak, cardiac mesoderm and cardiovascular derivatives by modulation of Wnt, Activin A, BMP4, and bFGF signaling, either with or without retinoic acid (Fig. 11a). Although they showed similar expression dynamics of the pan-cardiac marker *NKX2.5*, cells treated with RA between days 2 and 6 of differentiation showed upregulation of the FHF marker *TBX5* from day 4, which was virtually absent in untreated cells (Fig. 11b). The canonical SHF marker *ISL1* was present in both conditions, but RA-treated cells showed significantly lower expression from day 4 (Fig. 11b). Consistent with FHF identity, they also showed fast differentiation into ventricular cardiomyocytes, as evidenced by the upregulation of the sarcomeric marker *TNNT2* and the early ventricular marker *MYL3* from day 5 (Fig. 11b).

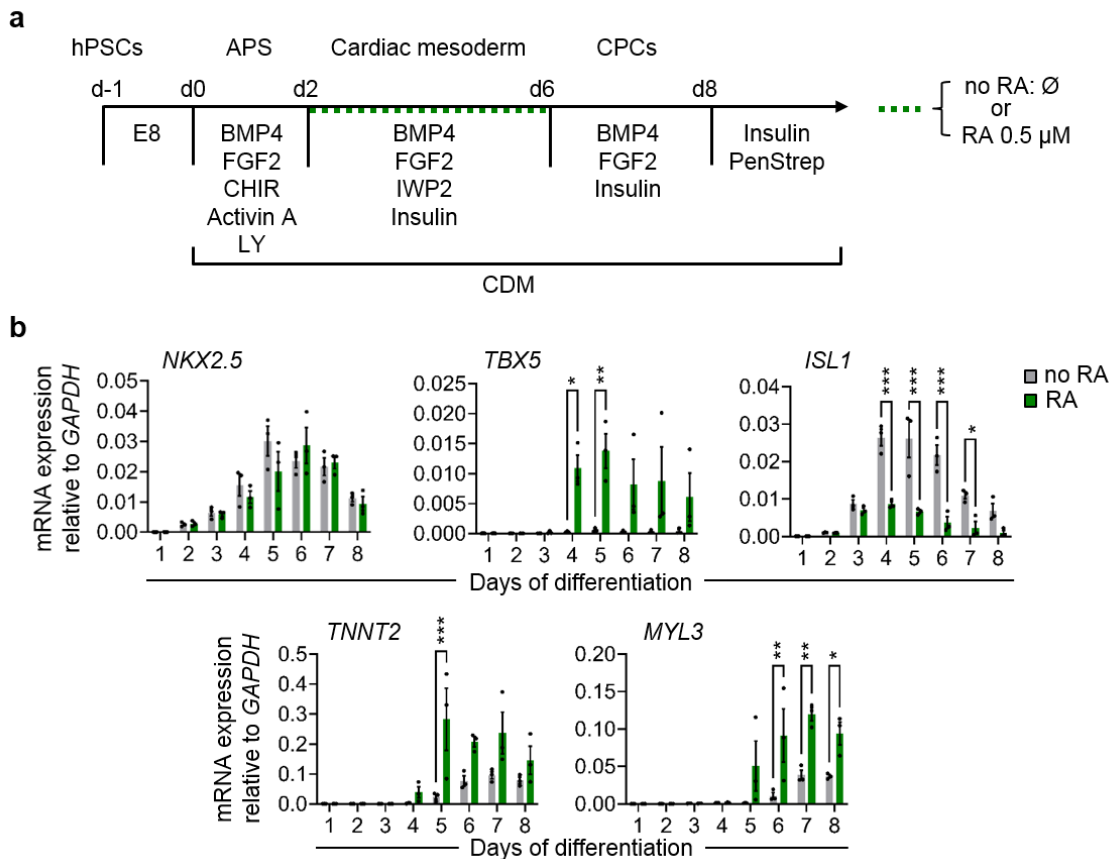


**Figure 11: Modulation of retinoic acid allows enrichment of FHF or SHF cardiac progenitor cells during in vitro cardiac differentiation of hPSCs. (a)** Graphical representation of the protocol used to differentiate human induced pluripotent stem cells (hPSCs) into cardiac cells via the induction of anterior primitive streak (APS), cardiac mesoderm and cardiac progenitor cells (CPCs), with or without addition of retinoic acid (“RA” and “no RA”, respectively) (see §2.1.3). E8: Essential 8 medium; CHIR: CHIR-99021; LY: LY-29004; PenStrep: Penicillin/Streptomycin. **(b)** Time course RT-qPCR analysis of cardiac markers from days 1 to 8 of hiPSC differentiation with the protocol described in (a), indicating mRNA expression levels relative to *GAPDH* expression. Mean  $\pm$  SEM are indicated; N = 3 differentiations/group; P-values determined by two-way ANOVA with Sidak’s multiple comparison test. \* $p < 0.05$ ; \*\* $p < 0.01$ ; \*\*\* $p < 0.0001$ .

In vivo, retinoic acid acts as a morphogen, driving organ patterning by induction of concentration-dependent cell responses<sup>158</sup>. We therefore hypothesized that in a 3D setting allowing the formation of signaling gradients, retinoic acid may influence not only cell specification but also self-organization. To test this, we generated spheroids by seeding 40,000 hiPSCs into low-attachment U-shaped 96-well plates and after 24 hours applied the same

---

cardiac induction media as previously, both with or without retinoic acid (Fig. 12a). Based on insights from other organoid systems, we additionally provided extracellular matrix support by embedding spheroids in a gel containing a high concentration of type I collagen, which represents up to 90% of cardiac extracellular matrix and contributes to both the structural and functional integrity of the heart<sup>159</sup>. This was implemented at day 8 of differentiation, when switching to maintenance medium (Fig. 12a). Collagen sheets containing spheroids were then kept in 6-well plates placed on a rocking shaker to improve oxygen and nutrient diffusion.

Differences in morphology quickly appeared between spheroids cultured with retinoic acid (RA) or without (no RA). Starting from a mean cross-sectional area of  $0.41 \pm 0.04 \text{ mm}^2$  on day 0, spheroids of the no RA group were already larger than the RA group by the end of RA treatment on day 6 (no RA:  $0.94 \pm 0.27 \text{ mm}^2$  vs RA:  $0.73 \pm 0.16 \text{ mm}^2$ ;  $p < 0.0001$ ) (Fig. 12b,c). RA spheroids then largely maintained the same size while no RA spheroids continued expanding (d15 no RA:  $1.88 \pm 0.6 \text{ mm}^2$  vs RA:  $0.78 \pm 0.2 \text{ mm}^2$ ;  $p < 0.0001$ ), (Fig. 12b,c). In addition, RA spheroids consistently displayed several rounded protrusions with smooth edges, most prominent between days 4 and 7, that were absent or much less pronounced in no RA spheroids (Fig. 12d).

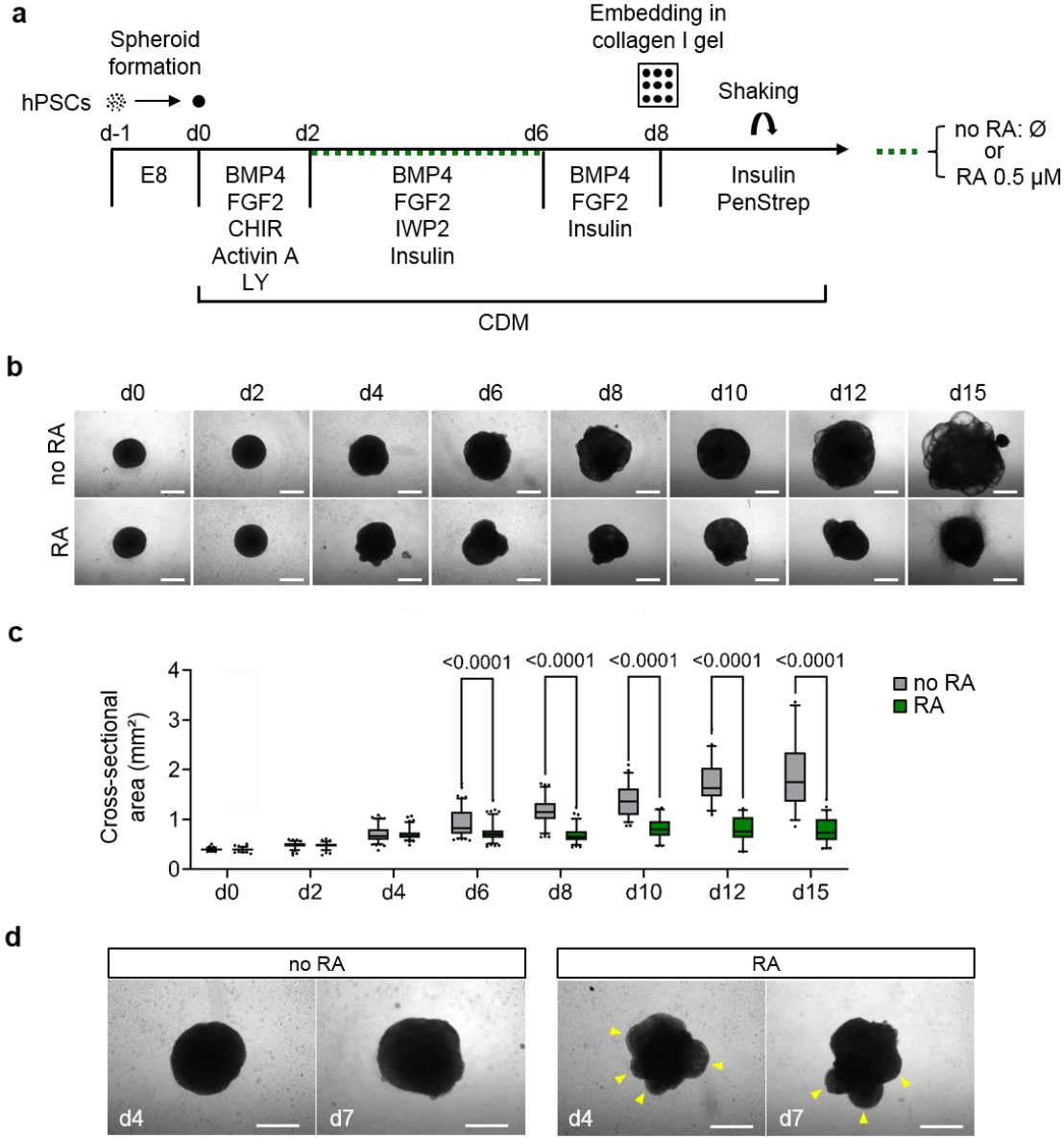


**Figure 12: Retinoic acid influences spheroid morphology during 3D cardiac induction of hPSCs.** (a) Graphical representation of the protocol used for 3D cardiac induction of hPSCs, with or without addition of retinoic acid (“RA” and “no RA”, respectively). E8: Essential 8 medium; CHIR: CHIR-99021; LY: LY-29004; PenStrep: Penicillin/Streptomycin. (b) Representative bright field images of spheroids at the indicated days of differentiation. Scale bars = 500 μm. (c) Cross-sectional area of spheroids at the indicated days of differentiation in mm<sup>2</sup>. N = 3 differentiations/group; no RA: n = 36-113 spheroids/day, RA: n = 36-116 spheroids/day; P-values determined by two-way ANOVA with Sidak’s multiple comparison test. (d) Representative bright field images of spheroids at days 4 and 7 of differentiation with or without RA. Scale bars = 500 μm. Yellow arrowheads indicate rounded protrusions typical of RA spheroids.

RA spheroids also started spontaneously beating earlier than no RA spheroids (around days 8 and 12, respectively; Fig. 13a), and their beating frequency was significantly faster, hinting to differences in myocytic differentiation (no RA:  $4.5 \pm 2.4$  beats/min vs RA:  $16.2 \pm 6.7$  beats/min;  $p < 0.0001$ ) (Fig. 13b).

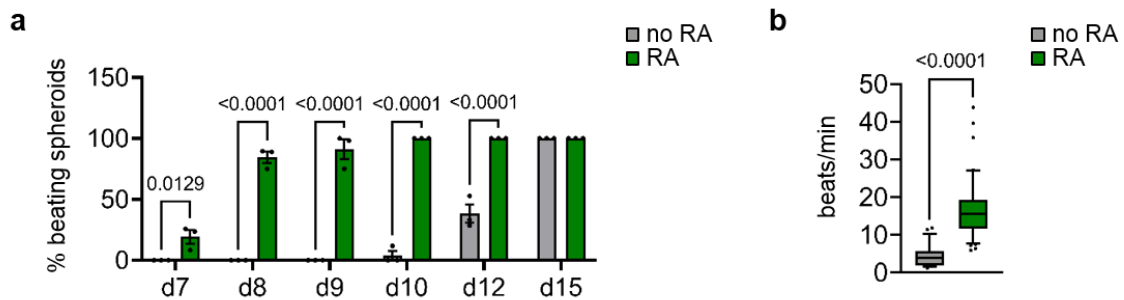


**Figure 13: Retinoic acid influences spontaneous beating behavior during 3D cardiac induction of hPSCs. (a)** Percentage of spontaneously beating spheroids at the indicated days of differentiation with retinoic acid (RA) or without (no RA); bars show the mean  $\pm$  SEM and all data points. N = 3 differentiations/group; no RA: n = 55 spheroids, RA: n = 96 spheroids. P-values determined by two-way ANOVA with Sidak's multiple comparison test. **(b)** Spontaneous beating frequency of spheroids at day 15 of differentiation with RA or without (no RA) in beats/minute. N = 6 differentiations/group; no RA: n = 53 spheroids, RA: n = 92 spheroids; P-value determined by unpaired two-tailed Mann-Whitney test.

Cell composition and organization were analyzed by immunofluorescence analysis of cryosections at day 15 of differentiation. Staining for the sarcomeric marker cardiac troponin T (cTnT) revealed that loosely organized cardiomyocytes represented the vast majority of cells in spheroids cultured without RA (Fig. 14a). By contrast, addition of RA led to the self-organization of an inner core mainly composed of cTnT<sup>+</sup> cardiomyocytes and an outer layer of cTnT<sup>-</sup> cells reminiscent of an epicardium (Fig. 14a). Indeed, this layer was positive for the human epicardial markers WT1, TBX18, TCF21 and vimentin<sup>160</sup> (Fig. 14b). Interestingly, only the outermost layer of these cells was positive for the epithelial markers ZO-1 and CK-18, suggesting a separation between an outer mesothelial layer and a subjacent region containing epicardial cells in the process of epithelial-mesenchymal transition (EMT) (Fig. 14b).

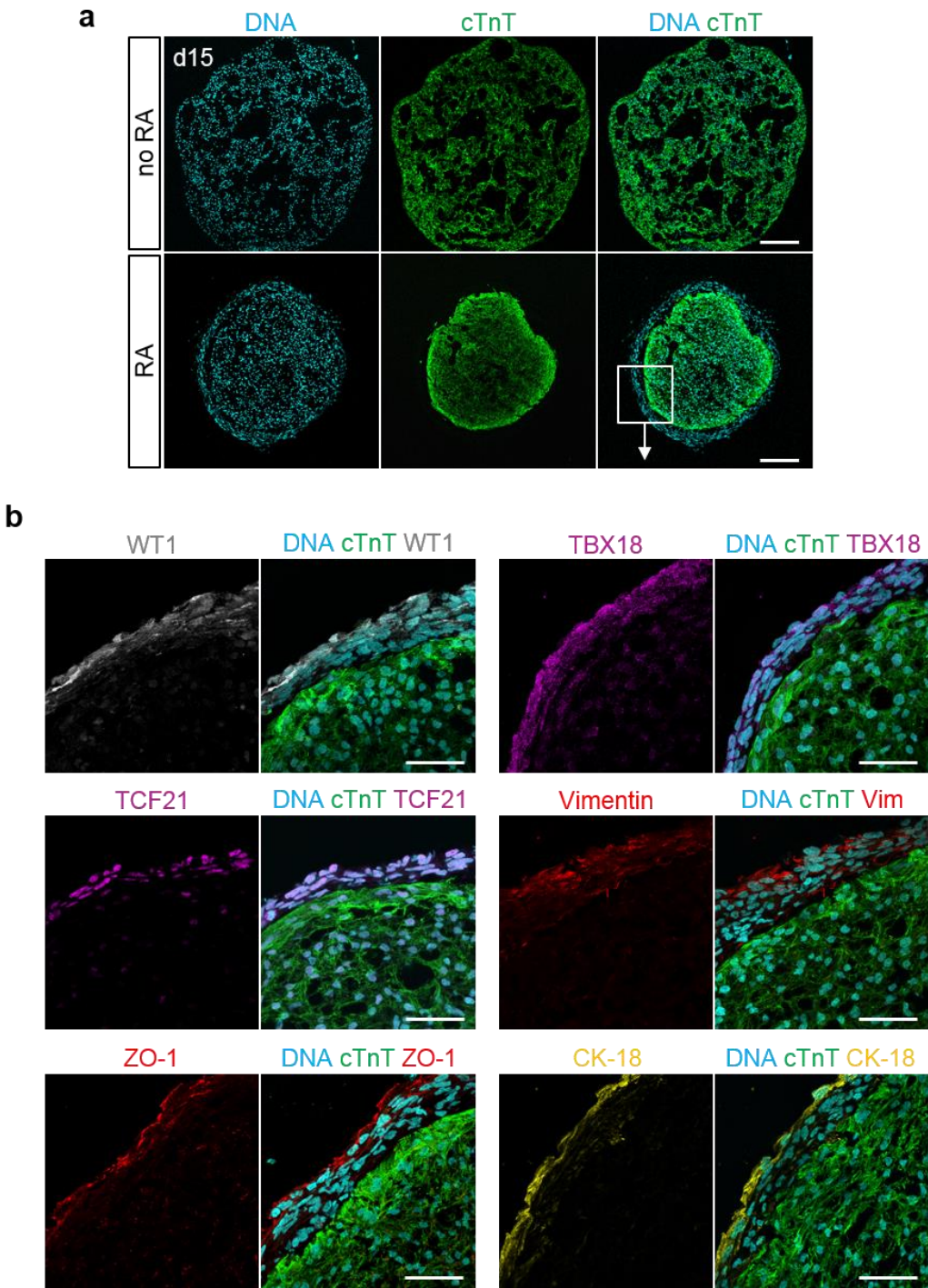


**Figure 14: Retinoic acid promotes the self-organization of an outer epicardial-like layer during 3D cardiac induction of hPSCs. (a)** Representative images of cTnT immunostaining of spheroids at day 15 of differentiation with retinoic acid (RA) or without (no RA). Scale bars = 200  $\mu$ m **(b)** Representative images of cTnT, TBX18, TCF21, vimentin (Vim), ZO-1 and cytokeratin-18 (CK-18) immunostaining of spheroids at day 15 of differentiation with retinoic acid. Scale bars = 50  $\mu$ m.

Importantly, this self-organization of myocardial and epicardial layers was reproducible in two other hiPSC lines as well as a hESC line, with similar efficiencies in obtaining a complete or at least partial epicardial layer (overall  $83.7 \pm 18.2\%$  and  $14.7 \pm 16.1\%$ , respectively, with  $1.5 \pm 4.7\%$  spheroids lacking this layer entirely) (Fig. 15a,b). However, the starting cell number needed to be adapted to each cell line, presumably due to differing proliferation rates, with the optimal number varying between 30,000 and 40,000 cells. Too few cells at day 0 – due to low starting cell number on day -1 or high cell death after seeding – resulted in small spheroids that often showed signs of cell death at the borders and never started beating (Fig. 15c). On the contrary, starting with too many cells led to large round spheroids with irregular edges instead of the expected smooth, rounded edges (Fig. 15c).

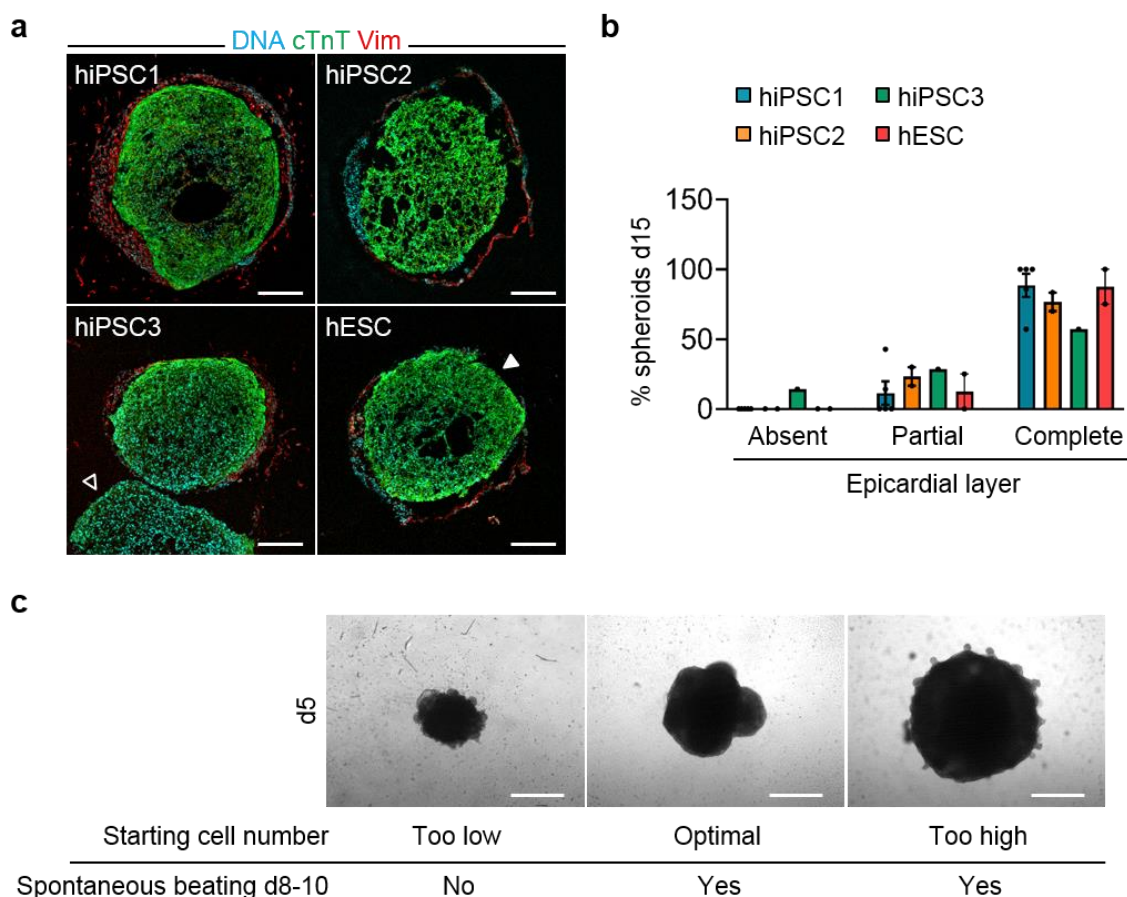


**Figure 15: The self-organization of myocardial and epicardial layers is reproducible in other hPSC lines after optimization of the starting cell number. (a)** Representative images of cTnT and vimentin (Vim) immunostaining of spheroids differentiated from four different hPSC lines (3 hiPSC lines and 1 hESC line) with retinoic acid (day 15). The white arrowhead indicates an example of a partial

epicardial layer, the empty arrowhead shows part of a spheroid without epicardial layer. Scale bars = 200  $\mu\text{m}$ . **(b)** Percentage of spheroids differentiated from the indicated hPSC lines with an absent, partial or complete epicardial layer at day 15 of differentiation with retinoic acid. Bars indicate the mean  $\pm$  SEM and all data points; hiPSC1 N = 5 differentiations, n = 33 spheroids; hiPSC2: N = 2 differentiations, n = 16 spheroids; hiPSC3: N = 1 differentiation, n = 7 spheroids; hESC: N = 2 differentiations, n = 8 spheroids. **(c)** Representative bright field images of spheroids at day 5 of differentiation with retinoic acid after starting with a cell number that was too low, optimal or too high for the hiPSC line used. The initiation of spontaneous beating around day 8 is indicated for each condition. Scale bars = 500  $\mu\text{m}$

We could confirm that the self-organization of the two layers was dependent on cardiac progenitor cell (CPC) induction having taking place in a 3D setting, as RA-treated cells differentiated in 2D until day 6 before aggregation into spheroids and embedding in collagen did not reproduce it (Fig. 16a,b).

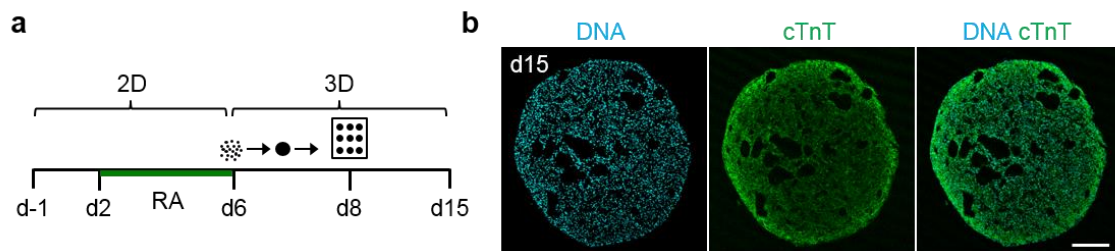


**Figure 16: The self-organization of the epicardial layer is dependent on CPC induction in 3D.** **(a)** Graphical representation of the protocol used for 2D cardiac induction of hiPSCs including retinoic acid treatment from day 2 to day 6 followed by spheroid formation on day 6 and collagen I embedding on day 8. **(b)** Corresponding representative images of cTnT immunostaining at day 15. Scale bar = 200  $\mu\text{m}$ .

The contribution of the collagen matrix to cell self-organization was also evaluated by leaving spheroids floating freely in medium until day 15. This did not have an effect on spheroid size or spontaneous beating frequency at day 15 (Fig. 17a-c). The formation of the epicardial layer was also largely maintained, but the efficiency was slightly reduced compared to spheroids having been embedded at day 8 (complete layer at day 15:  $55.3 \pm 29.8\%$ ; partial layer:  $39.8 \pm$

23.98%; absence of layer:  $4.7 \pm 8.2\%$ ) (Fig. 17d). Spheroids also showed higher disorganization (Fig. 17e), suggesting an overall positive effect of collagen embedding on the self-organization of the myocardial and epicardial layers.

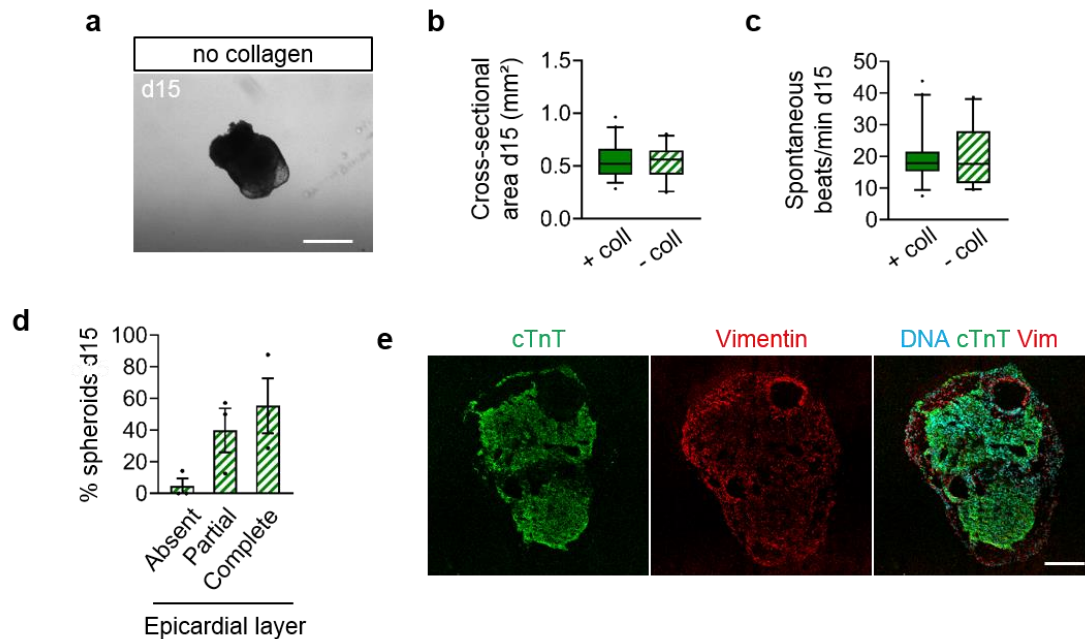


**Figure 17: Collagen embedding promotes the self-organization of the myocardial and epicardial layers.** (a) Representative bright field image of spheroids generated with retinoic acid but without collagen embedding, at day 15 of differentiation. Scale bar = 500  $\mu\text{m}$ . (b,c) Quantification of the cross-sectional area (b) and spontaneous beating frequency (c) of spheroids generated with or without collagen embedding within the same experiment (+ coll and - coll, respectively). N = 2 differentiations/group; + coll: n = 40 spheroids, - coll: n = 26 spheroids. (d,e) Percentage of spheroids showing an absent, partial, or complete epicardial layer at day 15 of differentiation without collagen embedding; bars show the mean  $\pm$  SEM and all data points. N = 3 differentiations, n = 23 spheroids. (d) Corresponding exemplary images of cTnT and vimentin (Vim) immunostaining at day 15. Scale bar = 200  $\mu\text{m}$ . (e)

Hereafter, spheroids generated with the protocol described in Fig. 12a, including retinoic acid addition and embedding in type I collagen, will be referred to as *epicardioids*. Spheroids generated with the same protocol except for the omission of retinoic acid will be referred to as control spheroids when comparing the two groups.

### 3.1.2 The epicardial layer is derived from ISL1<sup>+</sup> proepicardial progenitors segregating from the myocardial lineage during early epicardioid development

To understand the molecular processes underlying the segregation of the myocardial and epicardial lineages, we analyzed the early phases of epicardioid differentiation. By qRT-PCR analysis of key markers of primitive streak and cardiac mesoderm development described in human gastrulation<sup>161</sup>, we could observe the induction of the primitive streak around day 1 (characterized by *BRACHYURY*<sup>+</sup> *MESP1* cells), followed by nascent mesoderm around day 2 (*BRACHYURY*<sup>+</sup> *MESP1*<sup>+</sup>), emergent mesoderm at day 3 (*BRACHYURY*<sup>-</sup> *MESP1*<sup>+</sup>) and advanced mesoderm around day 4 (*MESP1* *HAND1*<sup>+</sup> *BMP4*<sup>+</sup>) (Fig. 18a). Of note, epicardioids also recapitulated the upregulation of *SNAI2*, a specificity of human gastrulation not observed in mice<sup>161</sup> (Fig. 18b). Immunofluorescence analysis showed that *MESP1*<sup>+</sup> mesodermal cells were evenly distributed within epicardioids and represented the vast majority of cells at day 3 (Fig. 18c).

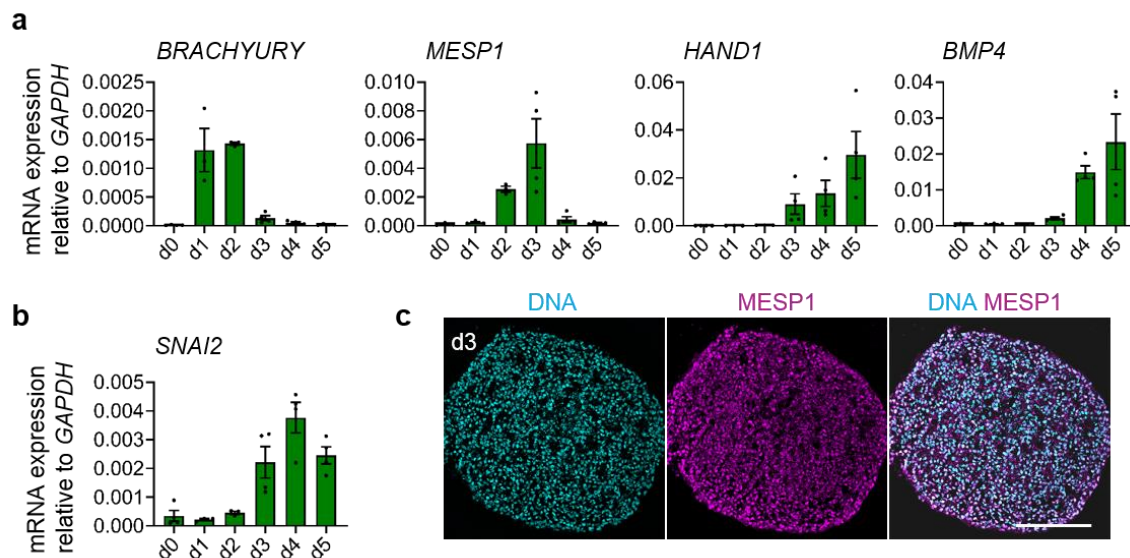


**Figure 18: Early epicardioids show stepwise upregulation of primitive streak and cardiac mesoderm markers. (a,b)** mRNA expression levels of *BRACHYURY*, *MESP1*, *HAND1*, *BMP4* (a) and *SNAI2* (b) relative to *GAPDH* at days 0, 1, 2, 3, 4, and 5 of epicardioid differentiation, as determined by qRT-PCR. Bars show the mean  $\pm$  SEM and all data points; N = 3 differentiations, n = 3-4 epicardioids/time point. **(c)** Representative images of *MESP1* immunostaining of an epicardioid at day 3 of differentiation. Scale bar = 200  $\mu$ m.

We then evaluated the expression of NKX2.5 and ISL1, two key regulators of cardiovascular progenitor specification<sup>162-164</sup>. Clusters of ISL1<sup>+</sup> cells first appeared on the outer edges of epicardioids on day 4 of differentiation; no NKX2.5 signal was visible at this stage (Fig. 19a). In some areas at the outer edge, a monolayer of mostly ISL1<sup>+</sup> cells appeared to detach from the rest (Fig. 19a). By day 5, the region of ISL1 expression was expanded and NKX2.5 was also present, allowing the distinction between a now continuous outer layer of ISL1<sup>+</sup> NKX2.5<sup>-</sup> cells and lobular areas of double-positive ISL1<sup>+</sup> NKX2.5<sup>+</sup> cells (Fig. 19b). This was maintained on day 6 (Fig. 19c). In addition, the outer layer of ISL1<sup>+</sup> NKX2.5<sup>-</sup> cells, which first appeared predominantly as a monolayer, had expanded to several layers by this point (Fig. 19c).

Differentiated cardiomyocytes could be identified by cTnT staining by day 7; virtually all were still positive for ISL1 (Fig. 20a). By contrast, the outer layer of ISL1<sup>+</sup> cells remained negative for cTnT, indicating a non-myocytic identity. Over the next week of culture, ISL1 was then progressively downregulated in cardiomyocytes but maintained in the outer layer, which ultimately formed the epicardial layer as described in Figure 14 (Fig. 20a-d). Only a subset of epicardial cells was positive for ISL1<sup>+</sup> on day 15 however, providing further evidence for their heterogeneity at this stage (Fig. 20d).

The expression of ISL1 in epicardial cells was somewhat unexpected, as in mice ISL1 is expressed in early proepicardial progenitors but not in epicardial cells<sup>165</sup>. For comparison, we generated hiPSC-derived epicardial cells via a protocol based on the induction of SHF CPCs followed by activation of Wnt signaling to induce proepicardial specification (Fig. 21a)<sup>85</sup>. This yielded WT1<sup>+</sup> proepicardial precursors that could be propagated under TGF- $\beta$  inhibition to obtain epicardial cells showing typical cobblestone morphology and expressing the same markers as the epicardial layer present in epicardioids: WT1, TBX18, TCF21, cytokeratin 18 (CK-18), ZO-1, and vimentin (Vim) (Fig. 21b,c). We found that ISL1 expression was also maintained from the proepicardial to the epicardial stage in these cells, pointing to a potential difference between murine and human epicardial cells (Fig. 21d).

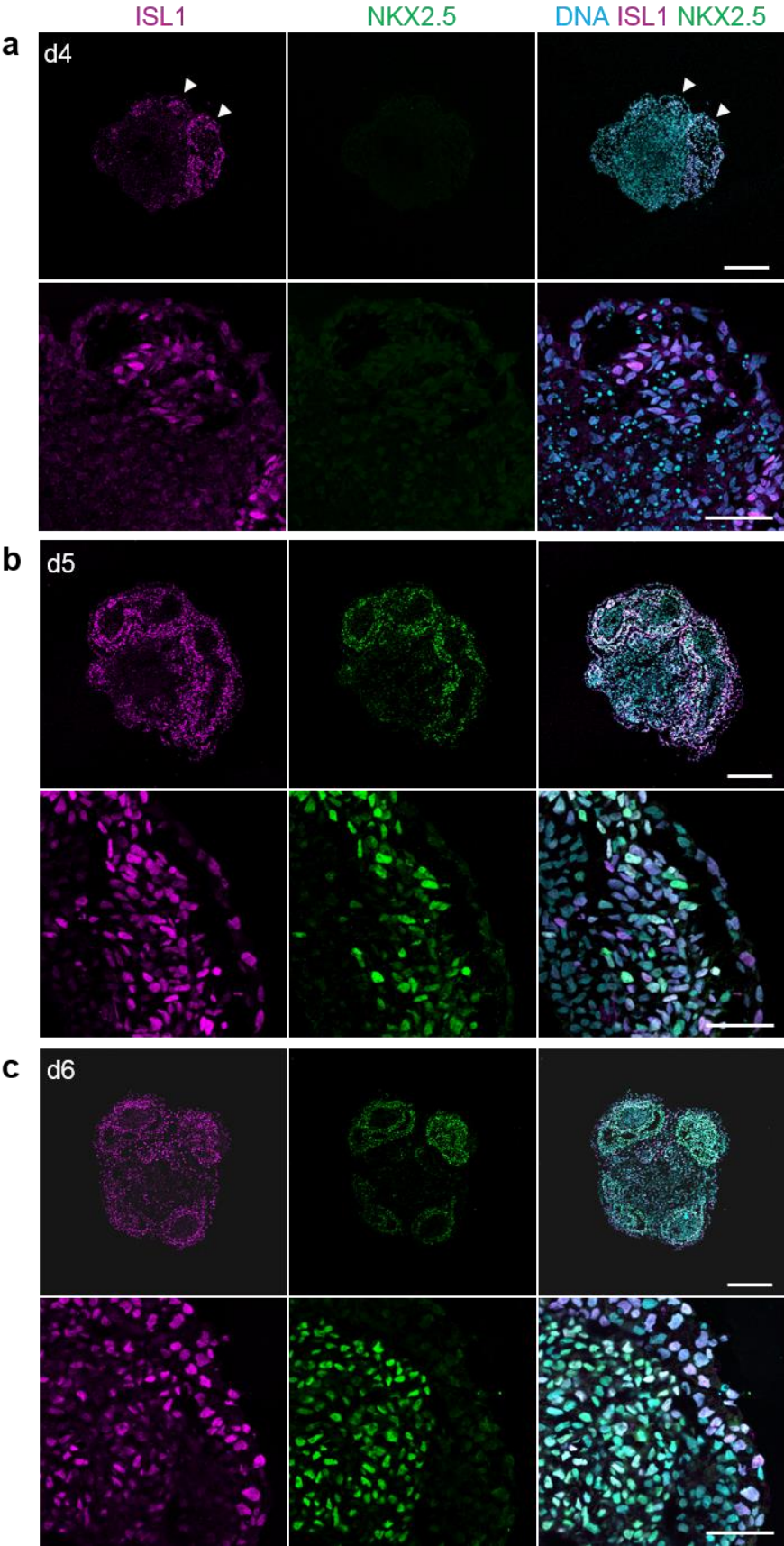


**Figure 19: Epicardioids show spatial segregation of ISL1<sup>+</sup> NKX2.5<sup>-</sup> and ISL1<sup>+</sup> NKX2.5<sup>+</sup> progenitors around day 5. (a-c)** Representative images of ISL1 and NKX2.5 immunostaining of epicardioids at days 4 (a), 5 (b), and 6 (c) of differentiation. Scale bars top = 200  $\mu$ m; bottom = 50  $\mu$ m. Arrowheads indicate first areas of outer layer formation on day 4.

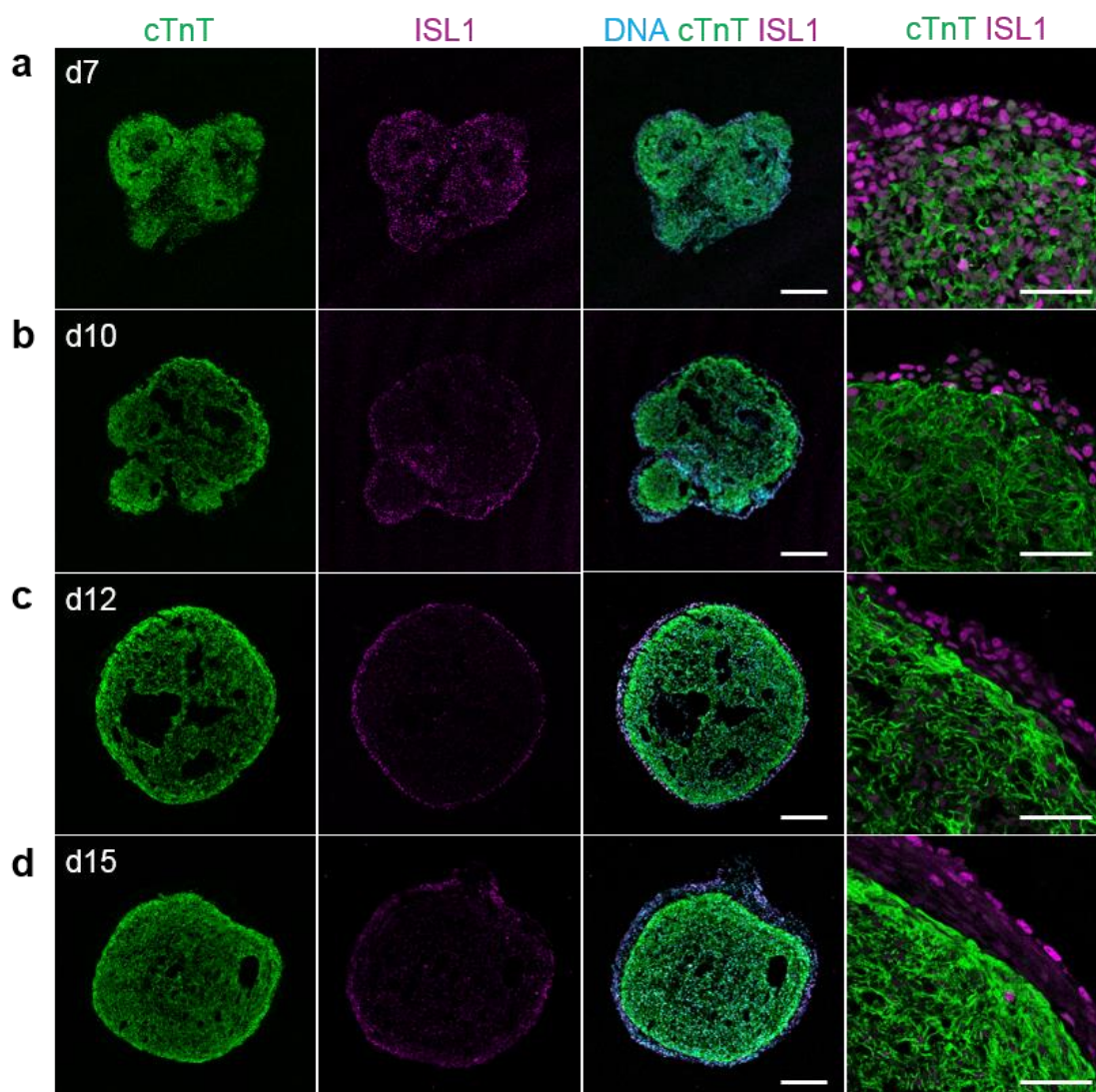


**Figure 20: ISL1 expression is maintained in the outer layer during epicardioid development. (a-d)** Representative images of ISL1 and cTnT immunostaining of epicardioids at days 7 (a), 10 (b), 12 (c), and 15 (c) of differentiation. Scale bars left = 200  $\mu$ m; right = 50  $\mu$ m.



### **3.1.3 The epicardial layer is partially formed but not maintained in the absence of retinoic acid**

To better understand the role of retinoic acid in promoting the formation of the epicardial layer, we next analyzed the development of control spheroids generated without it.

Immunofluorescence analysis at day 4 of differentiation showed that the region of ISL1 expression, forming a circle around the outer edge, was more extensive than in epicardioids at the same stage of differentiation (Fig. 22a). On day 5, areas of ISL1<sup>+</sup> NKX2.5<sup>-</sup> emerged at the outer layer, which became more prominent on day 6, suggesting a similar process as in epicardioids (Fig. 22b,c). Interestingly, the region of ISL1<sup>+</sup> cells still formed a single circle on days 5-6 instead of individual lobes as seen in epicardioids, consistent with the outer morphology observed during live imaging (Fig. 22d, Fig. 12d).

The morphological differences increased from day 7, as segments of ISL1<sup>+</sup> cTnT<sup>-</sup> cells at the outer layer progressively diminished until they were entirely absent on day 15 as previously described in Figure 14 (Fig. 23a-d). This suggested that the epicardial layer was partially formed but not maintained. The lower compaction in control spheroids compared to epicardioids was also apparent from day 10 (Fig. 23a-d).

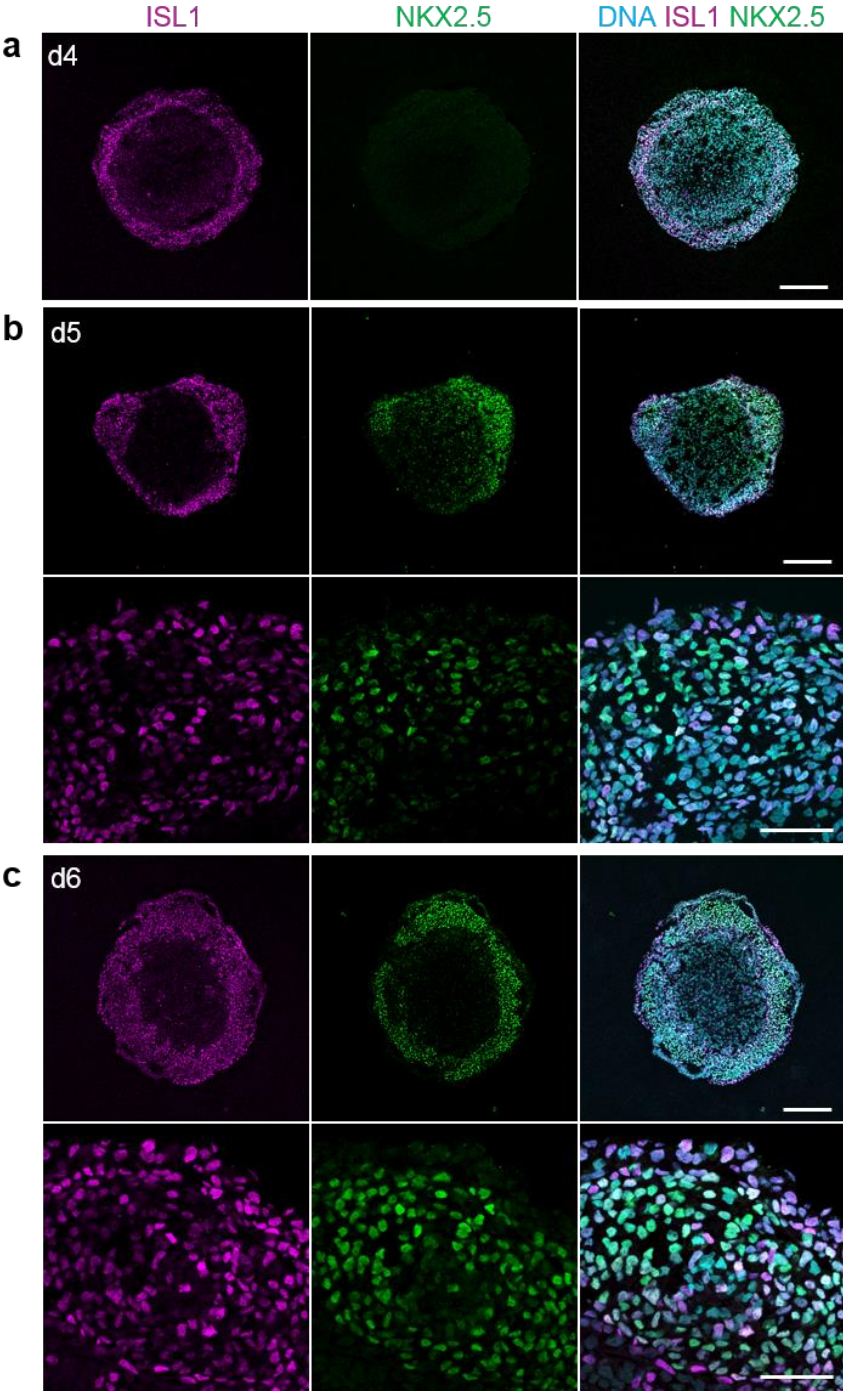


**Figure 22: Early control organoids show different spatial organization of ISL1<sup>+</sup> NKX2.5<sup>-</sup> and ISL1<sup>+</sup> NKX2.5<sup>+</sup> progenitors than epicardioids. (a-c)** Representative images of ISL1 and NKX2.5 immunostaining of control spheroids at days 4 (a), 5 (b), and 6 (c) of differentiation. Scale bars top = 200  $\mu\text{m}$ ; bottom = 50  $\mu\text{m}$ .

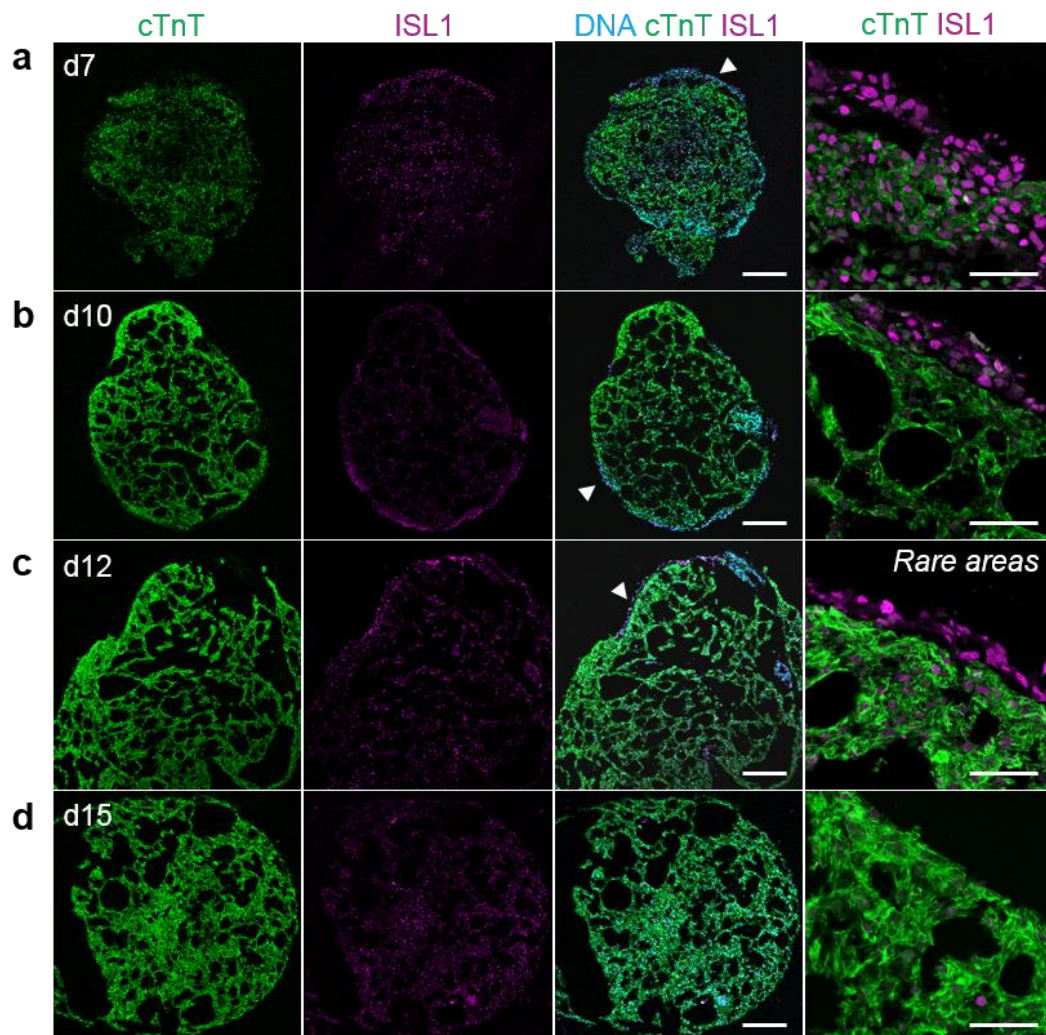


**Figure 23: An ISL1<sup>+</sup> outer layer is partially formed but not maintained in control spheroids. (a-d)** Representative images of ISL1 and cTnT immunostaining of control spheroids at days 7 (a), 10 (b), d12 (c), and 15 (c) of differentiation. Arrowheads indicate examples of areas showing a cTnT<sup>+</sup> ISL1<sup>+</sup> outer layer. Scale bars left = 200  $\mu$ m; right = 50  $\mu$ m.

Consistent with these immunofluorescence results, time course qRT-PCR analysis from the start of RA treatment on day 2 until day 15 showed that *ISL1* expression was higher in early control spheroids (days 3-4) but was maintained longer in epicardioids (Fig. 24). As was the case during 2D differentiation (Fig. 11), the addition of retinoic acid induced significantly higher expression of the FHF marker *TBX5* in epicardioids, while expression levels of the pan-cardiac marker *NKX2.5* were largely equivalent between the two groups (Fig. 24). *TNNT2* expression was also higher in epicardioids around days 7-9, in line with their initiation of spontaneous beating at this stage (Fig. 24).

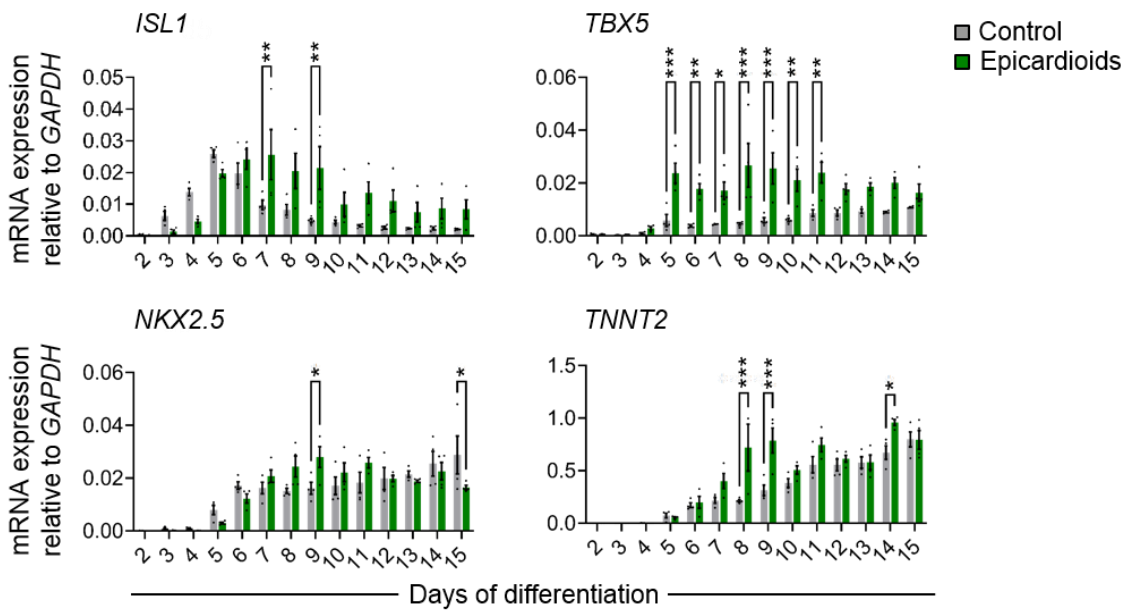


**Figure 24: Time course analysis of key cardiac markers in epicardioids compared to control spheroids.** mRNA expression levels of *ISL1*, *TBX5*, *NKX2.5*, and *TNNT2* relative to *GAPDH* at the indicated days of epicardioid or control spheroid differentiation, as determined by qRT-PCR. Bars show the mean  $\pm$  SEM and all data points; N = 3 differentiations; n = 4/time point. P-values determined by two-way ANOVA with Sidak's multiple comparison test. \* $p < 0.05$ ; \*\* $p < 0.01$ ; \*\*\* $p < 0.0001$ .

We next evaluated the expression dynamics of genes associated with the development of the (pro)epicardium in vivo. In both conditions, expression of *WT1* and *TBX18* was relatively low, and control spheroids unexpectedly showed higher *WT1* expression than epicardioids between days 5 and 10 (Fig. 25). By contrast, control spheroids had a transient peak of *TCF21* expression around day 4 while epicardioids showed significantly higher upregulation as well as maintenance of this gene in the following days (Fig. 25). *SEMA3D* was progressively upregulated during epicardioid development, while it remained virtually absent in control spheroids (Fig. 25). *SCX*, which marks a subset of epicardial cells in vivo, was not detected in either group (data not shown).

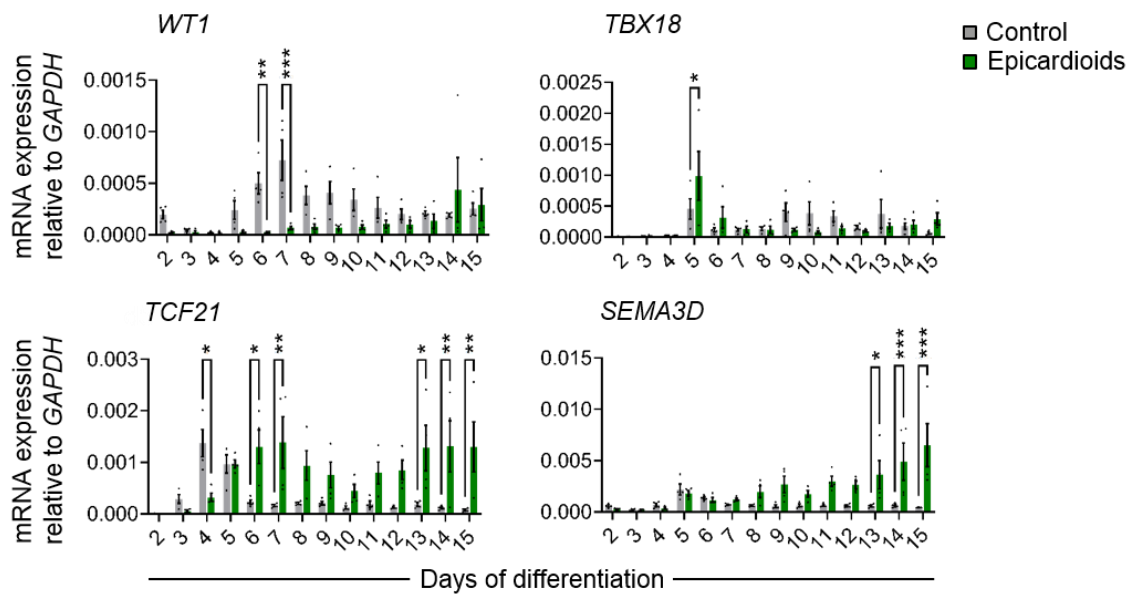


**Figure 25: Time course analysis of (pro)epicardial markers in epicardioids compared to control spheroids.** mRNA expression levels of *WT1*, *TBX18*, *TCF21*, and *SEMA3D* relative to *GAPDH* at the indicated days of epicardioid or control spheroid differentiation, as determined by qRT-PCR. Bars show the mean  $\pm$  SEM and all data points; N = 3 differentiations; n = 4/time point P-values determined by two-way ANOVA with Sidak's multiple comparison test. \* $p < 0.05$ ; \*\* $p < 0.01$  \*\*\* $p < 0.0001$ .

Several groups have recently described a population of multipotent progenitors marked by *MAB21L2* contributing to both myocardium and epicardium during mouse development<sup>40,41</sup>. Transcriptional profiling and lineage tracing defined these cells as a previously unrecognized subset of the first heart field, which has not yet been studied in humans<sup>40,41</sup>. For clarity, these cells will be referred to here as the juxta-cardiac field (JCF), a term coined by Tyser et al. based on their position relative to the cardiac crescent<sup>40</sup>. The transcription factors *HAND1* and *HOXB6* have been identified as key regulators of this cell population<sup>41</sup>. Control spheroids and epicardioids had similar expression dynamics of *MAB21L2* and *HAND1*, with faster upregulation of *HAND1* in early control spheroids (Fig. 26). However, there was a striking difference in the expression of *HOXB6*, which was upregulated from day 6 in epicardioids and remained virtually absent in control spheroids (Fig. 26).

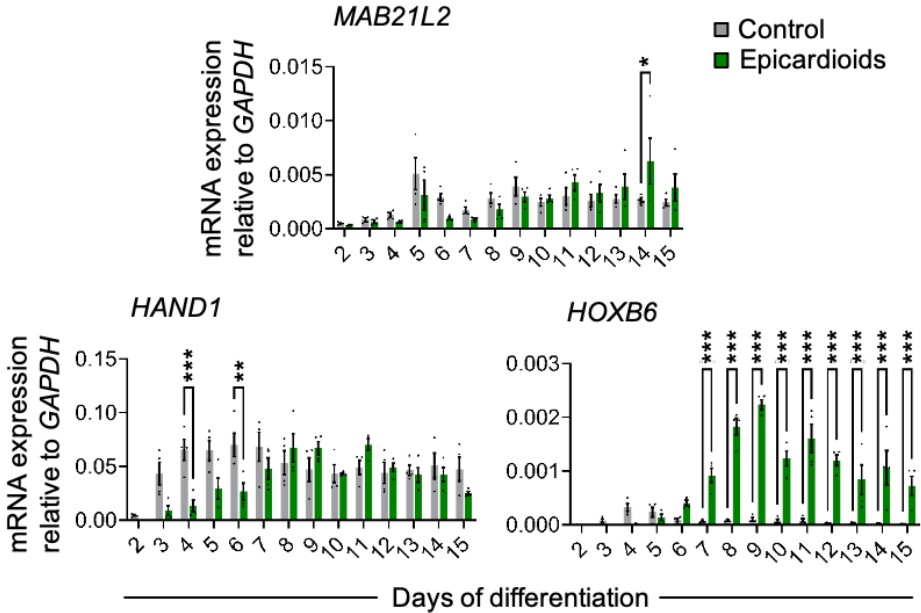


**Figure 26: Time course analysis of juxta-cardiac field (JCF) markers in epicardioids compared to control spheroids.** mRNA expression levels of *HAND1*, *MAB21L2*, and *HOXB6* relative to *GAPDH* at the indicated days of epicardioid or control spheroid differentiation, as determined by qRT-PCR. Bars show the mean  $\pm$  SEM and all data points; N = 3 differentiations; n = 4/time point. P-values determined by two-way ANOVA with Sidak's multiple comparison test. \*p < 0.05; \*\*p < 0.01; \*\*\*p < 0.0001.

## 3.2 Epicardioids recapitulate morphological, functional, and cellular features associated with the epicardium in vivo

### 3.2.1 Epicardioids show morphological patterning

In vivo, early myocardial patterning into the outer compact myocardium and inner trabecular myocardium is characterized by higher mitotic activity in the outer layer that is driven in part by signals emanating from the epicardium<sup>166</sup>.

A zone of higher cardiomyocyte compaction was also apparent underneath the epicardial layer in epicardioids (Fig. 27a). At day 15, the width of this zone varied between approximately 40 to 60  $\mu\text{m}$  as visible by eye. However, for unbiased quantifications, an arbitrary border between the outer layer of cardiomyocytes (OL) and the inner layer (IL) was set at 50  $\mu\text{m}$  from the outer edge of the myocardial layer across all samples. By quantifying the number of cardiomyocytes per  $\text{mm}^2$ , we could confirm that epicardioids had significantly higher density in the outer layer compared to the inner layer (OL:  $6,577 \pm 1,510$  CMs/ $\text{mm}^2$  vs IL:  $4,464 \pm 1,048$  CMs/ $\text{mm}^2$ ;  $p < 0.0001$ ), corresponding to an OL/IL ratio of  $1.5 \pm 0.2$  (Fig. 27a-c). This was not the case in control spheroids lacking the epicardial layer. In addition to having lower overall density (control:  $4,015 \pm 650.2$  CMs/ $\text{mm}^2$  vs epicardioids:  $5,521 \pm 1,225$  CMs/ $\text{mm}^2$ ;  $p = 0.0002$ ; data not shown), there was no difference between the outer and inner layer (OL:  $4,006 \pm 644.7$  CMs/ $\text{mm}^2$  vs IL:  $4,023 \pm 825.1$  CMs/ $\text{mm}^2$ ), resulting in an OL/IL ratio of  $1.0 \pm 0.2$  (Fig. 27a-c).

Immunostaining of Ki67, which is expressed during all phases of an active cell cycle<sup>167</sup>, showed that the higher density in the OL of epicardioids was associated with a twice higher percentage of Ki67<sup>+</sup> CMs compared to the IL (OL:  $23.9 \pm 7.9\%$  Ki67<sup>+</sup> CMs vs IL:  $11 \pm 4.9\%$ ;  $p < 0.0001$ ) (Fig. 27d,e). Although there was also a slightly higher percentage of Ki67<sup>+</sup> CMs in the OL of control spheroids (OL:  $28.8 \pm 5.3\%$  Ki67<sup>+</sup> CMs vs IL:  $24 \pm 2\%$ ;  $p = 0.0111$ ), the corresponding OL/IL ratio was significantly lower than in epicardioids (no RA:  $1.2 \pm 0.2$  vs RA:  $2.3 \pm 0.5$ ;  $p < 0.0001$ ) (Fig. 27d-f). The higher overall percentage of Ki67<sup>+</sup> CMs of control spheroids, coupled with their lower density, explains their large size described in Figure 12b,c (control:  $26.5 \pm 4.6\%$  Ki67<sup>+</sup> CMs vs epicardioids:  $17.5 \pm 6.1\%$  Ki67<sup>+</sup> CMs;  $p = 0.005$ ; data not shown).

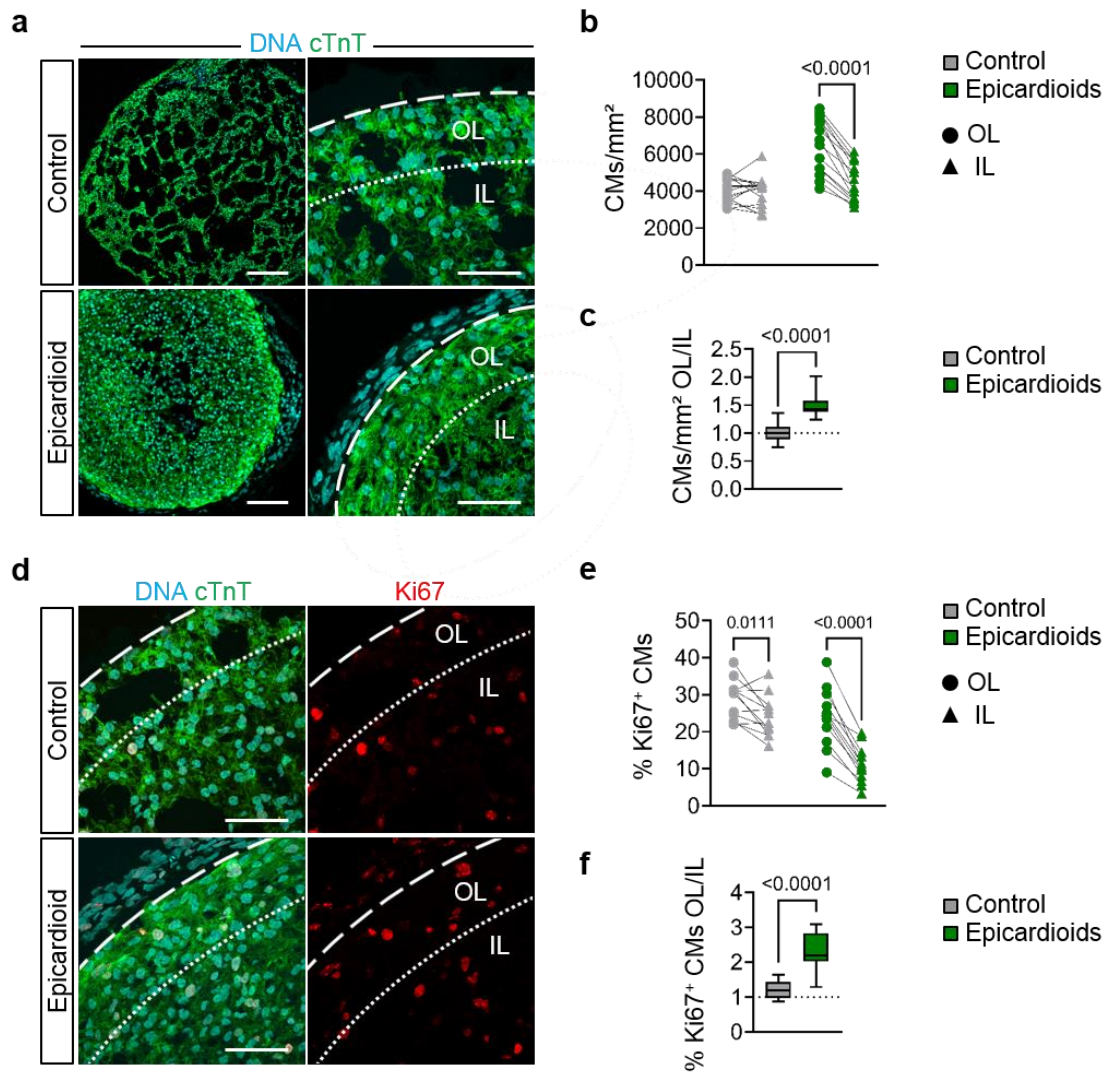


**Figure 27: The epicardial layer is associated with the formation of a subepicardial compact zone showing increased cardiomyocyte proliferation. (a,d)** The hatched lines mark the outer edge of the myocardial layer while the dotted lines mark the delimitation between the outer layer of cardiomyocytes (OL, within 50  $\mu\text{m}$  of the outer edge) and the inner layer (IL). **(a)** Representative images of cTnT immunostaining of control spheroids and epicardioids at day 15 of differentiation. Scale bars left = 100  $\mu\text{m}$ , right = 50  $\mu\text{m}$ . **(b)** Quantification of the density of cardiomyocytes (in CMs/mm<sup>2</sup>) in the OL and IL at day 15. Dot plot showing all data points, lines connect the values for OL and IL within the same spheroid. N = 15 spheroids from 3 differentiations per group; P-value determined by 2-way ANOVA matching paired data with Sidak's multiple comparison test. **(c)** Ratio of CM density between OL and IL at day 15. N = 15 spheroids from 3 differentiations per group; P-value determined by unpaired two-tailed *t*-test. **(d)** Representative images of cTnT and Ki67 immunostaining of control spheroids and epicardioids at day 15. Scale bars = 50  $\mu\text{m}$ . **(e)** Percentage of Ki67<sup>+</sup> CMs in OL and IL at day 15. Dot plot showing all data points, lines connect the values for OL and IL within the same

spheroid. N = 12 spheroids from 3 differentiations per group; P-value determined by 2-way ANOVA matching data with Sidak's multiple comparison test. **(f)** Ratio of the percentage of Ki67<sup>+</sup> CMs between OL and IL at day 15. N = 12 spheroids from 3 differentiations per group; P-value determined by unpaired two-tailed *t*-test.

### 3.2.2 Epicardioids show functional patterning

In the human heart, the wave of depolarization triggering contraction travels from the apex to the base and from the endocardium to the epicardium. The wave of repolarization, in turn, travels in the opposite direction. This means that cardiomyocytes closest to the epicardium are the last to be depolarized and the first to be repolarized, which is reflected in the shorter duration of their action potentials compared to cells close to the endocardium and those in the middle layer<sup>168</sup>. Hypothesizing that the morphological patterning described in Figure 27 could be associated with functional patterning, we next analyzed electrophysiological features of cardiomyocytes in the outer and inner layers of epicardioids.

As excitation-contraction coupling is dependent on the intracellular dynamics of calcium, we first compared calcium transients during contraction in cardiomyocytes of the outer layer (OL) and inner layer (IL). This was done after 30 days of culture to allow maturation of the cardiomyocytes. To allow simultaneous analysis of cardiomyocytes in OL and IL, 250  $\mu\text{m}$ -thick sections were prepared with a vibratome. The slices were then loaded with the calcium-binding fluorescent indicator Fluo-4. Upon excitation at a wavelength of 480 nm, Fluo-4 emits at 525 nm and an increase in emitted fluorescence reflects a rise in cytoplasmic  $\text{Ca}^{2+}$  levels. As an additional control, the same procedure was applied to control spheroids. Age-matched slices of both groups were recorded under 0.5 Hz pacing conditions to ensure equivalent conditions.

This showed that in epicardioids, calcium transients had a significantly shorter time to 50% peak decay ( $\text{TD}_{50}$ ) and 90% peak decay ( $\text{TD}_{90}$ ) in cardiomyocytes of the OL compared to the IL ( $\text{TD}_{50}$  OL:  $0.72 \pm 0.18$  s vs IL:  $0.83 \pm 0.18$  s;  $p < 0.0001$ ;  $\text{TD}_{90}$  OL:  $1.21 \pm 0.23$  s vs IL:  $1.35 \pm 0.22$  s;  $p < 0.0001$ ) (Fig. 28a-c).

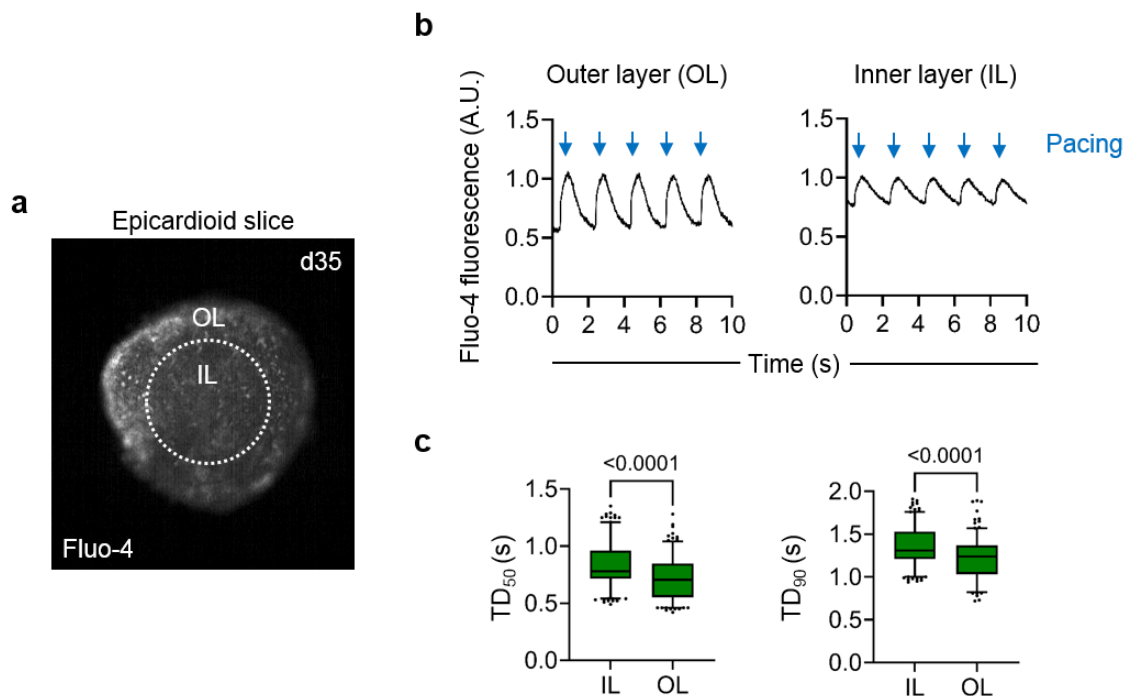


**Figure 28: Epicardioids show a decrease in calcium transient duration in the subepicardial outer layer.** (a) Representative image of an epicardioid slice loaded with Fluo-4 for calcium transient imaging at day 35. The dotted line defines the outer layer (OL) and inner layer (IL) of the epicardioid. (b,c) Exemplary traces of Fluo-4 fluorescence in the IL and OL under 0.5 Hz pacing conditions. (b) Corresponding quantification of TD<sub>50</sub> (the duration until 50% peak decay, left) and TD<sub>90</sub> (the duration until 90% peak decay, right) (c) in the OL and IL. N = 3 differentiations; n = 200 transients per layer from 9 epicardioids. P-values obtained by unpaired two-tailed *t*-test.

Control spheroids showed a smaller difference in calcium transient duration between OL and IL, with largely equal TD<sub>90</sub> in cardiomyocytes of the two layers (TD<sub>90</sub> OL:  $1.72 \pm 0.12$  s vs IL:  $1.68 \pm 0.15$  s) and, in contrast to epicardioids, slightly longer TD<sub>50</sub> in the OL (TD<sub>50</sub> OL:  $1.24 \pm 0.12$  s vs IL:  $1.23 \pm 0.19$  s;  $p < 0.0001$ ) (Fig. 29a-c). This indicated that the functional patterning observed in epicardioids is not an inherent property of cardiac spheres.

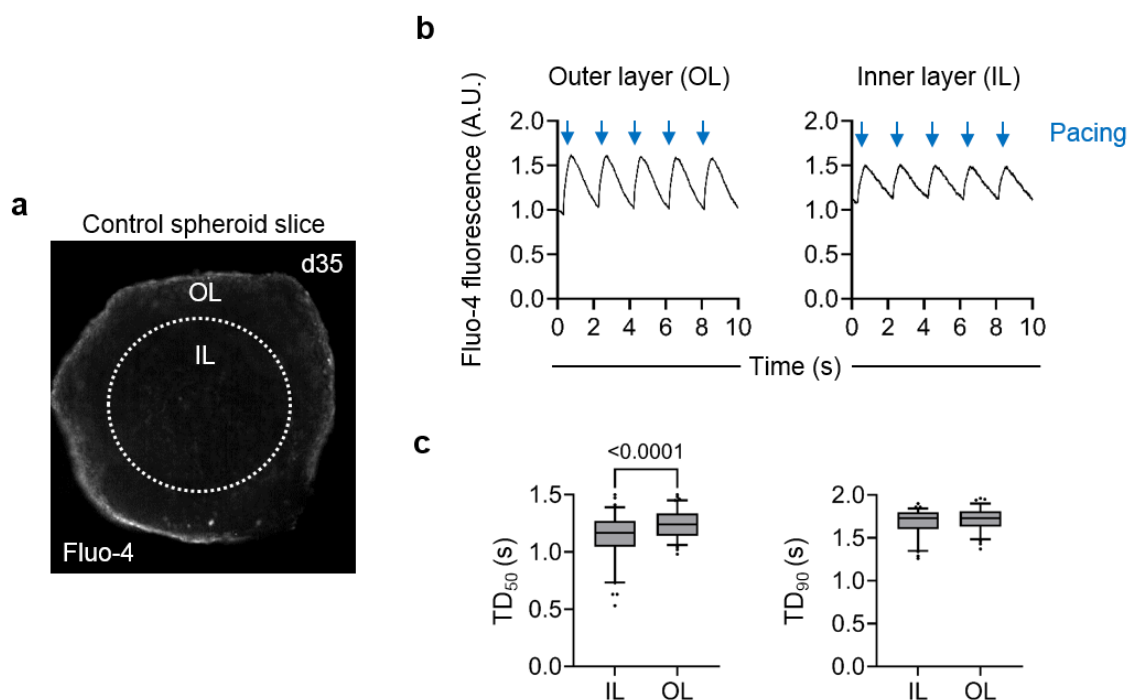


**Figure 29: Control spheroids do not show decreased calcium transient duration in the outer layer.** (a) Representative image of a control spheroid slice loaded with Fluo-4 for calcium transient imaging at day 35. The dotted line defines the outer layer (OL) and inner layer (IL) of the spheroid. (b,c) Exemplary traces of Fluo-4 fluorescence in the IL and OL under 0.5 Hz pacing conditions. (b) Corresponding quantification of  $TD_{50}$  (the duration until 50% peak decay, left),  $TD_{90}$  (the duration until 90% peak decay, right) (c) in the OL and IL.  $N = 2$  differentiations;  $n = 75$  transients per layer from 4 spheroids. P-values obtained by unpaired two-tailed  $t$ -test.

To confirm that differences in calcium transient durations could be extrapolated to action potential durations, we generated epicardioids from a genetically modified hiPSC line ubiquitously expressing a FRET-based voltage indicator knocked into the AAVS1 safe harbor locus under the CAG promoter (AAVS1-CAG-VSFP, gene editing and validation performed by Fangfang Zhang). The construct consists of a voltage-sensing transmembrane domain fused to a green fluorescent protein (GFP, specifically Clover) and a red fluorescent protein (RFP, specifically mRuby2). In the resting state, excitation of Clover results in the transfer of a fraction of the excitation energy to mRuby2 by Förster resonance energy transfer (FRET), i.e., bright green fluorescence emission is accompanied by dim red fluorescence emission. Upon membrane depolarization, a structural rearrangement of the voltage sensor triggers a reorientation of the fluorophores that increases FRET efficiency, resulting in brighter red

fluorescence and lower green fluorescence (Fig. 30a). By acquiring videos of the cells at a fluorescence microscope equipped with an image splitter separating the red and green fluorescence emissions, the change in the two signals can be recorded simultaneously and a ratio of the two can be calculated to infer the membrane potential in every image of a time-lapse series recorded at 100 frames per second (fps) (method previously described in<sup>169</sup>).

Live imaging of whole AAVS1-CAG-VSFP epicardioids at day 30 showed the expected green and red fluorescence (Fig. 30b). For simultaneous imaging of the OL and IL, 250  $\mu\text{m}$ -thick sections were prepared with a vibratome as previously. Optical action potential imaging in these slices revealed significantly shorter action potential durations in the OL, as determined by mapping the duration to 50% ( $\text{ADP}_{50}$ ) or 90% repolarization ( $\text{ADP}_{90}$ ) (Fig. 31a) and extracting corresponding values from ROIs localized in the OL or IL ( $\text{ADP}_{50}$  OL:  $0.46 \pm 0.05$  s vs IL:  $0.54 \pm 0.09$  s;  $\text{ADP}_{90}$  OL:  $0.65 \pm 0.08$  s vs IL:  $0.82 \pm 0.14$  s; both  $p < 0.0001$ ) (Fig. 31b-c).

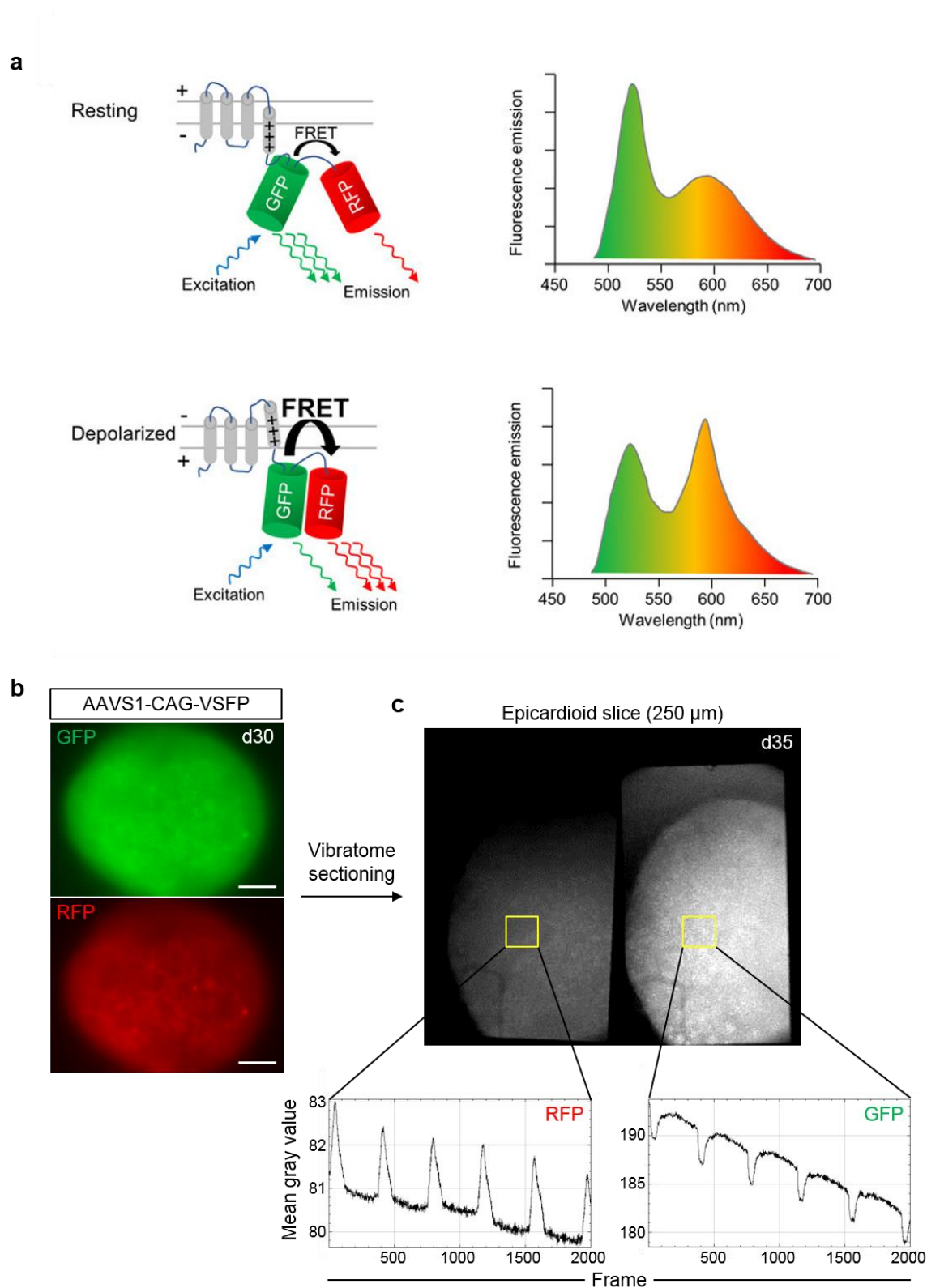


**Figure 30: Optical action potential imaging in epicardioid slices via a genetically encoded FRET-based voltage indicator. (a)** Schematic representation of the conformational states of the voltage-sensitive fluorescent protein (VSFP) and the associated changes in GFP and RFP fluorescence

intensity at rest (top) and upon depolarization of the membrane (bottom) in cardiomyocytes. Modified from Goedel et al. 2018, *J. Vis. Exp.*<sup>169</sup>. **(b)** Live imaging of a whole epicardioid differentiated from a hiPSC line edited to ubiquitously express VSFP from the AAVS1 locus (day 30). Scale bars = 200  $\mu\text{m}$ . **(c)** Exemplary traces of GFP and RFP fluorescence intensity simultaneously acquired during spontaneous beating of a 250  $\mu\text{m}$ -thick epicardioid slice obtained by vibratome sectioning (day 35).

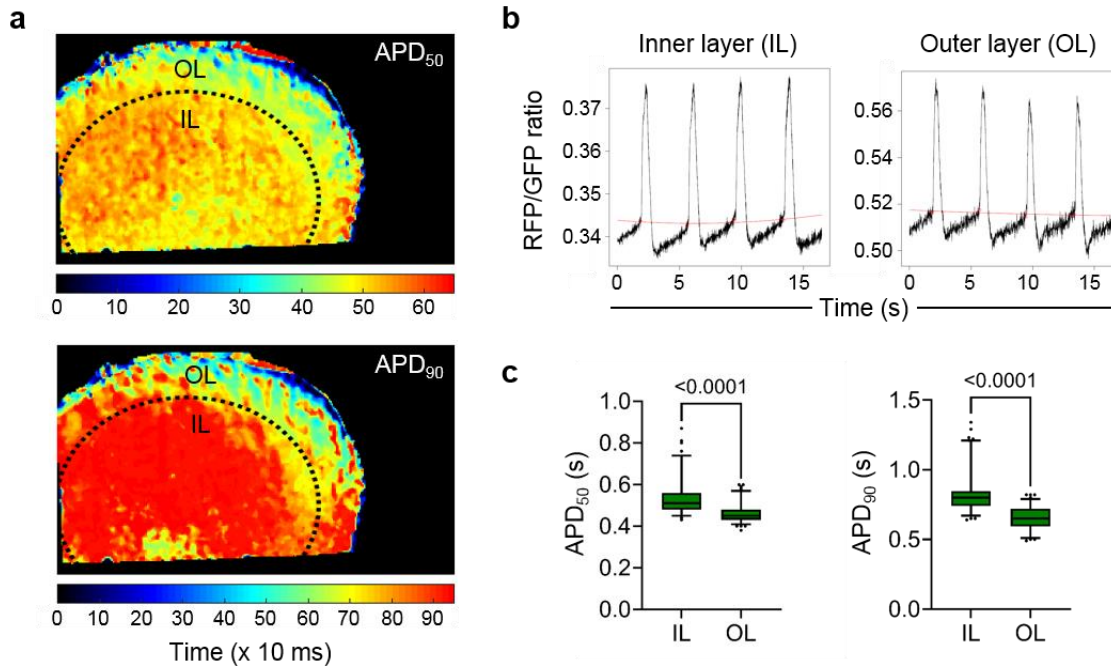


**Figure 31: Epicardioids show a decrease in action potential duration in the subepicardial outer layer. (a,b)** Representative map of  $\text{APD}_{50}$  (the duration from the beginning of the action potential (AP) until the repolarization is 50% completed, top) and  $\text{APD}_{90}$  (the duration until the repolarization is 90% completed, bottom) in an epicardioid slice at day 35 of differentiation. The dotted line defines the outer layer (OL) and inner layer (IL) of the epicardioid. Maps generated by Dr. Qinghai Tian. (a) Corresponding exemplary traces of the ratio of RFP and GFP fluorescence intensity in the IL and OL (b). **(c)** Quantification of  $\text{APD}_{50}$  (left) and  $\text{APD}_{90}$  (right) in the OL and IL of spontaneously beating epicardioids between days 35 and 40 of differentiation.  $N = 2$  differentiations;  $n = 100$  APs from 4 epicardioids, 3-4 ROIs per layer per epicardioid. P-values obtained by unpaired two-tailed  $t$ -test.

### 3.2.3 The epicardial layer is a source of mesenchymal cells

During embryonic development, the epicardium is the source of several non-myocytic lineages after a subset of epicardial cells undergoes EMT and gives rise to epicardial-derived cells (EPDCs) that will invade the myocardium and mainly differentiate into fibroblasts and smooth muscle cells. This process can take place *in vitro*, as hiPSC-derived epicardial cells differentiated with the protocol presented in Figure 21 give rise to smooth muscle cells and fibroblasts upon treatment with TGF- $\beta$ 1 and FGF2, respectively (Fig. 32a-d).

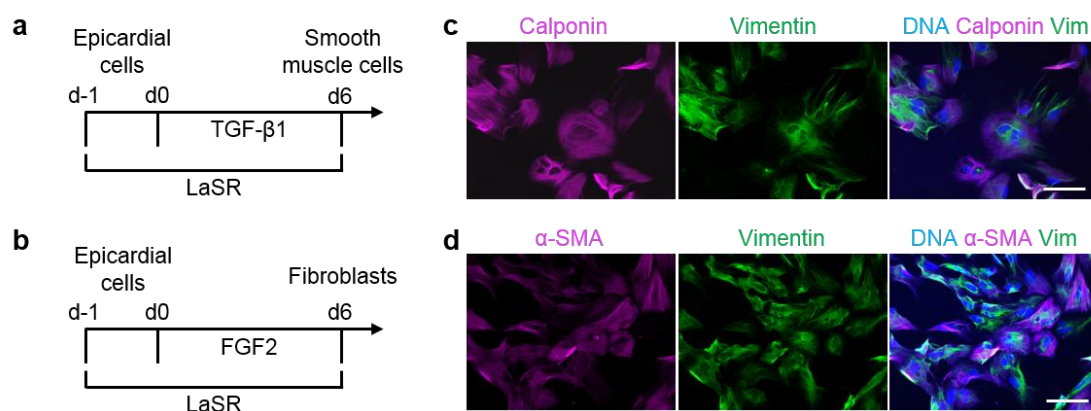


**Figure 32: hiPSC-derived epicardial cells can differentiate into smooth muscle cells and fibroblasts.** (a,b) Graphical representation of the protocols used to differentiate hiPSC-derived epicardial cells into smooth muscle cells (a) and fibroblasts (b) as established by Bao and colleagues<sup>85</sup>. (c,d) Representative images of smooth muscle cells (c) and fibroblasts (d) differentiated with the protocols described in (a-c) and immunostained for calponin, vimentin (Vim) or alpha smooth muscle actin ( $\alpha$ -SMA). Scale bars = 100  $\mu$ m.

Although both epicardioids and control spheroids contained cTnT<sup>-</sup> vimentin<sup>+</sup> mesenchymal cells interspersed between cardiomyocytes at day 15 (Fig. 33a), epicardioids showed significantly higher expression of the cardiac fibroblast marker *DDR2* and the smooth muscle cell marker *MYH11*, suggesting the emergence of EPDCs dependent on the presence of the epicardial layer (Fig. 33b). In some sections of epicardioids, vimentin<sup>+</sup> mesenchymal cells appeared to migrate inward away from the epicardial layer, resembling the migration of EPDCs into the myocardium after epicardial EMT (Fig. 33a).

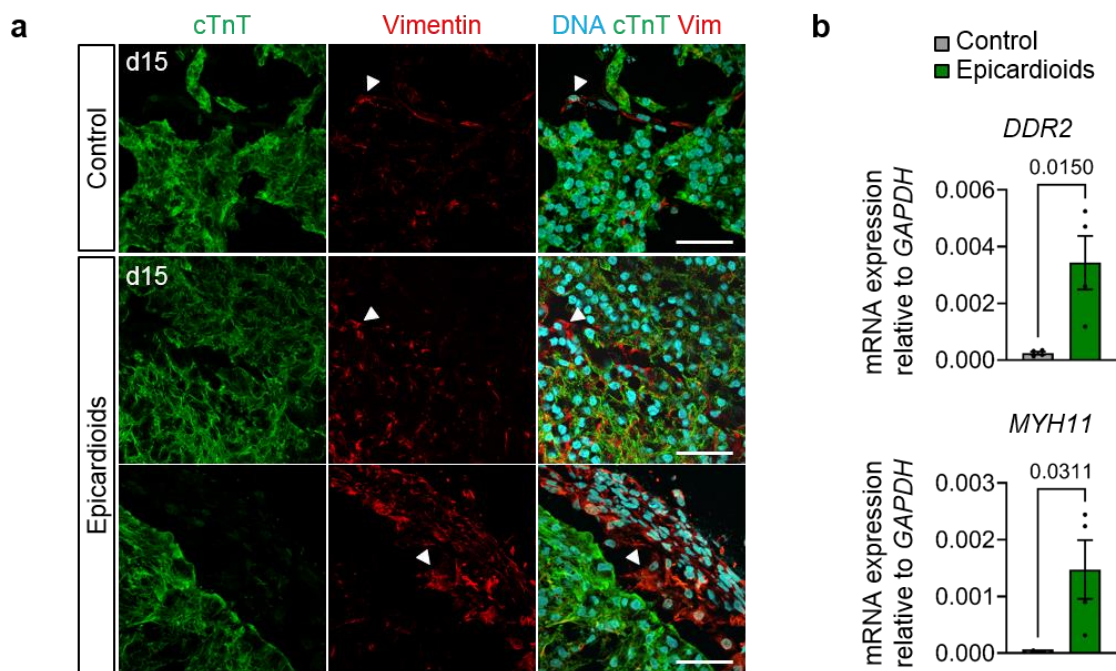


**Figure 33: The epicardial layer is a source of fibroblasts and smooth muscle cells. (a)** Representative images of cTnT and vimentin (Vim) immunostaining of control spheroids and epicardioids at day 15 of differentiation. Scale bars top = 100  $\mu$ m, bottom = 50  $\mu$ m. Arrowheads show examples of cTnT<sup>-</sup> vimentin<sup>+</sup> mesenchymal cells. **(b)** mRNA expression levels of *DDR2* and *MYH11* relative to *GAPDH* at day 15 of epicardioid or control spheroid differentiation, as determined by qRT-PCR. Bars show the mean  $\pm$  SEM and all data points; N = 3 differentiations; n = 4/group. P-values determined by unpaired two-tailed *t*-test.

Moreover, we found that the epicardial layer diminished over time, with only  $14.8 \pm 25.6\%$  epicardioids showing a complete epicardial layer by day 30,  $78.5 \pm 22.2\%$  a partial layer and  $10.8 \pm 10.1\%$  no layer at all (Fig. 34a-b). This was accompanied by an increase in fibroblast-like cells, detectable by immunofluorescence and by the expression level of *DDR2* compared to day 15 (Fig. 34a,c). The expression of the smooth muscle marker *MYH11* also slightly increased (Fig. 34c). These results could indicate that the epicardial layer continuously produces EPDCs and is thereby depleted over time. However, Ki67 staining showed that the epicardial layer was still proliferative on day 30, suggesting concomitant maintenance of the epicardial layer by a subset of dividing cells (Fig. 34d).

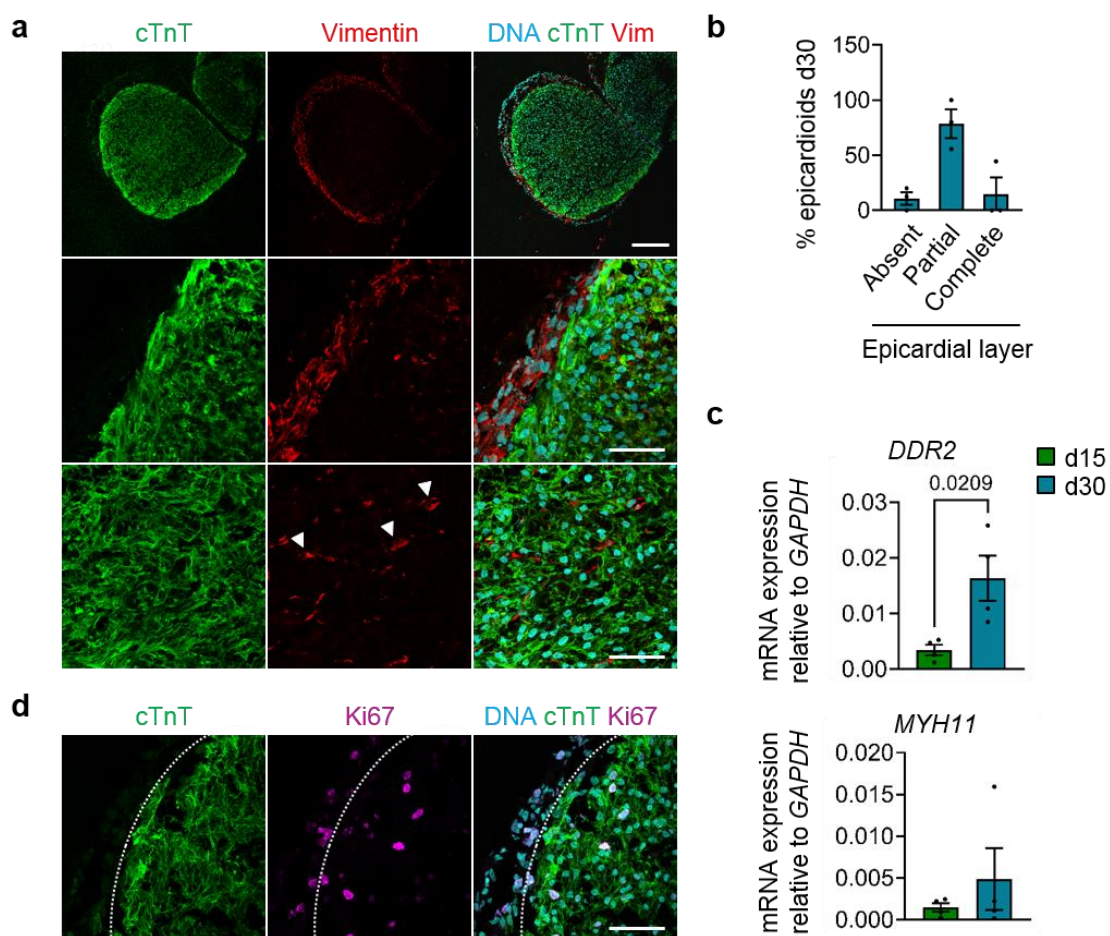


**Figure 34: The epicardial layer is maintained but partially depleted over time.** (a) Representative images of cTnT and vimentin (Vim) immunostaining of epicardioids at day 30 of differentiation. Scale bars top = 100  $\mu\text{m}$ , bottom = 50  $\mu\text{m}$ . Arrowheads show examples of cTnT<sup>-</sup>vimentin<sup>+</sup> mesenchymal cells. (b) Percentage of epicardioids with an absent, partial or complete epicardial layer at day 30 of differentiation. Bars indicate the mean  $\pm$  SEM and all data points; N = 3 differentiations, n = 22 epicardioids. (c) mRNA expression levels of *DDR2* and *MYH11* relative to *GAPDH* at days 15 and 30 of epicardioid differentiation, as determined by qRT-PCR. Bars show the mean  $\pm$  SEM and all data points; N = 3 differentiations; n = 4/group. P-values determined by unpaired two-tailed *t*-test. (d) Representative images of cTnT and Ki67 immunostaining of epicardioids at day 30 of differentiation. Scale bar = 50  $\mu\text{m}$ . The dotted line indicates the separation between the myocardial and epicardial layers.

It is still debated to which extent EPDCs can differentiate into endothelial cells, with some studies showing limited contribution to the coronary vasculature<sup>51</sup>. We found that supplementing the maintenance medium with the angiogenic growth factor VEGF was

necessary to detect an endothelial component in epicardioids at day 15. This was not the case in control spheroids, which showed significantly higher expression of the endothelial markers *CD31* and *CDH5* even without addition of VEGF, underlining differences in CPC lineage specification caused by retinoic acid modulation (Fig. 35a-b). In epicardioids, although some *CD31*<sup>+</sup> endothelial cells were found within the inner myocardial mass, the majority of *CD31*<sup>+</sup> cells were found in close proximity to or within the epicardial layer, suggesting an epicardial origin (Fig. 35a).

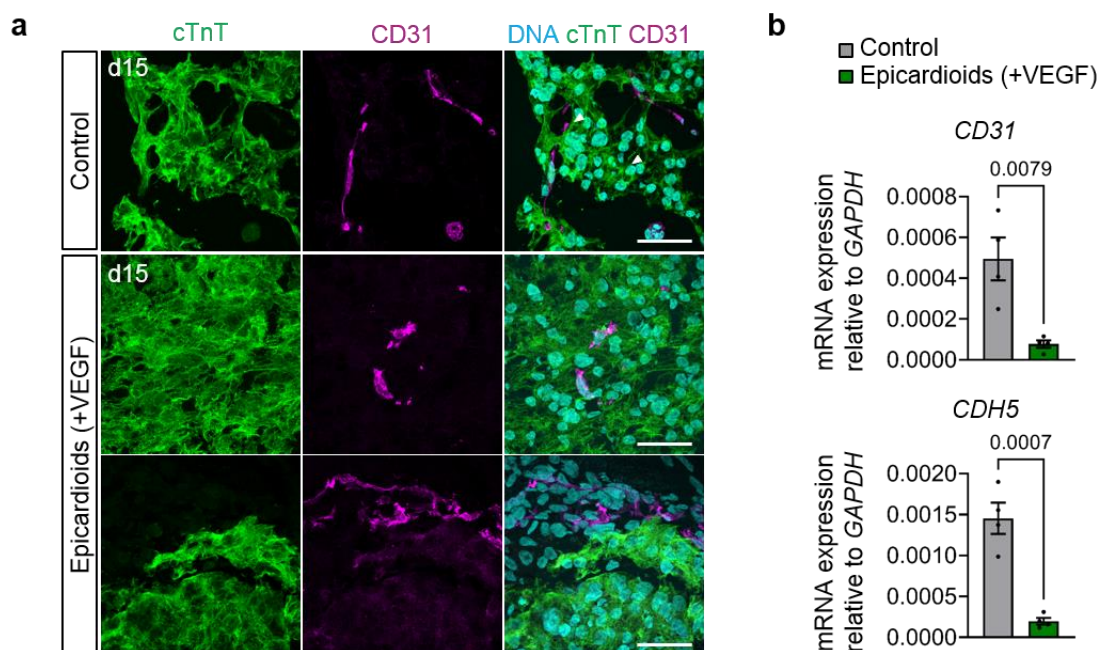


**Figure 35: Endothelial lineage specification is weak in epicardioids compared to control spheroids.** (a) Representative images of cTnT and CD31 immunostaining of control spheroids and VEGF-treated epicardioids at day 15 of differentiation. Scale bars = 50  $\mu$ m. (b) mRNA expression levels of *CD31* and *CDH5* relative to *GAPDH* at day 15 of control spheroid or VEGF-treated epicardioid differentiation, as determined by qRT-PCR. Bars show the mean  $\pm$  SEM and all data points; N = 3 differentiations; n = 4/group. P-values determined by unpaired two-tailed *t*-test.

Of note, Bao and colleagues demonstrated that hiPSC-derived epicardial cells could be coaxed into endothelial cells by VEGF treatment<sup>88</sup>, which we could also reproduce, supporting this possibility (Fig. 36a,b).

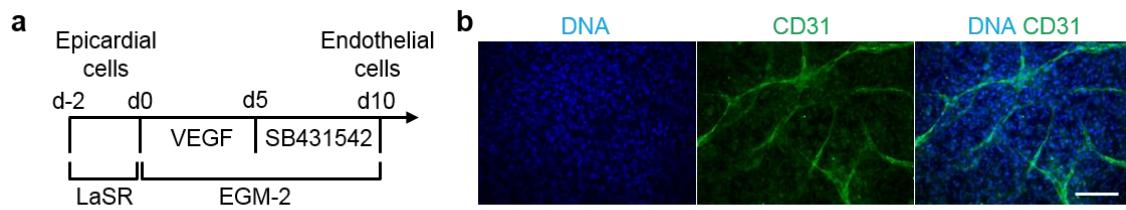


**Figure 36: hiPSC-derived epicardial cells can be differentiated into endothelial cells. (a)** Graphical representation of the protocol used to differentiate hiPSC-derived epicardial cells into endothelial cells, as established by Bao and colleagues<sup>88</sup>, with some modifications. **(b)** Representative images of endothelial cells differentiated with the protocol described in (a) and immunostained for CD31. Scale bar = 100  $\mu\text{m}$ .

Overall, we could demonstrate that the epicardial layer observed in epicardioids is not only an additional cell population compared to control spheroids but that it is associated with key morphological, functional, and cellular features associated with the epicardium in vivo.

### 3.3 Single-cell time course analysis reveals molecular processes of epicardioid development and maturation

#### 3.3.1 Time course scRNA-Seq analysis of epicardioids

For in-depth characterization of the cell populations arising during epicardioid development, we next performed a single-cell RNA-sequencing (scRNA-Seq) time course. Based on insights from the immunofluorescence and transcriptomic analyses presented above, we chose seven time points for analysis: days 2, 3, 4, 5, 7, 10, and 15 (Fig. 37a). We hypothesized that these time points would allow us to capture the specification of proepicardial progenitors and epicardial cells as well as the differentiation of EPDCs. For each sample, 6-13 epicardioids were pooled for single cell dissociation with papain. Libraries were then prepared via a GEM-based system (10x Genomics, see §2.2.3) wherein single cells are encapsulated together with reverse transcription reagents to synthesize cDNA barcoded according to its individual cell of origin (Fig. 37b).

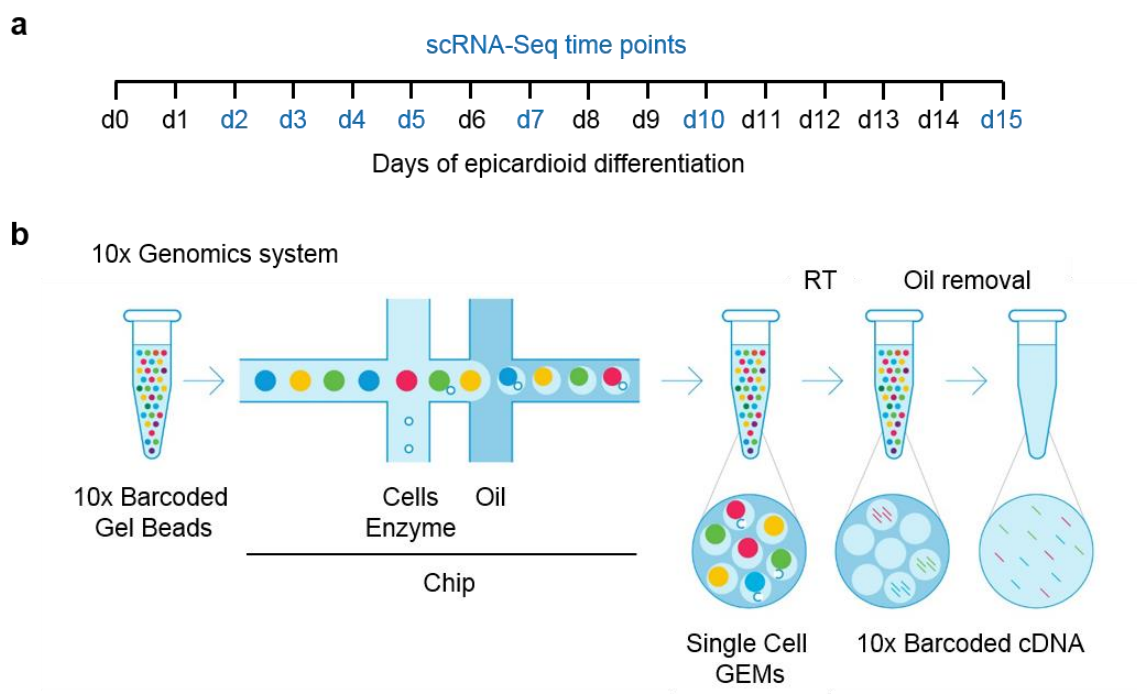


**Figure 37: Time course scRNA-Seq analysis of epicardioid formation. (a)** Schematic representation of the time points of differentiation chosen to dissect key steps of epicardioid

---

development by scRNA-Seq analysis. **(b)** Schematic representation of the 10x Genomics workflow used to prepare cells for sequencing. GEMs are generated by loading single cells on a chip in which they are encapsulated with a barcoded gel bead with the help of partitioning oil. Reverse transcription within the GEMs results in cDNA barcoded according to its individual cell of origin. Adapted from [www.10xgenomics.com](http://www.10xgenomics.com).

After sample processing and quality control, the dataset consisted of a total of 35,499 cells, with an average of  $5,071 \pm 546$  cells per time point. To get an overview of the cell populations across all time points, data from the seven samples were merged and analyzed by UMAP (Uniform Manifold Approximation and Projection), a nonlinear dimensionality reduction algorithm yielding more meaningful separation of cell populations than the commonly used method of *t*-distributed stochastic neighborhood embedding (t-SNE)<sup>170</sup>. This resulted in the identification of 31 clusters, ranked 0 to 30 according to size (Fig. 38a). Visualization of the clusters separated by sample revealed significant shifts from one time point to the next, with the exception of days 4 and 5, which had a large overlap between clusters hinting to smaller developmental differences between these two samples compared to the others (Fig. 38b).

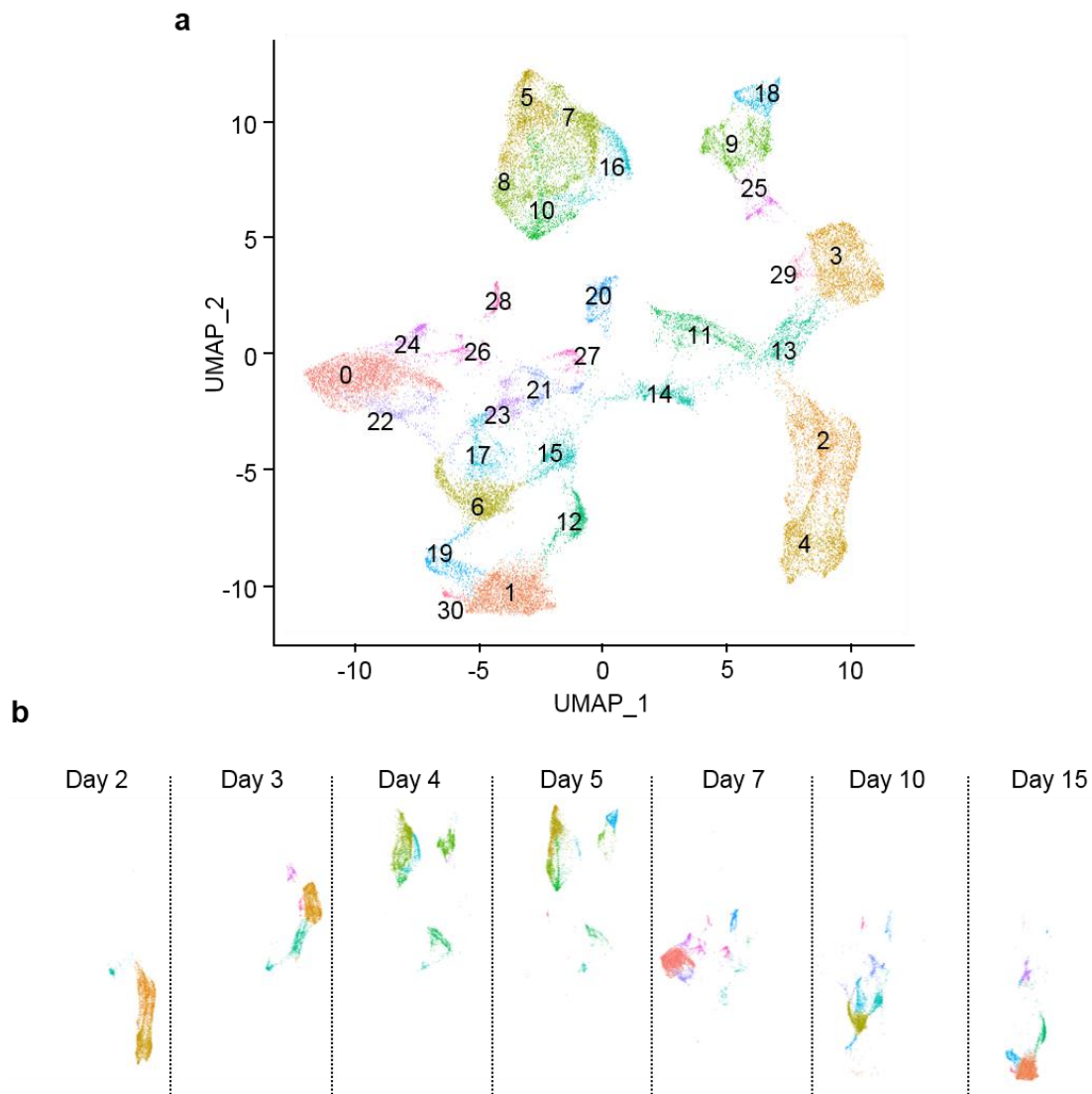


**Figure 38: UMAP visualization of cell clusters in the complete scRNA-Seq dataset of epicardioid formation. (a,b)** Annotated UMAP plot showing the distribution of the 31 clusters identified in the scRNA-Seq data of epicardioids at days 2, 3, 4, 5, 7, 10, and 15 of differentiation (a) and separation of the clusters by day (b).

To define cluster identities, we took advantage of several publicly available scRNA-Seq datasets of human development: from Asp et al., a spatiotemporal atlas of the human heart at 4.5-5, 6.5-7 and 9 post conception weeks<sup>171</sup>, from Cui et al., a dataset of human hearts ranging from 5 to 25 post conception weeks<sup>172</sup>, and from Tyser et al., a spatially resolved single cell dataset of a human gastrulating embryo at approximately 16 to 19 days post fertilization<sup>161</sup>. Having a specific interest in epicardial specification, we also used two datasets of the murine developing

---

heart between approximately E7.25 and E8.25, which supported the authors' characterization of multipotent progenitors of myocardium and epicardium (referred to here as juxta-cardiac field, JCF)<sup>40,41</sup>. With the exception of Cui et al., all authors provided valuable online tools allowing the visualization of any gene's expression level and distribution among identified clusters. To avoid relying on markers that may be typical but not specific of a given cell type, we used these datasets to identify genes that were as specific as possible to each cell type of interest as well as consistent between two or more studies. This allowed the classification of clusters according to the following cell identities: early mesoderm, cardiac progenitor cells (CPCs), endoderm, endothelial cells, (pro)epicardial cells and their derivatives, early cardiomyocytes, and late cardiomyocytes. The process of cluster definition and main conclusions derived from transcriptional dynamics are detailed in the following sections.

### 3.3.2. First heart field specification is predominant in epicardioids

As previously determined by qRT-PCR and immunofluorescence (see Fig. 18), early epicardioids recapitulated molecular processes of cardiac mesoderm specification, with the majority of cells expressing *MESP1* on day 2 (clusters 2 and 4, Fig. 39a). scRNA-Seq analysis additionally revealed the presence of *SOX17*<sup>+</sup> *FOXA2*<sup>+</sup> endodermal progenitors on days 4 and 5 (clusters 9, 18 and 25), which likely gave rise to cells positive for hepatic markers such as *AFP* and *ALDH1A1*, detected by day 7 (cluster 20, Fig. 39b). However, this population dwindled to 0.5% of total cells by day 15, suggesting that the culture conditions do not support the maintenance of endodermal derivatives. The absence of ectodermal markers such as *PAX6* and *SOX1* indicated that this germ layer was not induced at all (data not shown).

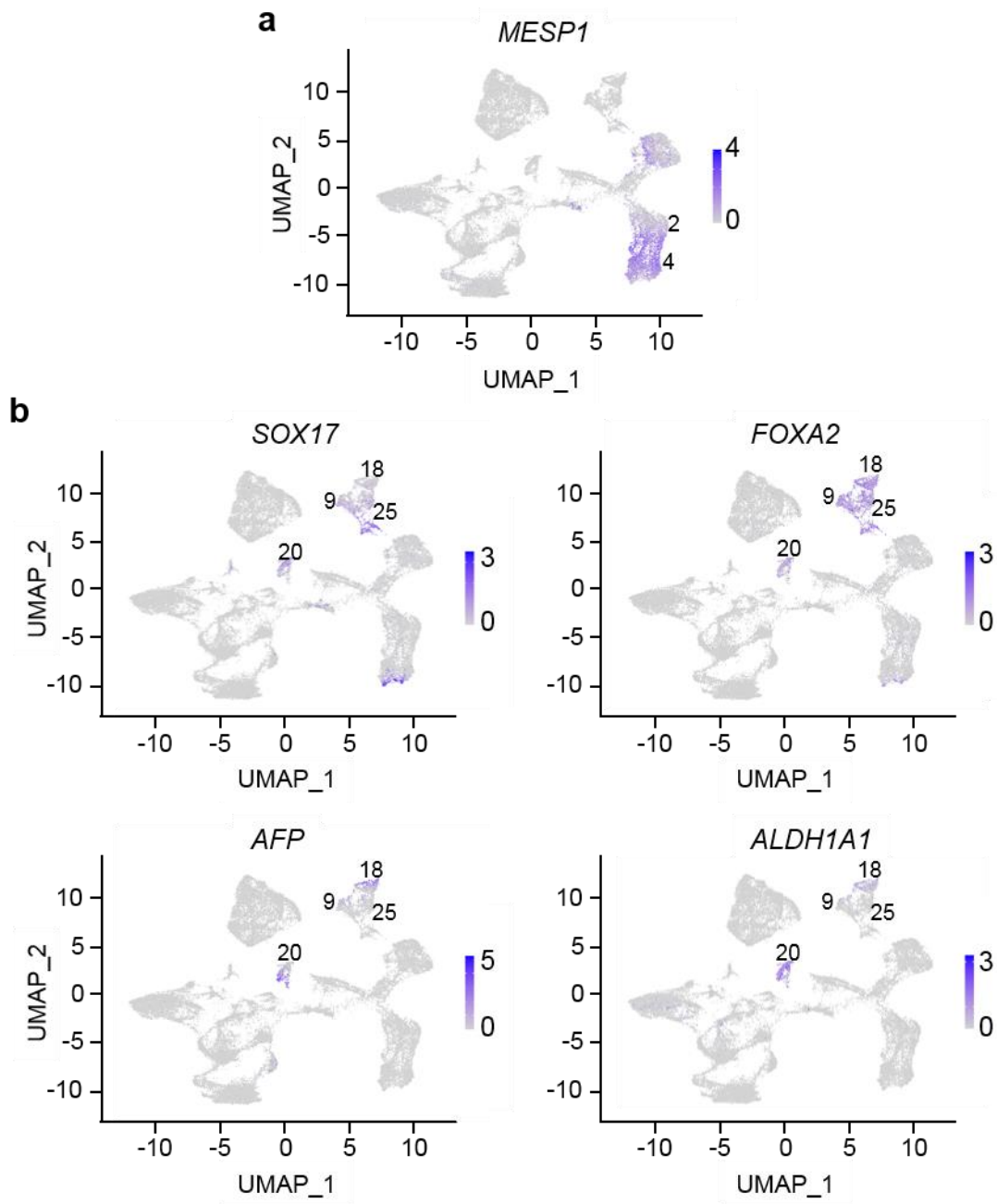


**Figure 39: Expression of markers of mesoderm and endoderm during epicardioid formation.** (a-d) UMAP feature plots of markers of mesoderm (*MESP1*) (a) and endoderm (*SOX17*, *FOXA2*, *AFP*, *ALDH1A1*) (b) in epicardioids across all time points. Heatmaps indicate the respective level of expression of each gene. Relevant clusters mentioned in the text are annotated.

We next evaluated clusters 5, 7, 8, 10, and 16, which we identified as cardiac progenitor cells based on widespread expression of *ISL1* from day 4 followed by initiation of *NKX2.5*

expression on day 5 (Fig. 40a). In addition to the high expression of the FHF marker *TBX5* in these clusters, the very low number of cells positive for SHF markers such as *TBX1*, *FGF10*, and *FGF8* indicated that CPCs in epicardioids have a predominantly FHF identity (Fig. 40b).

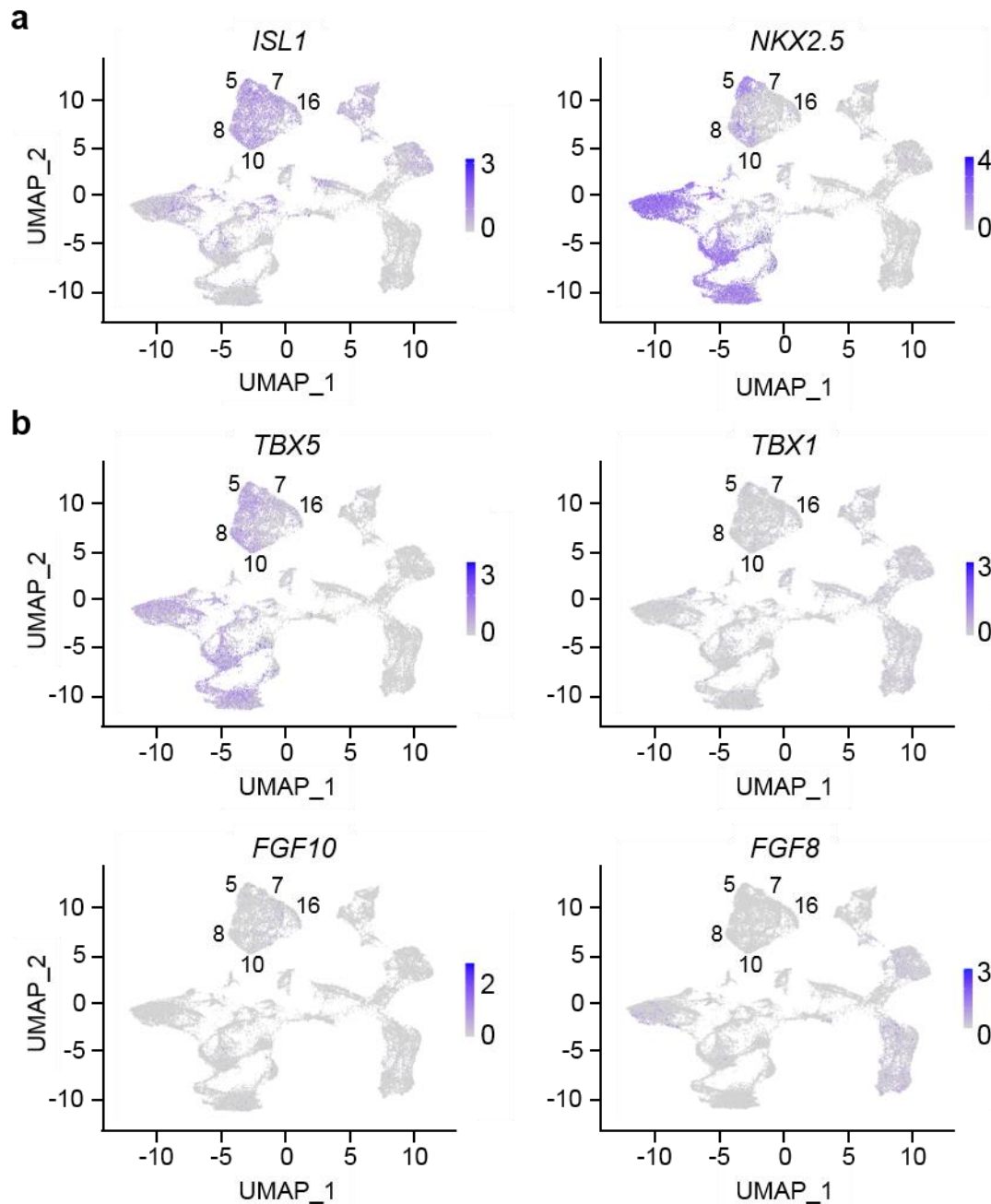


**Figure 40: Expression of markers of first and second heart field in CPC clusters. (a,b)** UMAP feature plots of markers of CPCs (*ISL1*, *NKX2.5*) (a) and specifically FHF (*TBX5*) and SHF (*TBX1*,

*FGF10*, *FGF8*) (b) in epicardioids across all time points. Heatmaps indicate the respective level of expression of each gene. Relevant clusters mentioned in the text are annotated.

Weak SHF specification may explain the paucity of endothelial cells within epicardioids, previously shown in Figure 35. We identified only a small cluster of cells matching an early endothelial cell signature (co-expression of *IGFBP4*, *RAMP2*, *KDR*, *PLVAP*, *HAPLN1*, and *CDH5*; cluster 28), which represented between 1.3 and 2.8% of cells between days 5 and 10 but was reduced to 0.2% of cells by day 15 (Fig. 41a). The expression of endocardial markers such as *NPR3* and *HEY2* in some cells of this cluster suggested that an endocardial compartment may be transiently formed during epicardioid development but not maintained (Fig. 41b). Although proximity to the epicardial layer had suggested an epicardial origin (see Fig. 35), the early emergence of these cells at day 5 did not support this.

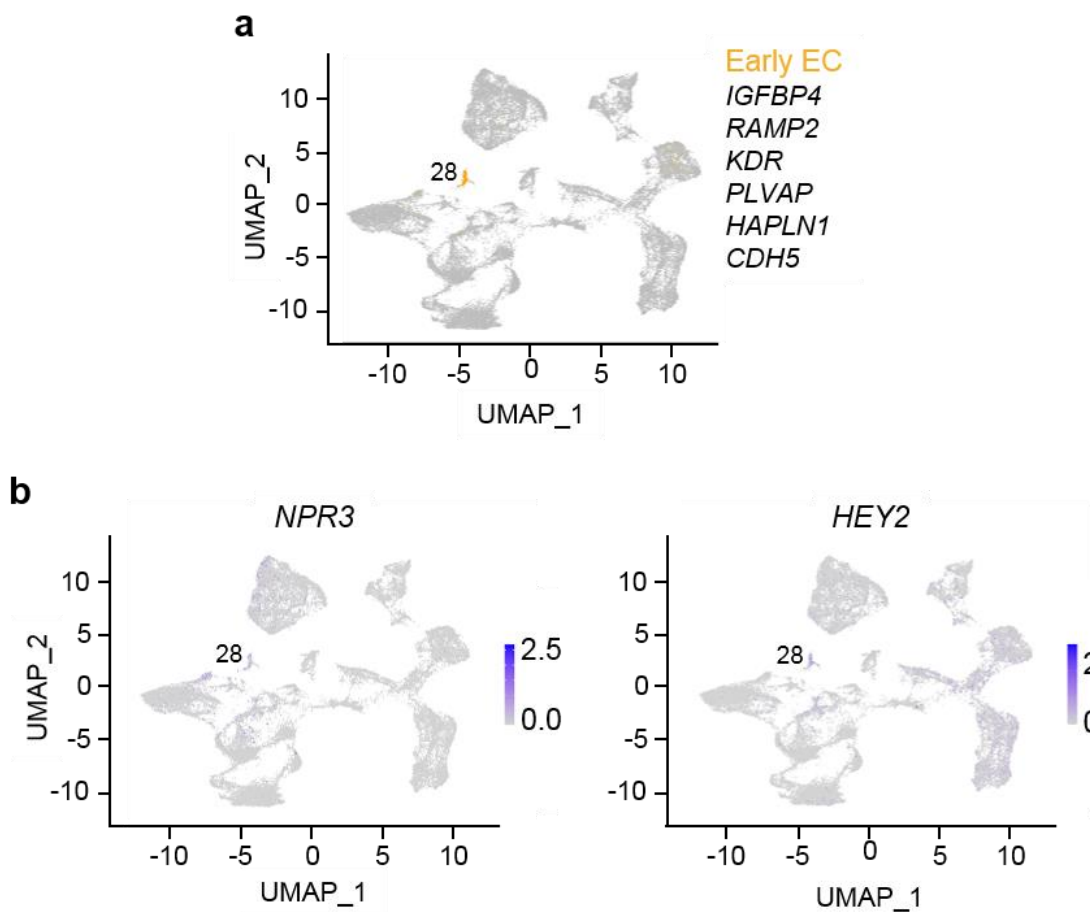


**Figure 41: Expression of endothelial lineage markers during epicardioid formation.** (a) UMAP feature plot showing cells co-expressing markers of early endothelial cells (*IGFBP4*, *RAMP2*, *KDR*, *PLVAP*, *HAPLN1*, *CDH5*) in epicardioids across all time points. (b) UMAP feature plots of the endocardial markers *NPR3* and *HEY2* in epicardioids across all time points. Heatmaps indicate the respective level of expression of each gene. The relevant cluster mentioned in the text is annotated.

### 3.3.3. Transcriptional signatures reflect ventricular patterning and maturation

Differentiated cardiomyocytes could be identified by the expression of sarcomeric markers such as *TNNT2* by day 7 and represented 88.9% of cells by day 15 (across all samples: clusters 24, 26, 0, 22, 17, 6, 15, 19, 30, 1, and 12) (Fig. 42a). Consistent with FHF specification, the predominantly ventricular identity of cardiomyocytes was apparent from day 7 by the expression of the early ventricular marker *MYL3* (Fig. 35b). By day 15, most cardiomyocytes matched an in vivo ventricular signature (*MYH7*, *VCAN*, *MYL2*, *MASP1*, *S100A4*) (Fig. 42c). By contrast, there was no specific match to an atrial signature (*MYH6*, *PAM*, *VSNL1*, *GPX3*, *CPNE5*) (data not shown). qRT-PCR analysis additionally showed that the mature ventricular marker *MYL2* was upregulated while *MYL3* was downregulated at day 30 compared to day 15, indicating maturation of cardiomyocytes over time (Fig. 42d).

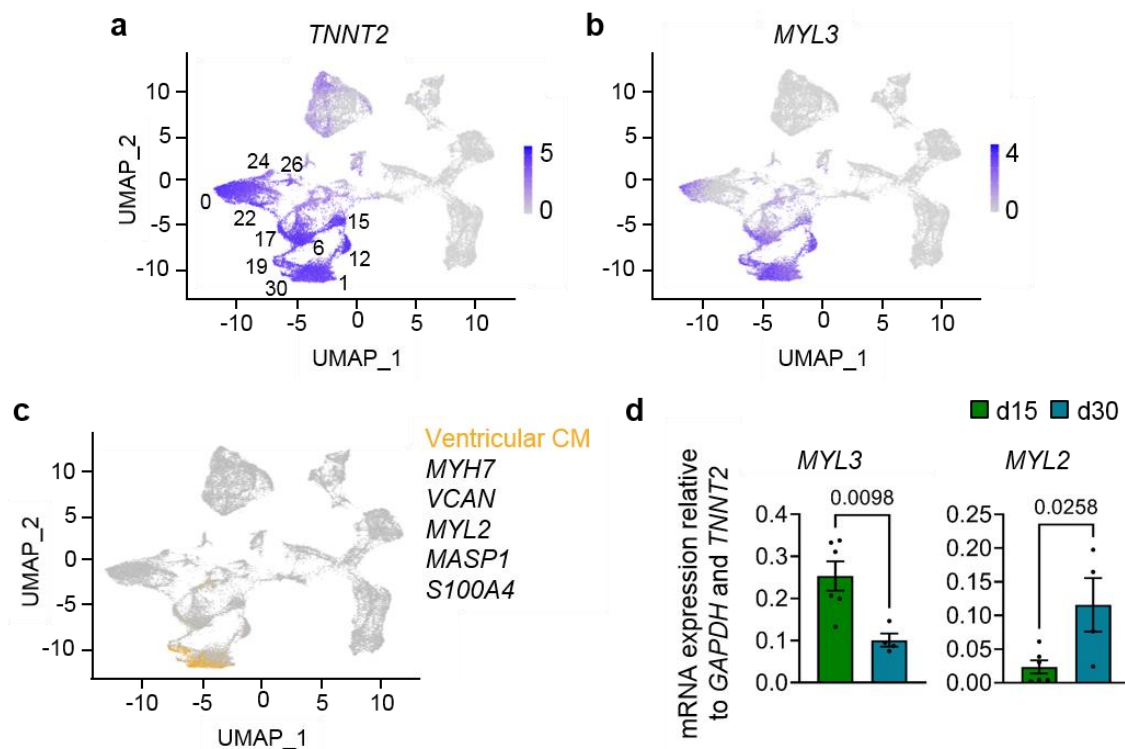


**Figure 42: Expression of ventricular markers during epicardioid formation and long-term culture.** (a,b) UMAP feature plots of *TNNT2* (a) and *MYL3* (b) in epicardioids across all time points. Heatmaps indicate the respective level of expression of each gene. Relevant clusters mentioned in the text are annotated. (b) UMAP feature plot showing cells co-expressing markers of human ventricular cardiomyocytes (*MYH7*, *VCAN*, *MYL2*, *MASP1*, *S100A4*) in epicardioids across all time points. (c) mRNA expression levels of *MYL3* and *MYL2* relative to *GAPDH* and *TNNT2* at days 15 and 30 of epicardioid differentiation, as determined by qRT-PCR. Bars show the mean  $\pm$  SEM and all data points; d15: n = 7 from N = 3 differentiations, d30: n = 4 from N = 2 differentiations. P-values determined by unpaired two-tailed *t*-test.

Importantly, transcriptional features of the cardiomyocytes at day 15 allowed us to distinguish between a ‘compact’ cluster (30, representing 2.8% of CMs), a ‘trabecular’ cluster (12, representing 21.7% of CMs) and two ‘intermediate’ clusters (1 and 19, representing 64.1% and 11.4% of CMs, respectively). This was illustrated by the gradient of expression of trabecular markers such as *NPPB* and *FHL2*, highest in cluster 12 (Fig. 43a), and compact markers such as *RAMP1* and *FZD1*, highest in cluster 30 (Fig. 43b)<sup>172,173</sup>. Cluster 19, which already emerged at day 10, was composed of cardiomyocytes that expressed mitotic markers such as *TOP2A* (Fig. 43c). Considering the concentration of dividing cells in the compact layer (Fig. 27) and

transcriptional similarities with cluster 30, this cluster likely included a large proportion of cells undergoing division to form the compact layer (Fig. 43a-c). We next assessed the maturation levels of these cardiomyocytes. During embryonic development, the maturation of cardiomyocytes is associated with the stoichiometric replacement of the fetal isoform of troponin I (encoded by *TNNI1*) with the adult isoform (encoded by *TNNI3*), making the ratio of *TNNI3/TNNI1* a quantifiable indicator of maturation<sup>174</sup>. In epicardioids, cardiomyocytes with a trabecular profile had the highest *TNNI3/TNNI1* ratio (1.25), indicating the highest maturation, while compact cardiomyocytes had the lowest (0.44) (Fig. 43d). This is in line with *in vivo* studies reporting faster maturation in trabecular cardiomyocytes<sup>175</sup>.

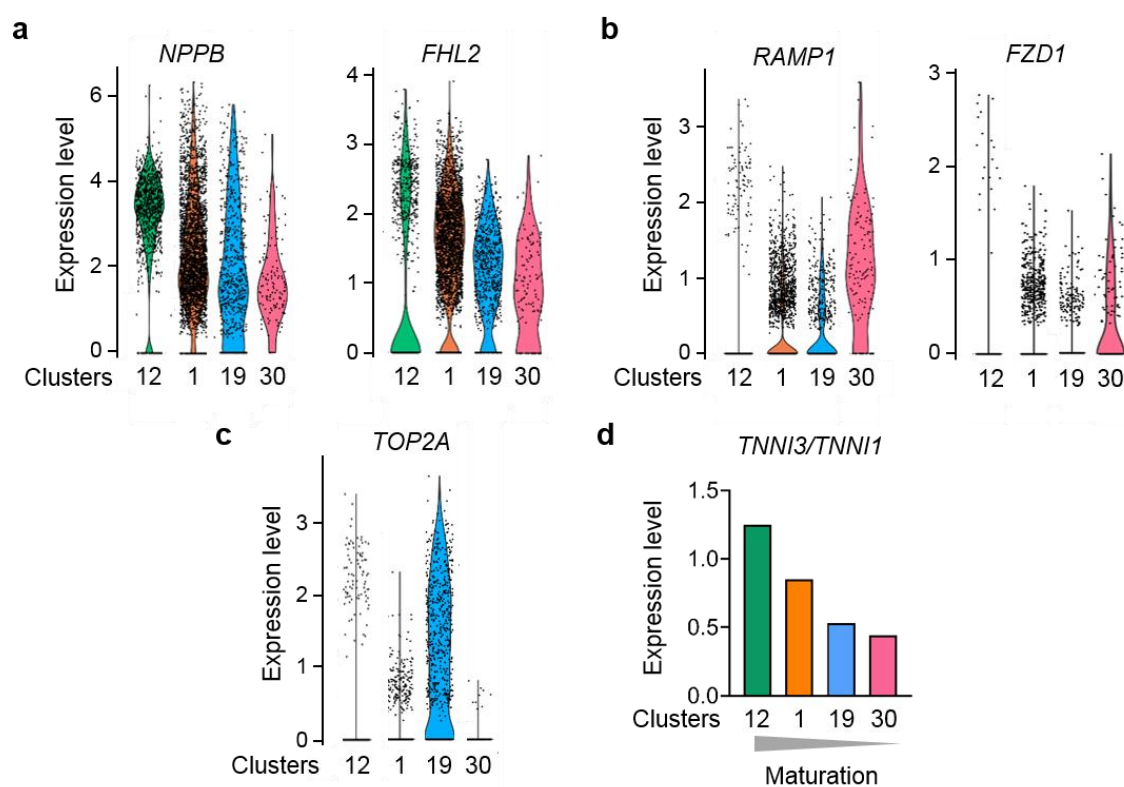


**Figure 43: Expression of compact and trabecular markers in cardiomyocyte clusters at day 15 of epicardioid differentiation. (a,c)** Violin plots showing the expression levels of markers of trabecular (*NPPB*, *FHL2*) (a), compact (*RAMP1*, *FZD1*) (b) and proliferative myocardium (*TOP2A*) (c) in cardiomyocyte clusters present in epicardioids at day 15. **(d)** Bar chart showing the ratio of expression of *TNNI3* and *TNNI1* in cardiomyocyte clusters present in epicardioids at day 15.

### 3.3.4 Epicardioids uncover human (pro)epicardial fates

To investigate the epicardial lineage in epicardioids, epicardial and epicardial-derived cell populations were first defined using markers identified in the human datasets cited above. This revealed that cells matching for signatures of the epicardium (*SULF1*, *TM4SF1*, *CCDC80*, *S100A10*), EPDCs (*RAMP1*, *ITGA8*), and epicardial-derived fibroblasts and smooth muscle cells (*PTN*, *LRRC17*, *COL1A2*, *SERPINE2*, *MFAP4*) were all found in cluster 23, present at day 15 (Fig. 44a-c). Their localization in a common cluster is consistent with the high transcriptional similarity between these populations, which is apparent in in vivo datasets and is likely to be exacerbated in iPSC-derived cells.

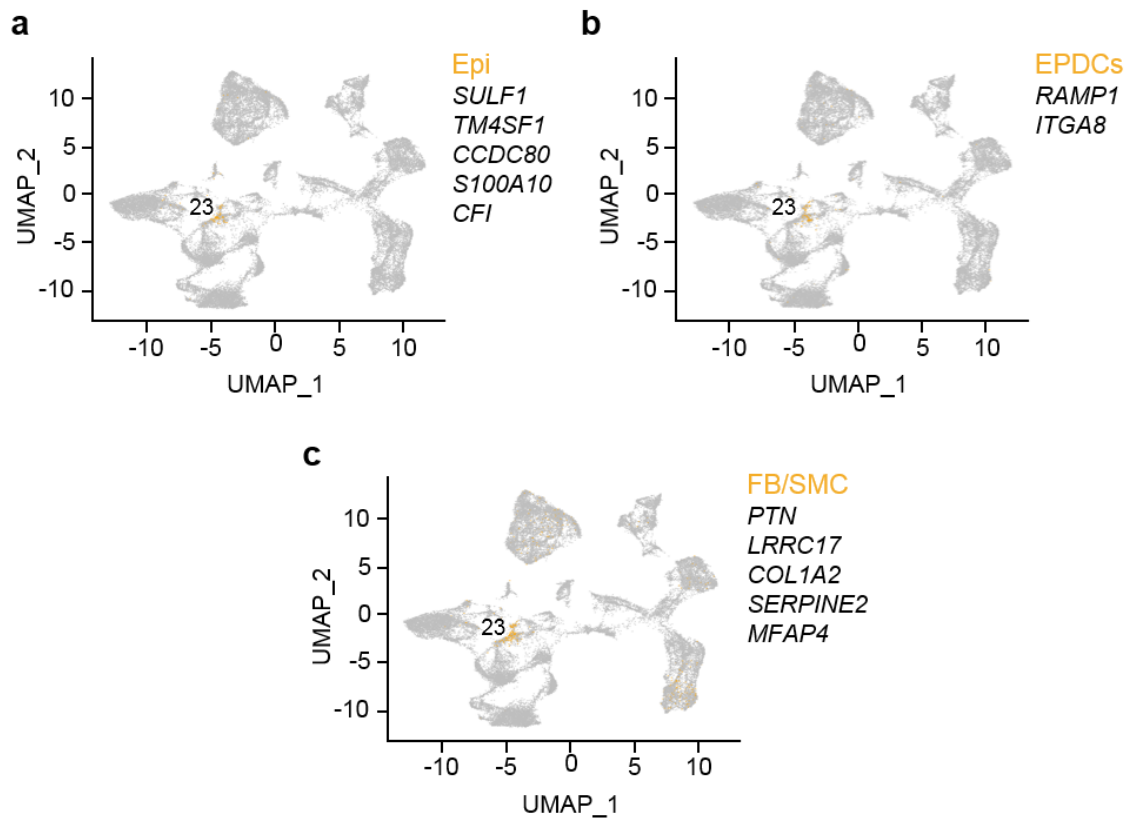


**Figure 44: Expression of epicardial lineage markers during epicardioid formation. (a-c)** UMAP feature plot showing cells co-expressing markers of the human epicardium (Epi; *SULF1*, *TM4SF1*, *CCDC80*, *S100A10*, *CFI*) (a), epicardial-derived cells (EPDCs; *RAMP1*, *ITGA8*) (b) and epicardium-derived fibroblasts and smooth muscle cells (FB/SMC; *PTN*, *LRRC17*, *COL1A2*, *SERPINE2*, *MFAP4*) (c) in epicardioids across all time points. The relevant cluster mentioned in the text is annotated.

Among the canonical markers of epicardium, *TCF21* and *SEMA3D* showed significant expression in cluster 23, while only few cells expressed *TBX18* and *WT1*, which were lowly expressed across all clusters (Fig. 45).

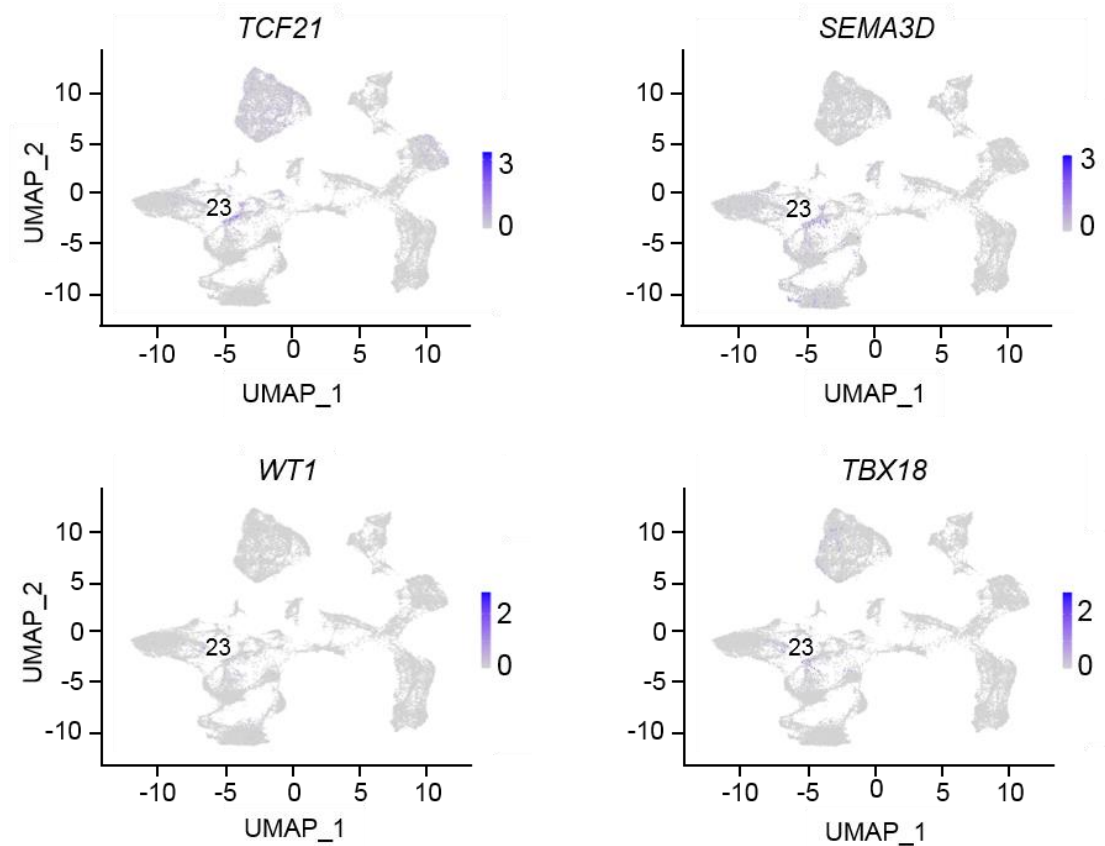


**Figure 45: Expression of canonical epicardial markers during epicardioid formation.** UMAP feature plots of *TCF21*, *SEMA3D*, *WT1*, and *TBX18* in epicardioids across all time points. Heatmaps indicate the respective level of expression of each gene. The relevant cluster mentioned in the text is annotated.

No transcriptomic data are available for human proepicardial progenitors, as existing datasets don't include developmental stages earlier than 4.5 weeks post-conception, at which point the myocardium is already partially covered by epicardial cells<sup>160</sup>. We therefore assessed the presence of juxta-cardiac field cells (JCF) identified in early murine embryos (at ~E7.75-E8.25) as multipotent progenitors of epicardium and myocardium<sup>40,41</sup>.

Co-expression analysis of markers of the JCF (*HAND1*, *MAB21L2*, *HOXB6*, *HOXB5*, *BNC2*) identified two matching clusters: cluster 27, present on day 7, and cluster 21, present on day 10 (Fig. 46a). Their close proximity to the epicardial cluster 23 supported the developmental relationship between these cells. As *HOXB6* expression was exclusive to the JCF-like clusters, its very low expression in control spheroids compared to epicardioids may explain the lack of epicardial layer formation in these structures (Fig. 46b, Fig. 26). These clusters also expressed genes identified in both the JCF and the murine proepicardial organ, such as *CCBE1* and *SPARC*<sup>40,41,176,177</sup> (Fig. 46c). Consistent with putative proepicardial progenitors identified by immunostaining, these cells were positive for *ISL1* and had very low *NKX2.5* expression (Fig. 46d, Fig. 19 and 20). This is the first evidence to date for the existence of proepicardial progenitors resembling the murine juxta-cardiac field in a human system. Further studies will be required to unravel the molecular processes underlying its specification and differentiation during epicardioid development.

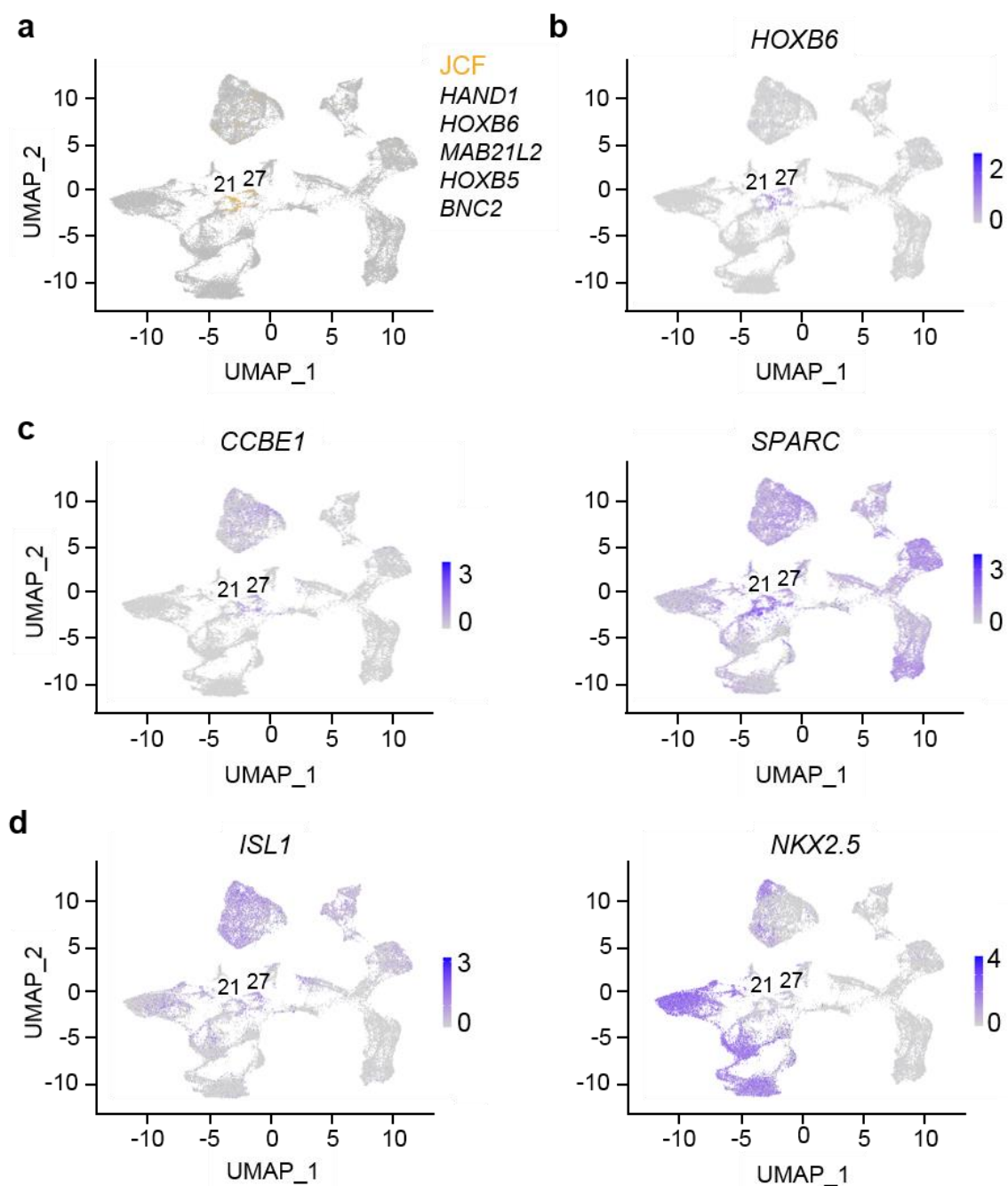


**Figure 46: Expression of juxta-cardiac field (JCF) markers during epicardioid formation.** (a) UMAP feature plot showing cells co-expressing markers of the JCF (*HAND1*, *HOXB6*, *MAB21L2*, *HOXB5*, *BNC2*) in epicardioids across all time points. (b-d) UMAP feature plots of *HOXB6* (b), *CCBE1*, *SPARC* (c), *ISL1* and *NKX2.5* (d) in epicardioids across all time points. Heatmaps indicate the respective level of expression of each gene. Relevant clusters mentioned in the text are annotated.

### 3.3.5 Epicardial cells signal to the myocardium

In mouse cardiogenesis, signaling from the epicardium is required for myocardial proliferation and formation of the compact layer<sup>45</sup>. To determine if similar processes are taking place in epicardioids, we evaluated cell-cell interactions mediated by ligand-receptor complexes using the publicly available tool CellPhoneDB<sup>151</sup>. Among cells present at day 15, the highest number of significant interactions was found between the epicardial cluster (23) and the cluster identified as compact myocardium (30) (Fig. 47a). In line with the cells' putative distance from the epicardial layer, there was a progressive decrease in interaction with the epicardial cluster between the cardiomyocyte clusters 30 (compact), 19, 1 (intermediate) and 12 (trabecular) (Fig. 47a).

The main signaling factor implicated in myocardial stimulation by the epicardium in mice is insulin-like growth factor 2 (IGF2)<sup>45,178</sup>. Among highly significant interactions between cluster 23 and clusters 30, 19, and 1 ( $p < 0.01$ ), we found the secretion of IGF2 by epicardial cells and expression of its receptors IGF1R and IGF2R in cardiomyocytes, suggesting an equivalent role in epicardioids (Fig. 47b). Other highly significant signals included transforming growth factor  $\beta$  (TGF $\beta$ 1), which plays key roles in epicardial function<sup>179</sup>, and interactions between fibronectin and integrin complexes (including integrin  $\beta$ 1,  $\alpha$ 5 and  $\alpha$ 3) (Fig. 47b). Fibroblast secretion of fibronectin binding to integrin  $\beta$ 1 has been shown to promote myocardial proliferation in mice<sup>180</sup>. As cluster 23 also contains epicardial-derived fibroblasts, experimental validation such as cell type-specific ablation of molecules of interest would be required to resolve the origin of these signaling molecules and their individual impact on myocardium patterning.

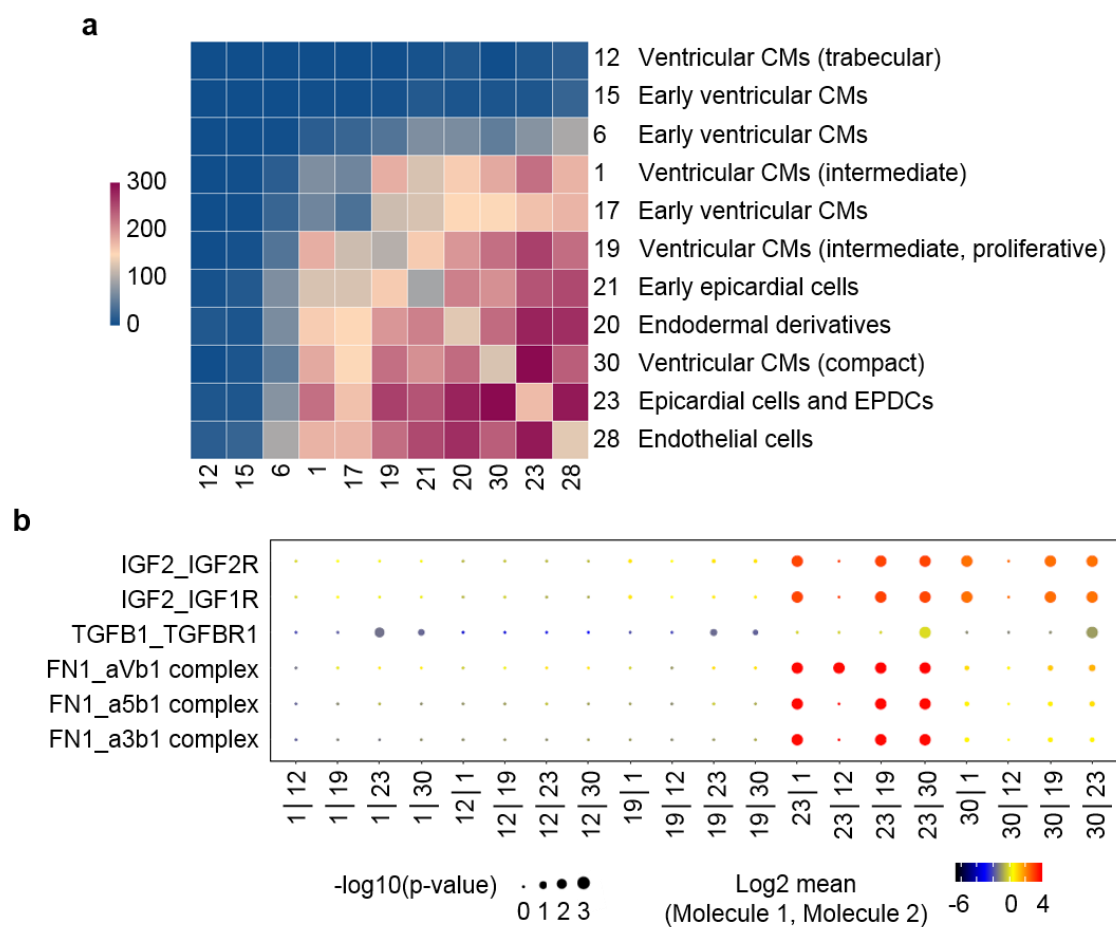


**Figure 47: Cell-cell interaction analysis indicates crosstalk between the epicardium and myocardium in epicardioids. (a)** Heatmap showing the number of significant interactions between cells present at day 15 in epicardioids, as determined by analysis of scRNA-Seq data with CellPhoneDB. Clusters containing less than 5 cells at this time point were excluded. **(b)** Dot plot showing putative ligand-receptor interactions between clusters 1, 19, 12, 30, and 23 (in both directions) at day 15. P-values are indicated by circle size, the mean of the level of expression of the two interacting molecules in the respective cluster are indicated by color.

## 3.4 Development of new platforms for in vitro modeling of cardiac disease and therapy

### 3.4.1 Modeling pathological cardiac hypertrophy in epicardioids

Having established that epicardioids recapitulate key facets of myocardial and epicardial development and function in vitro, we next aimed to test their potential for modeling cardiac disease and developing new therapies.

Pathological cardiac hypertrophy is a common adaptive response to cardiac stress such as hypertension and is a major risk factor for heart failure and cardiac death<sup>181,182</sup>. In contrast to physiological hypertrophy, thickening of the heart muscle in pathological hypertrophy is associated with progressive cardiomyocyte dysfunction and fibrosis, in a process that is still incompletely understood. Studies have shown that exposing hPSC-derived cardiomyocytes to pharmacological or mechanical hypertrophic stimuli is sufficient to trigger an increase in cell size and the upregulation of hypertrophic gene programs, making them useful tools to study hypertrophic phenotypes in vitro<sup>183,184</sup>. However, conventional cardiomyocyte cultures fail to recapitulate tissue-level aspects of hypertrophic remodeling such as the fibrotic response mediated by activated fibroblasts. We hypothesized that the functional self-organization of multiple cell lineages within epicardioids could make them ideal in vitro models to study the pathomechanisms of hypertrophy.

To test this, we treated day 30 epicardioids with 100 nM endothelin-1 (ET1), a potent vasoconstrictor known to induce hypertrophy in vivo and in vitro<sup>185-187</sup>. In concordance with previous studies, there was a significant upregulation of the hypertrophic markers *NPPA*, *NPPB*, and *ACTA1* in epicardioids treated with ET1 for 6 days compared to untreated controls (Fig. 48a). An increase in expression of the ECM genes type I collagen (*COL1A2*), type III collagen (*COL3A1*), and fibronectin (*FN1*) additionally suggested a fibrotic response (Fig. 48b).

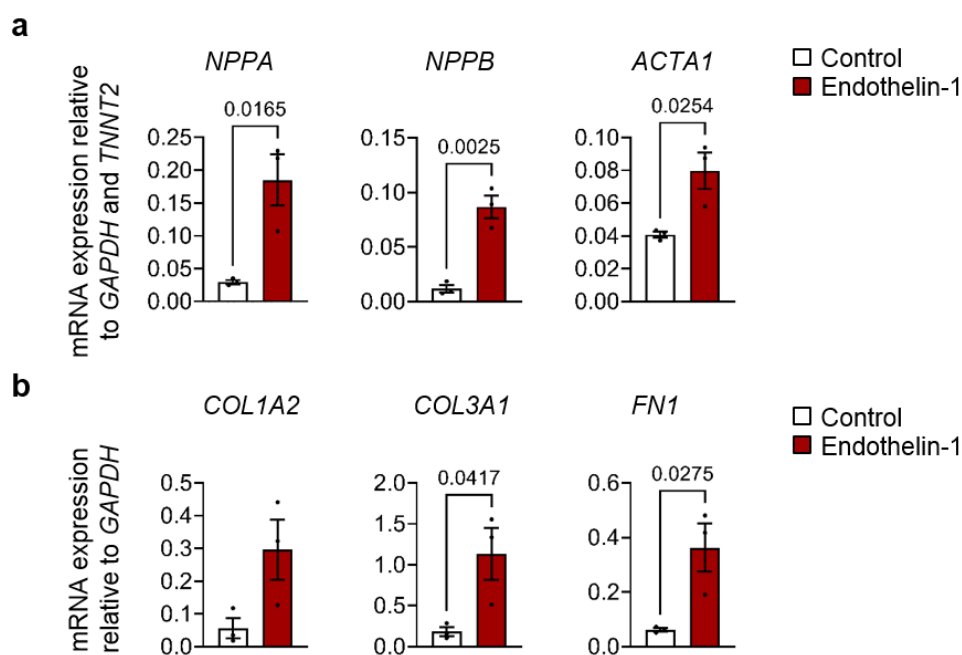


**Figure 48: Endothelin-1 induces the upregulation of hypertrophy markers and ECM genes.** (a,b) mRNA expression levels of *NPPA*, *NPPB*, and *ACTA1* relative to *GAPDH* and *TNNT2* (a) and mRNA expression levels of *COL1A2*, *COL3A1*, and *FN1* relative to *GAPDH* (b) in epicardioids after 6 days of treatment with 50 nM endothelin-1 compared to untreated controls, as determined by qRT-PCR. Bars show the mean  $\pm$  SEM and all data points;  $n = 3/\text{group}$ . P-values determined by unpaired two-tailed *t*-test.

Interestingly, immunofluorescence analysis showed that this ECM deposition was concentrated in the subepicardial space and was accompanied by an increase in cells positive for vimentin and  $\alpha$ -smooth muscle actin, a marker of myofibroblasts, suggesting the activation of epicardium-associated fibroblasts (Fig. 49). Of note, untreated controls also showed fibronectin expression in epicardial cells, as is the case in vivo<sup>188</sup> (Fig. 49). Although further investigations were out of the scope of this work, these preliminary results suggested that epicardioids could be suitable models to study the pathogenesis and treatment of hypertrophy in vitro.

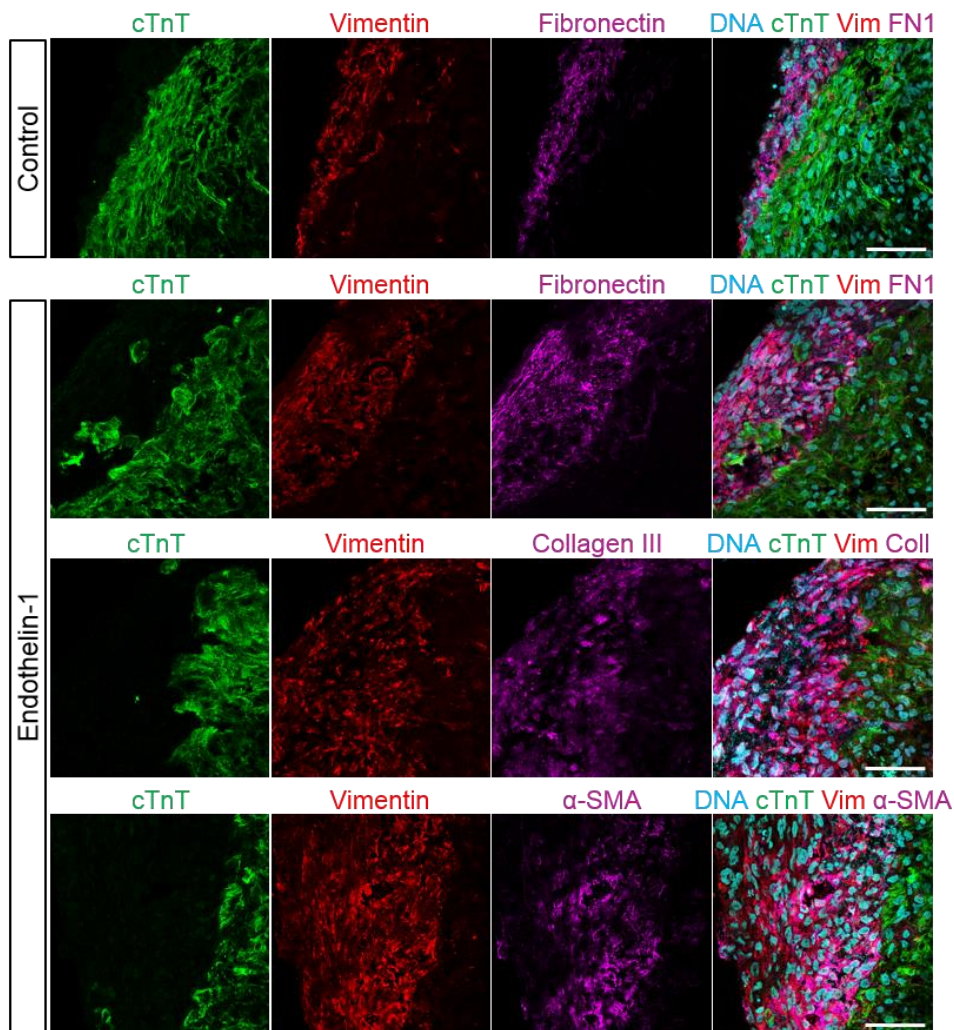


**Figure 49: Endothelin-1 induces subepicardial fibroblast activation and ECM deposition.** Representative images of cTnT, vimentin (Vim), fibronectin (FN1) type III collagen (Coll), and  $\alpha$ -smooth muscle actin ( $\alpha$ -SMA) immunostaining of epicardioids after 6 days of treatment with 100 nM endothelin-1 compared to untreated controls. Scale bars = 50  $\mu$ m.

### 3.4.2 AAV-mediated somatic gene editing in Duchenne muscular dystrophy

The advent of efficient and precise gene editing by CRISPR/Cas9 technology has opened new possibilities in disease modeling, especially in combination with complex 3D models such as organoids. It has also renewed hope for gene therapy, with the first clinical trial for in vivo CRISPR/Cas9 editing showing promising results for the treatment of the fatal disease transthyretin amyloidosis<sup>189</sup>. However, there are still significant issues to resolve before clinical application of gene editing can become widespread, notably the delivery of editing vectors to

specific cell types and the prevention of off-target effects. In addition to recapitulating disease phenotypes, organoids could be a suitable model to address some of these questions in vitro.

Currently, the most common strategy for gene editing in disease modeling is to manipulate the genome of undifferentiated iPSCs before clonal selection and differentiation into specific cell types or organoids. This can serve to introduce pathogenic mutations to cause a disease phenotype, or to correct mutations in patient-derived iPSCs to generate isogenic controls<sup>190,191</sup>. However, for advanced disease models as well as for testing gene therapy approaches, new methods must be developed to achieve efficient editing in terminally differentiated cells and organoids, which remains a technical challenge. Epicardioids could serve as a platform to test gene editing of cardiac cells in a tissue-like context, building upon our work on establishing AAV-mediated gene editing to correct a mutation causing Duchenne muscular dystrophy<sup>149</sup>.

Duchenne muscular dystrophy (DMD) is a devastating disease affecting 1 in 3,500-5,000 male newborns. It is caused by frameshift mutations in the *DMD* gene encoding dystrophin, a large protein belonging to a complex stabilizing the plasma membrane of striated muscle cells. In DMD, loss of dystrophin leads to progressive muscle degeneration and premature death due to respiratory and cardiac failure, and there is currently no cure. Our collaborators, led by Prof. Christian Kupatt (TUM), established a genetically engineered pig model of DMD by deleting *DMD* exon 52, causing a premature STOP codon preventing the translation of dystrophin. Having confirmed a severe DMD phenotype in these animals, they then tested the therapeutic potential of AAV-mediated CRISPR/Cas9 deletion of *DMD* exon 51, which would restore the reading frame and allow expression of a truncated but functional protein. AAVs (adeno-associated viruses) are the most promising delivery vectors for gene therapy because they efficiently transduce a wide range of both quiescent and dividing cells, do not integrate into the genome and are non-pathogenic to humans<sup>19</sup>. One drawback, however, is their relatively small packaging capacity of ~5 kb. Here, deletion of *DMD* exon 51 was performed by targeting flanking regions with two guide RNAs (gRNAs). As the length of the two gRNAs together with the sequence encoding *S. pyogenes* Cas9 would exceed the packaging capacity of a single AAV, a recently established split-intein Cas9 system was utilized to divide the sequence of the Cas9 into two AAVs additionally encoding one gRNA each<sup>192</sup>.

In parallel, we reprogrammed hiPSCs from a male DMD patient carrying a similar deletion of exon 52 (referred to as DMD $\Delta$ 52) to test various aspects of AAV-mediated editing in hiPSC-derived muscle cells, using gRNAs adapted to the human *DMD* locus (Fig. 50a,b). For

comparison, we also generated an isogenic corrected line by performing ribonucleoprotein (RNP)-mediated CRISPR/Cas9 editing at the undifferentiated hiPSC stage followed by clonal selection (referred to as DMD $\Delta$ 51-52) (Fig. 50c,d). A healthy male hiPSC line was additionally used as an independent control; the detailed characterization of the three lines can be found in<sup>149</sup>.

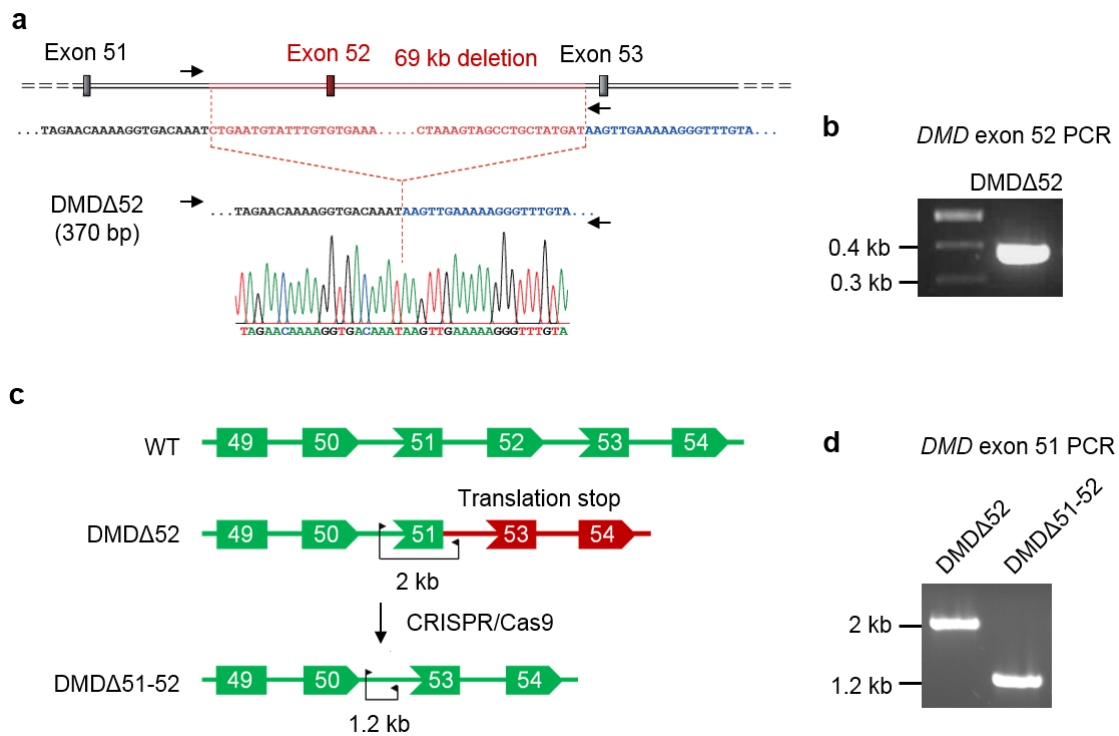


**Figure 50: Reprogramming of hiPSCs from a Duchenne muscular dystrophy patient (DMD $\Delta$ 52) and generation of an isogenic corrected line (DMD $\Delta$ 51-52).** (a,b) Schematic representation of the deletion of *DMD* exon 52 in DMD $\Delta$ 52 hiPSCs (a) and corresponding genomic PCR result after amplification with the indicated primers (arrows) (b). (c,d) Schematic representation of the frameshift mutation of *DMD* exon 52 in DMD $\Delta$ 52 hiPSCs and the restored reading frame after CRISPR/Cas9 deletion of exon 51 in DMD $\Delta$ 51-52 hiPSCs (c). Corresponding genomic PCR results after amplification with the indicated primers (arrows) in DMD $\Delta$ 52 hiPSCs and clonally selected DMD $\Delta$ 51-52 hiPSCs. Adapted from Moretti et al. 2020, *Nature Medicine*<sup>149</sup>.

Testing of AAV-mediated somatic editing in human cells was done in both hiPSC-derived cardiomyocytes and skeletal muscle cells; here, the focus will lie on results obtained in

cardiomyocytes. After cardiac induction of hiPSCs in 2D monolayers, day 30 DMD $\Delta$ 52 cardiomyocytes were transduced with the two AAVs carrying the sequences for the split-intein Cas9 and the gRNAs targeting DMD exon 51 (referred to as AAV6-Cas9/gE51) (Fig. 51a). Genomic PCR showed that a 20-hour incubation with  $10^6$  viral particles of each AAV per cell successfully induced the deletion of *DMD* exon 51 with an efficiency of  $43.6 \pm 26.4\%$  (Fig. 51b,c). This translated to dystrophin protein levels corresponding to  $48.7 \pm 30.5\%$  of the control cardiomyocytes (Fig. 51d,e). As expected, the dystrophin levels in cardiomyocytes derived from corrected DMD $\Delta$ 51-52 hiPSCs were equivalent to that of control cells ( $97.1 \pm 12.7\%$ ) (Fig. 51d,e).

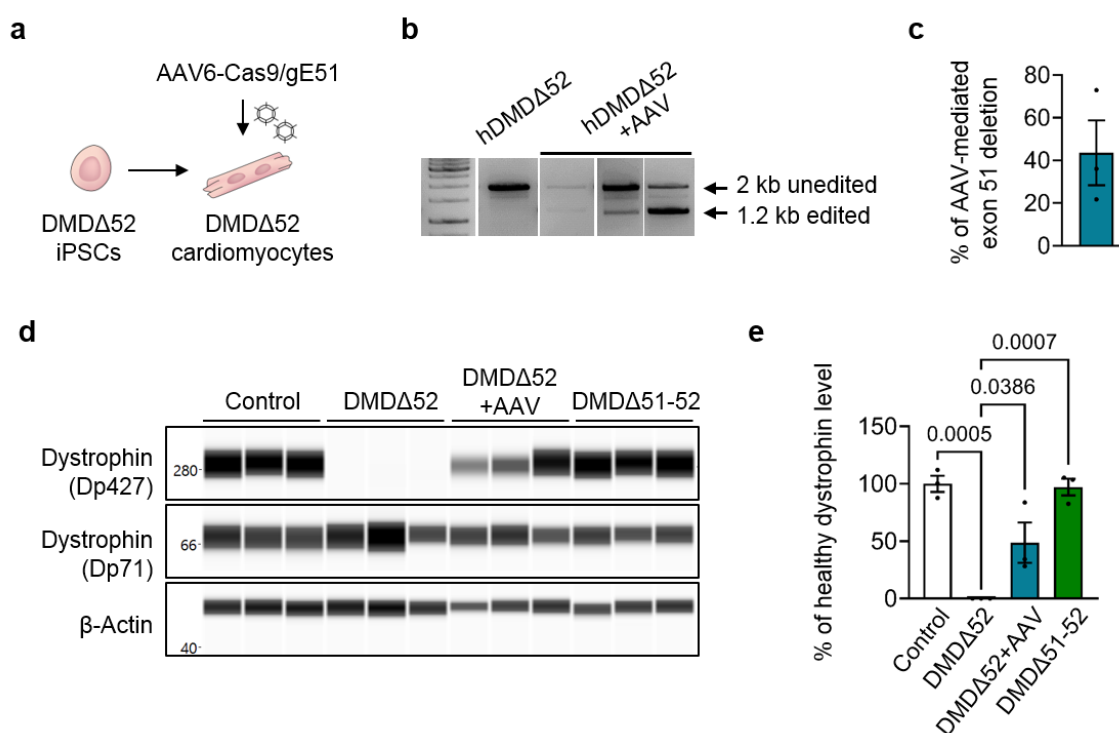


**Figure 51: AAV-mediated CRISPR/Cas9 deletion of exon 51 restores dystrophin expression in DMD $\Delta$ 52 hiPSC-derived cardiomyocytes.** (a) Schematic representation of somatic gene editing by dual AAV6-Cas9/gE51 transduction of DMD $\Delta$ 52 hiPSC-derived cardiomyocytes. (b,c) Genomic PCR analysis of AAV-mediated CRISPR/Cas9 deletion of exon 51 in DMD $\Delta$ 52 hiPSC-derived cardiomyocytes (b) and corresponding quantification of the percentage of deletion, indicating the mean  $\pm$  SEM and all data points;  $n = 3$ . (d,e) Dystrophin detection by capillary immunoassay in control, untreated DMD $\Delta$ 52, AAV6-Cas9/gE51-transduced DMD $\Delta$ 52 and DMD $\Delta$ 51-52 cardiomyocytes using  $\beta$ -actin as a loading control (d). The antibody detects the dystrophin isoforms Dp427 and Dp71, the latter being unaffected by the deletion of *DMD* exon 52. Corresponding quantification of

dystrophin (Dp427) levels relative to control cardiomyocytes, indicating mean  $\pm$  SEM and all data points;  $n = 3$ . P-values obtained by one-way ANOVA with Tukey's multiple comparisons test. (e) Adapted from Moretti et al. 2020, *Nature Medicine*<sup>149</sup>.

We next evaluated if AAV-mediated somatic gene editing could alleviate disease phenotypes in hiPSC-derived cardiomyocytes. In DMD pigs, calcium transient analysis in cardiac tissue slices revealed pathological arrhythmogenic susceptibility that could be reduced by CRISPR/Cas9 deletion of exon 51<sup>149</sup>. To perform equivalent analyses of calcium handling in 2 months-old hiPSC-derived cardiomyocytes, we used a dual AAV6-Cas9-gE51 system in which each AAV additionally encoded fluorescent reporters: either eGFP (referred to as AAV6-N-Cas9-gE51-eGFP) or mCherry (referred to as AAV6-C-Cas9-gE51-mCherry). This allowed us to select eGFP<sup>+</sup>/mCherry<sup>+</sup> cells having received both AAVs for single-cell calcium transient analysis with Fluo-4 (Fig. 52a). The first observation was that under equal 1 Hz pacing conditions, untreated DMD $\Delta$ 52 cardiomyocytes had prolonged calcium transients, as indicated by significantly longer duration to 90% peak decay (TD<sub>90</sub>), compared to control and isogenic corrected DMD $\Delta$ 51-52 cardiomyocytes (Fig. 52b,c). AAV treatment successfully rescued this phenotype (Fig. 52b,c). In addition, we observed recurring arrhythmic events triggered by electrical stimulation in DMD $\Delta$ 52 cardiomyocytes, which were absent in control cells and rare in DMD $\Delta$ 51-52 cells (Fig. 52d,e). This pathological feature was also rescued by AAV treatment, providing additional evidence that restoration of dystrophin expression by somatic gene editing was sufficient to ameliorate functional defects in hiPSC-derived cardiomyocytes (Fig. 52e).

This study showed the high potential of AAV-based delivery of CRISPR/Cas9 components for somatic editing of differentiated cells. In further studies, the technology could be transferred to epicardioids to develop a platform for testing AAV-based gene editing in a tissue-like context.

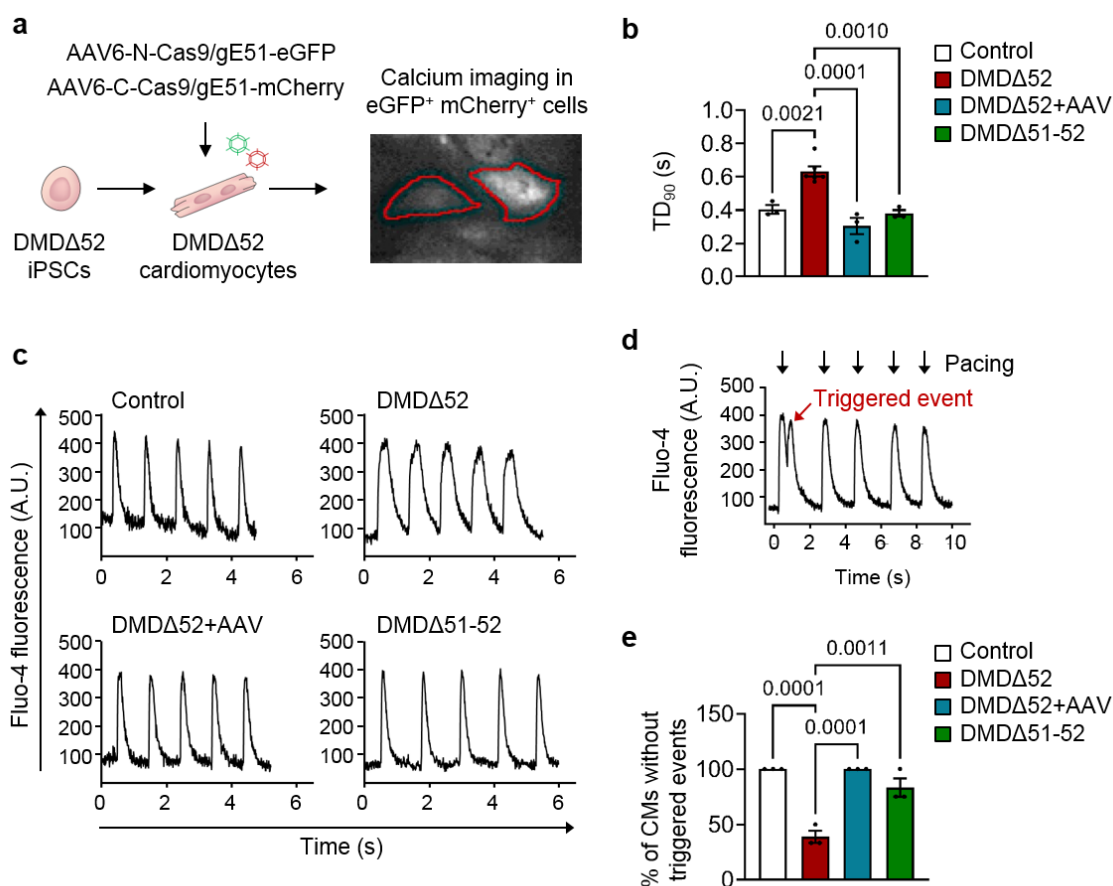


**Figure 52: AAV-mediated somatic gene editing rescues calcium handling defects in DMDΔ52 hiPSC-derived cardiomyocytes.** (a) Schematic representation of somatic gene editing of DMDΔ52 hiPSC-derived cardiomyocytes with two AAV6-Cas9/gE51 vectors additionally encoding either eGFP (AAV6-N-Cas9/gE51-eGFP) or mCherry (AAV6-C-Cas9/gE51-mCherry) to select double-positive cells for calcium imaging. (b) Duration of single-cell calcium transients to 90% of peak decay (TD<sub>90</sub>) in control, untreated DMDΔ52, AAV6-Cas9/gE51-eGFP/mCherry-transduced DMDΔ52, and DMDΔ51-52 cardiomyocytes, indicating the mean ± SEM and all data points; n = 3 except for DMDΔ52, n = 6. P-values determined by one-way ANOVA with Tukey's multiple comparisons test. (c) Exemplary single-cell traces of Fluo-4 fluorescence at 1 Hz pacing in control, untreated DMDΔ52, AAV6-Cas9/gE51-eGFP/mCherry-transduced DMDΔ52, and DMDΔ51-52 cardiomyocytes. (d,e) Exemplary single-cell trace of Fluo-4 fluorescence at 0.5 Hz pacing in untreated DMDΔ52 cardiomyocytes, showing a triggered event. (d) Corresponding quantification of the percentage of cardiomyocytes (CMs) without triggered events among control, untreated DMDΔ52, AAV6-Cas9/gE51-eGFP/mCherry-transduced DMDΔ52, and DMDΔ51-52 cardiomyocytes, indicating the mean ± SEM and all data points; n = 3. P-values determined by one-way ANOVA with Tukey's multiple comparisons test. Analysis performed by Tobias Haufe and Dr. med. Daniel Sinnecker. Adapted from Moretti et al. 2020, *Nature Medicine*<sup>149</sup>.

## 4 Discussion

Engineering cardiac tissue in a dish has been a long-standing pursuit of the cardiovascular field<sup>109,193</sup>. The main underlying goal is to generate 3D models of cardiac development and disease that recapitulate in vivo physiology better than 2D cell culture systems<sup>194,195</sup>. Additionally, there is hope that in vitro generated tissue substitutes may one day be used in cardiac regenerative medicine<sup>196</sup>. Over the last decade, incredible advances have been made in the generation of self-organized tissue mimics from pluripotent stem cells, which have been termed organoids<sup>197</sup>. Their similarity to respective organs in terms of development, cell composition, morphology, and function makes them precious tools in a wide range of applications in biomedical research. However, compared to other systems of the body including the gut, brain, and lung, the generation of cardiac organoids has remained elusive.

Here, we report the first human pluripotent stem cell-based model of cardiogenesis displaying self-organization of ventricular myocardium and epicardium. We show that the unprecedented morphological, functional, and molecular self-patterning of the myocardium in this system makes it a highly promising in vitro model of cardiac development and disease. Moreover, we demonstrate the utility of somatic gene editing for the rescue of disease phenotypes in hiPSC-derived cardiomyocytes, with the perspective of advancing gene therapy in cardiovascular medicine.

### **4.1 Retinoic acid promotes the self-organization of myocardial and epicardial layers during 3D cardiac induction of human pluripotent stem cells**

The importance of retinoic acid signaling in cardiogenesis is demonstrated by the cardiovascular defects caused by both deficiency and excess of retinoids during prenatal and postnatal development<sup>198,199</sup>. Extensive studies in mouse and avian embryos have shown that during early cardiogenesis, retinoic acid is required to define the posterior boundary of the second heart field and to activate the expression of *Tbx5*<sup>156,157</sup>. This was reflected during in vitro cardiac induction of hPSCs, as the addition of retinoic acid during both 2D and 3D differentiation was sufficient to obtain a significant enrichment of TBX5<sup>+</sup> FHF progenitors and their derivatives. Strikingly, in the 3D setting only, retinoic acid additionally triggered the

self-organization of an inner myocardial mass and an outer epicardium-like layer, which was reproducible across multiple hPSC lines. This layer was further divided into an outer mesothelial layer and a subjacent region of cells expressing epicardial but not epithelial markers, suggesting that they underwent EMT to give rise to EPDCs. This was supported by the significant enrichment of mesenchymal cells within the myocardial layer of these structures we termed epicardioids compared to control spheroids generated without retinoic acid. Single-cell RNA-Seq time course analysis in epicardioids additionally confirmed the presence of cell populations closely matching transcriptional signatures of human epicardial cells, EPDCs, and epicardial-derived fibroblasts and smooth muscle cells.

Retinoic acid has previously been implicated in epicardial development and can be used in combination with Wnt and BMP signaling to differentiate pluripotent stem cells into epicardial cells *in vitro*<sup>198,200,201</sup>. In epicardioids, single-cell RNA sequencing revealed the presence of a cell population corresponding to juxta-cardiac field (JCF) progenitors, which have recently been identified as common progenitors of myocardium and epicardium located at the rostral border of the cardiac crescent in the mouse<sup>40,41</sup>. To our knowledge, this is the first evidence for the existence of this pool of progenitors in a human system. As lineage tracing showed that the JCF is a subset of the FHF in the mouse, this was congruent with predominant FHF specification in epicardioids<sup>41</sup>. *HOXB6*, which has been implicated in the specification of the JCF *in vivo* and was specific to JCF cells in epicardioids, was significantly upregulated during induction in epicardioids but not in control spheroids lacking retinoic acid treatment and failing to establish an epicardial layer. As *HOXB6* expression can be directly induced by retinoic acid<sup>202</sup>, this further supported JCF specification as the underlying mechanism of epicardial layer formation upon retinoic acid treatment. Interestingly, early control spheroids did transiently form a putative epicardial outer layer that was then quickly lost during further development. This was visible by immunofluorescence analysis of sections as well as by transcriptomic analysis of epicardial markers, which, in contrast to epicardioids, showed early upregulation but not maintenance of expression in control spheroids. As the JCF markers *HAND1* and *MAB21L2* as well as low *HOXB6* expression could be detected in early control spheroids, this transient layer may derive from weak specification of a JCF-like population that, in the absence of retinoic acid signaling, was not sufficient for the proper formation and maintenance of an epicardial layer. However, our current understanding is that the JCF is one of several progenitor populations contributing to the epicardial lineage *in vivo*<sup>41</sup>. Considering the significant effect of retinoic acid treatment on progenitor specification, these cells may

therefore represent a developmentally distinct pool of epicardial progenitors. As mentioned above, the addition of retinoic acid during *in vitro* cardiac induction of hiPSCs activated a transcriptional program typical of the FHF, while the absence of retinoic acid was associated with SHF identity. As SHF progenitors have been shown to contribute to the proepicardial lineage in the mouse<sup>203</sup>, it is possible that control spheroids and epicardioids form distinct SHF and FHF-associated epicardial lineages, respectively, and that the culture conditions – or inherent properties of the progenitors – only allow the maintenance of an epicardial layer in epicardioids.

Intriguingly, a very similar protocol for 3D cardiac induction of hPSCs including the same concentration and timing of retinoic acid was recently reported to induce the self-organization of myocardial and endocardial compartments but not the epicardium<sup>121</sup>. This difference in outcomes may be attributed to the pleiotropic roles of retinoic acid during cardiogenesis, or to differing culture conditions. In particular, the authors initiated differentiation from significantly lower cell numbers (2,500-7,500 cells vs 30,000-40,000 cells for epicardioids) and did not provide external ECM support, two parameters that significantly influenced epicardioid development. As they also described optimal CHIR99021 and Activin A concentrations to be essential for the formation of the inner lining of endocardial cells, differences between their protocol and ours in this regard (CHIR: 4  $\mu$ M vs 1.5  $\mu$ M for epicardioids; Activin A: 4 ng/mL vs 50 ng/mL for epicardioids) may also be at play. Nevertheless, one can speculate based on these complementary findings that with the right dosage of signaling factors, such a protocol may eventually allow the generation of bona fide cardiac organoids forming all three layers – myocardium, epicardium, and endocardium.

## **4.2 Epicardioids show unprecedented morphological, molecular, and functional patterning of the myocardial layer**

The epicardium is an essential regulator of myocardium morphogenesis and specifically ventricular compaction, as evidenced by the hypoplastic ventricular wall resulting from surgical or genetic ablation of the epicardium<sup>47,48</sup>. In addition to providing epicardial-derived fibroblasts and smooth muscle cells, the presence of the epicardial layer in epicardioids was associated with myocardial patterning typical of the ventricular wall.

The subepicardial layer of cardiomyocytes was more compact than the inner layer, as reflected by a higher density of cardiomyocytes, which could be linked to increased cardiomyocyte proliferation. Beyond spatial organization, cardiomyocytes within this wall-like structure also adopted molecular signatures specific of compact, trabecular, and intermediate cardiomyocytes detected by single-cell transcriptomic analysis. Importantly, we could also observe functional features characteristic of transmural patterning in vivo. In the heart, cardiomyocytes closest to the epicardial layer are the last to be depolarized and the first to be repolarized, resulting in a shorter action potential duration compared to cardiomyocytes closer to the endocardium<sup>168</sup>. Results from both calcium transient imaging and optical action potential recordings indicated that cardiomyocytes closest to the epicardial layer in epicardioids had shorter action potentials than cardiomyocytes of the inner layer after 30 days of differentiation. This was not due to faster maturation in the outer layer, which could also decrease action potential duration, because cardiomyocytes with a compact identity showed the lowest molecular maturation, as is the case in vivo<sup>175</sup>. The fact that age-matched control spheroids lacking an epicardial layer did not show compaction or action potential shortening in the outer layer confirmed that this does not occur spontaneously in any 3D cardiac structure.

Funakoshi et al. recently established a protocol for the controlled generation of mature compact ventricular cardiomyocytes from hPSCs, which could serve as a cell source for in vitro disease modeling or regenerative approaches<sup>173</sup>. However, this is a 2D system based on the staged addition of growth factors and metabolic regulators, which does not resemble the 3D morphogenetic process of compact layer formation. Self-patterned 3D models of early cardiogenesis derived from murine ESCs have been reported but were limited to early developmental stages corresponding to the cardiac crescent<sup>204,205</sup>. Epicardioids therefore constitute the first in vitro cardiac mimics showing advanced morphological and functional self-organization of the myocardium in a tissue-like context, which we believe to be driven at least in part by interaction with the epicardial layer. In the mouse, the epicardium was shown to stimulate myocardial proliferation and compaction via the secretion of mitogens such as IGF2, FGF2, and FGF9<sup>44,166</sup>. The major role of IGF2 in this process is illustrated by the fact that the global deletion of *Igf2* or conditional deletion of the IGF receptors *Igfr1* and *Insr* in the myocardium each result in ventricular wall hypoplasia<sup>178</sup>. A comparable phenotype is obtained after cardiomyocyte-specific deletion of integrin  $\beta 1$ , which was shown to promote myocardial proliferation after binding of ECM proteins including fibronectin<sup>180</sup>. Single-cell RNA-Seq revealed significant crosstalk between the epicardium and the myocardium in epicardioids and

suggested that these signals, among others, could also be contributing to myocardial self-patterning *in vitro*. A requirement for paracrine epicardial signaling could explain why recently established models containing myocardium and an endocardium-like compartment but not the epicardium did not show morphological or functional self-patterning of the myocardial layer<sup>120,121,206</sup>. Recently, Lewis-Israeli and colleagues used a protocol based on Wnt signaling modulation to generate 3D cardiac structures showing spontaneous emergence of epicardial cells, which formed individual clusters mainly localized at the outer layer of cardiomyocytes and sometimes in the inner layer<sup>122</sup>. However, the author observed neither the formation of an outer compact layer of cardiomyocytes nor functional patterning of the myocardium (although the latter was likely not tested). While several factors may be at play, this suggests that the presence of epicardial cells is not sufficient to stimulate myocardial patterning and that the self-organization of a mature epicardial layer is necessary. Based on the heterogeneity of the epicardial population in epicardioids, as reflected by differential expression of epithelial markers as well as *ISL1*, one can also speculate that a specific subset of epicardial cells is responsible for stimulating myocardial patterning and that these cells may not be present in the structures obtained by Lewis-Israeli et al.

#### **4.2 Epicardioids as *in vitro* models of the human (pro)epicardium**

During cardiogenesis, the epicardium is the source of several cardiac cell types and secretes signaling molecules critical to the development of the myocardium. Animal studies have shown that some of these embryonic programs are re-activated in the adult epicardium during cardiac repair after injury, making it a promising target for regenerative therapies<sup>207</sup>. However, the mechanisms underlying these developmental and regenerative processes in humans are still unclear, in part due to a lack of human models of (pro)epicardial function.

Native human proepicardial progenitors are virtually inaccessible, as they appear in the embryo less than four weeks post-conception, at which point pregnancy may not yet be detected<sup>160</sup>. Later epicardial cells, although somewhat easier to obtain, are difficult to study *ex vivo* because they quickly undergo spontaneous EMT and lose epicardial identity<sup>160,208</sup>. This can be circumvented by generating epicardial cells and their progeny *in vitro* from human pluripotent stem cells<sup>85,201,209–211</sup>. However, these 2D systems lack many facets of *in vivo* physiology. In the few (semi)-self-organized 3D cardiac models including an epicardial compartment, it was either

added externally<sup>121</sup> or consisted of unorganized clusters of cells<sup>122</sup>. By contrast, we could show that epicardioids recapitulate the stepwise formation of proepicardial progenitors, a mature epicardial layer, EPDCs, and epicardial-derived fibroblasts and smooth muscle cells, making them uniquely suited to study the epicardial lineage in a physiologically relevant human system. Importantly, this epicardial compartment was maintained over a prolonged time in culture by continuous self-renewal, providing an adequate time frame for experiments. The expression profile of sarcomeric proteins also showed maturation of the myocardial compartment over time.

The analysis of the single-cell RNA-Seq time course of epicardioid development presented in this work was limited in scope, and the dataset could be explored further from many different angles. As they harbor a JCF-like population that was previously only described in the mouse<sup>40,41</sup>, data from epicardioids could for example help dissect potential differences between the murine and human JCF populations. We could already observe that in contrast to murine epicardial cells, the expression of *ISL1* is maintained in human epicardial cells in both directly differentiated cells and epicardioids. More broadly, epicardioids offer the possibility to tackle many open questions in the field. One debated aspect is the heterogeneity of various (pro)epicardial cell populations; specifically, it is still unclear at which stage the ultimate fate of epicardial cells is determined – at the proepicardial stage, in epicardial cells before EMT, or after EMT. Several groups have described heterogeneity in proepicardial or epicardial cells in mice<sup>212,213</sup>, zebrafish<sup>214</sup>, and hiPSC-derived epicardial cells<sup>215</sup>, attributing specific differences in gene expression to downstream fate decisions. Conversely, a recent study in mice suggested that differences in marker expression in proepicardial and epicardial cells did not restrict their fate, which was determined after EMT<sup>216</sup>. One strategy to address this question in epicardioids would be to combine single-cell RNA-Seq with single-cell ATAC-Seq (Assay for Transposable-Accessible Chromatin using sequencing), which uncovers genome-wide chromatin accessibility<sup>217</sup>. This could reveal if cells with seemingly homogeneous transcriptional profiles show differences in chromatin accessibility in loci linked to fate determination, as has been done in other organ systems<sup>218,219</sup>. Generating epicardioids from hPSC reporter lines allowing lineage tracing of cells expressing markers of interest could then be used for functional validation.

### 4.3 Applications of epicardioids in disease modeling and drug screening

Pluripotent stem cell-derived cardiomyocytes have become well-established tools for studying disease mechanisms and testing novel therapeutic approaches<sup>220,221</sup>. They have been shown to recapitulate key pathological features when carrying disease-causing mutations<sup>89,90,222</sup> or when submitted to toxic stimuli<sup>223</sup>. One area of study in hPSC-derived cardiomyocytes has been the mechanisms underlying cardiac hypertrophy, a common adaptive response to cardiac stress that leads to reduced capacity of the heart to pump blood to the tissues of the body. Several groups have shown that hPSC-derived cardiomyocytes are sensitive to mechanical and pharmacological hypertrophic stimuli such as endothelin-1, angiotensin-II, phenylephrine, or free fatty acids in 2D cultures<sup>183–185</sup>. These studies yielded valuable insights into the cell-autonomous hypertrophic response of cardiomyocytes, but there is a lack of information about other cell types involved in hypertrophy *in vivo*. Specifically, cardiac fibroblasts play a pivotal role in several processes of cardiac remodeling, secreting extracellular matrix components and communicating with cardiomyocytes via signaling molecules<sup>224</sup>. Accordingly, increased collagen deposition mediated by cardiac fibroblasts was observed in a 3D model of hypertrophy generated from a mix of ventricular cells from rat hearts<sup>225</sup>. However, it is unclear to what extent such engineered tissues resemble the microenvironment of the human heart. By contrast, epicardioids combine the advantages of multicellularity and relevant spatial self-organization in a human setting. First experiments showed that endothelin-1 stimulation of epicardioids induced the expected upregulation of hypertrophic markers as well as increased expression of fibrosis-related genes. Importantly, the latter reflected myofibroblast activation and increased deposition of ECM proteins that were not diffuse but specifically localized in the subepicardial region. While this could be due to higher exposure of resident fibroblasts to endothelin-1 molecules at the outer layer, it may also indicate *de novo* generation of epicardium-derived fibroblasts. Resolving this question may lead to insights on how to manipulate the epicardium to regulate the heart's response to stress, an ongoing pursuit in the field inspired by the essential role played by the epicardium in heart regeneration in lower vertebrates<sup>226</sup>. Our lab recently established an acute injury model based on radiofrequency ablation (RFA) in native tissue cultured *ex vivo*, which was used to test the potential of cell therapy in promoting tissue regeneration over fibrosis<sup>227</sup>. Phenotypical comparisons between hypertrophic and RFA-injured epicardioids may be an interesting avenue of study, as it is still debated which populations of fibroblasts are driving cardiac fibrosis in different pathological

settings *in vivo*<sup>228</sup>. This could eventually culminate in high-throughput screenings in epicardioids to identify disease-specific anti-fibrotic compounds.

Moreover, the self-patterning of the myocardium in epicardioids would make them particularly suited to study disorders affecting morphogenesis of the ventricular wall, such as left ventricular non-compaction (LVNC) or cardiomyopathy associated with Noonan syndrome (NS-CM). We recently identified cardiomyocyte cell cycling defects as a previously undescribed driver of NS-CM, using both native myocardial tissue and patient-specific hiPSC-derived cardiomyocytes cultured in 2D (Meier et al., under review). As Noonan syndrome is a “RASopathy” caused by mutations in the Ras/MAPK pathway, a promising treatment strategy is the application of small molecules targeting specific components of this pathway, which are already available for oncologic indications<sup>229–232</sup>. Epicardioids would be a useful 3D model to evaluate the potential of such compounds in attenuating hypertrophy in NS-CM. In this and any other pathophysiological context, epicardioids could also be used to study the crosstalk between different cardiac cell types, which can be resolved by single-cell RNA-Seq via algorithms deciphering cell-cell communication<sup>233,234</sup>. As presented in this work, calcium transient or action potential analyses in epicardioid slices additionally allow the identification of functional differences between cardiomyocytes with a compact vs trabecular identity. It can be noted that advanced microscopy methods allowing high-resolution imaging in 3D structures, such as two-photon excitation microscopy, may circumvent the need for sectioning<sup>235</sup>.

Another potential area of application for epicardioids could be cardiotoxicity assays. Cardiotoxicity is one of the most common adverse drug effects and a major cause of withdrawal from clinical trials or the market<sup>236</sup>. This holds true across multiple drug classes including antineoplastic agents, agents targeting the central nervous system and, paradoxically, cardiovascular drugs<sup>237</sup>. Cardiotoxic effects are mainly associated with the disruption of electrophysiological function, contractility, mitochondrial function, and growth factor signaling, among other mechanisms. The increase in drug attrition due to cardiac safety concerns in the last decades is a sign of raised standards in pharmacovigilance, but it also suggests that current preclinical models are not adequate predictors of cardiotoxicity. Recently, treatment of organoids with various compounds was shown to generate responses close to those obtained in primary tissues and *in vivo* models<sup>238</sup>. For example, screening in midbrain organoids correctly identified known nigrostriatal toxicants and identified a new substance as

a selective toxicant for dopaminergic neurons for the first time<sup>239</sup>. Epicardioids may therefore also be a promising model for toxicological investigations.

#### **4.4 Somatic gene editing: from bench to bedside**

Recent advances in CRISPR/Cas9 technology including prime editing<sup>140</sup>, base editing<sup>139</sup>, and transcriptional regulation by CRISPR interference (CRISPRi) and activation (CRISPRa)<sup>240</sup> have vastly expanded the biomedical research toolbox. In addition to facilitating countless strategies for genetic manipulation *in vitro*, this has paved the way for a new CRISPR era of gene therapy.

In 2021, a landmark clinical trial showed that transthyretin amyloidosis, a disorder caused by accumulation of misfolded transthyretin (TTR) protein in tissues, could be successfully attenuated by intravenous infusion of lipid nanoparticles containing Cas9 mRNA and a sgRNA targeting the TTR-encoding gene<sup>189</sup>. In this instance, CRISPR/Cas9 editing was employed to introduce random indels leading to frameshift mutations preventing translation of the protein. However, the treatment of most genetic disorders including cardiomyopathies will require precise genetic modifications including single nucleotide changes, which are currently much more difficult to achieve with high efficiency than gene disruption. The ongoing optimization of CRISPR editors promises rapid improvement in this regard, but there are still several issues to tackle for clinical applications. In light of tragic deaths caused by insertional oncogenesis in early gene therapy trials<sup>241</sup>, a major concern is the off-target effects potentially occurring during CRISPR/Cas9 editing<sup>242</sup>. Of note, the method of delivery has a significant influence on both efficacy and safety. A significant advantage in treating transthyretin amyloidosis was that the target was the liver, which readily takes up lipid particles from the blood via binding of apolipoprotein E (ApoE)<sup>189</sup>. For organs that are more difficult to target, including the heart, the most promising delivery modality remains adeno-associated virus (AAV) vectors<sup>15,19</sup>. However, only two AAV-based gene therapies have reached the clinic so far and there are many hurdles still remaining<sup>22</sup>.

In collaboration with the research group of Prof. Christian Kupatt, we showed that a dual AAV system encoding a split-intein Cas9 and two gRNAs could efficiently restore expression of the dystrophin protein in a pig model of Duchenne muscular dystrophy (DMD) as well as in muscle cells derived from DMD patient hiPSCs<sup>149</sup>. This was associated with an amelioration of disease phenotypes both *in vivo* and *in vitro*, specifically calcium handling defects in

cardiomyocytes. To bring this approach a step closer to clinical application, epicardioids could serve as a platform for further testing of AAV-mediated somatic gene editing in a human, tissue-like context. With respect to the data gained in hiPSC-CMs cultured in 2D, a compact 3D environment would yield more relevant insights on delivery efficiency and the percentage of editing needed for beneficial effects at the tissue level. The presence of multiple cell populations in an organized microenvironment could also help optimize AAV capsid composition – i.e., serotype and potential chemical modifications – to target or avoid specific cell types. This concept has already been applied in brain, lung, and retinal organoids to evaluate the efficacy, kinetics, and cell tropism of different AAV serotypes<sup>145,146,243</sup>. Aiming to correct different types of disease-causing mutations in epicardioids generated from patient hiPSCs would also allow systematic comparison of various CRISPR editors regarding efficiency and incidence of off-target effects, including recently developed compact CRISPR systems promising easier packaging into AAVs<sup>244,245</sup>. Finally, an intriguing possibility would be to use organoids edited *in vitro* for cell therapy approaches, as they have been shown to engraft well in relevant tissues<sup>246,247</sup>.

### 4.3 Limitations and outlook

As presented in the previous sections, epicardioids are a novel *in vitro* model of cardiogenesis displaying unprecedented morphological and functional self-organization of myocardial and epicardial compartments. However, they fail to establish the endocardial layer of the heart, thus falling short of the definition of a *bona fide* cardiac organoid (it is worth noting that others have not been so stringent with the nomenclature of their own models). This is likely due to the predominant FHF specification driven by retinoic acid treatment, which appears to drastically suppress the contribution of SHF derivatives including endocardial cells. Accordingly, among the cell types present, the percentage of cardiomyocytes is too high compared to the composition of the human heart (representing just under 50% of cells in the adult ventricle<sup>248</sup> vs close to 90% in epicardioids) and there is a paucity of non-myocytes, particularly endothelial cells. It can be reasonably expected that the relative cell composition could be refined in further studies by tweaking the culture conditions. There are also other strategies available to increase the complexity and physiological relevance of organoids. The main concern of all organoid systems is that they do not form a functional vasculature, which is a key component of most organs. So far, the most straightforward way to address this has

been to transplant organoids into animal tissue, leading to the development of robust host-derived vascularization as well as increased organoid maturation<sup>249,250</sup>. Tissue engineering techniques including the culture of organoids in microfluidic chips are also being developed to promote the formation of vessel-like structures *in vitro*<sup>251</sup>. For other missing cell compartments, inspiration could be taken from the field of brain organoids, which has progressed to fusing organoid models of different regions of the brain into so-called “assembloids”<sup>252</sup>. This has allowed groups to model complex processes such as interneuron migration and the formation of long-distance neuronal projections<sup>253–255</sup>. In the case of the heart, one could envision the fusion of epicardioids with structures containing SHF progenitor derivatives, such as atrial cardiomyocytes and endothelial cells. To address certain questions, co-culture with neural progenitors<sup>256</sup> or immune cells<sup>257</sup> could provide neural innervation and an immunological component, respectively. Even complex processes of human innate and adaptive immune responses have been recently recapitulated in organoids, which may become relevant for assessing AAV immunogenicity *in vitro*<sup>258–260</sup>. On the long term, preclinical research would vastly benefit from advanced human “body-on-a-chip” models consisting of several interconnected organoids simulating the crosstalk between different organs of the body<sup>261,262</sup>. This would for example allow early identification of drug side-effects in secondary tissues, including cardiotoxicity.

Ongoing failures in clinical development have highlighted the need for better preclinical models of the human cardiovascular system. In this work, we established an *in vitro* model of the human heart offering several improvements with respect to previously reported structures. In parallel, we showed successful application of a novel system for somatic gene editing in cardiac cells. Both individually and synergistically, these tools may contribute to the next generation of advanced disease modeling and therapy development.

---

## References

1. Roth, G. A. *et al.* Global Burden of Cardiovascular Diseases and Risk Factors, 1990–2019: Update From the GBD 2019 Study. *J. Am. Coll. Cardiol.* **76**, 2982 (2020).
2. Woolf, S. H. & Schoemaker, H. Life Expectancy and Mortality Rates in the United States, 1959-2017. *JAMA* **322**, 1996–2016 (2019).
3. Powell-Wiley, T. M. *et al.* Obesity and Cardiovascular Disease: A Scientific Statement From the American Heart Association. *Circulation* **143**, E984–E1010 (2021).
4. Bastien, M., Poirier, P., Lemieux, I. & Després, J. P. Overview of Epidemiology and Contribution of Obesity to Cardiovascular Disease. *Prog. Cardiovasc. Dis.* **56**, 369–381 (2014).
5. Bhatnagar, A. Environmental Determinants of Cardiovascular Disease. *Circ. Res.* **121**, 162 (2017).
6. Cosselman, K. E., Navas-Acien, A. & Kaufman, J. D. Environmental factors in cardiovascular disease. *Nat. Publ. Gr.* **12**, 627–642 (2015).
7. Kathiresan, S. & Srivastava, D. Genetics of Human Cardiovascular Disease. *Cell* **148**, 1242 (2012).
8. Gianfagna, F., Cugino, D., Santimone, I. & Iacoviello, L. From candidate gene to genome-wide association studies in cardiovascular disease. *Thromb. Res.* **129**, 320–324 (2012).
9. Olivotto, I. *et al.* Mavacamten for treatment of symptomatic obstructive hypertrophic cardiomyopathy (EXPLORER-HCM): a randomised, double-blind, placebo-controlled, phase 3 trial. *Lancet* **396**, 759–769 (2020).
10. Fordyce, C. B. *et al.* Cardiovascular Drug Development: Is it Dead or Just Hibernating? *J. Am. Coll. Cardiol.* **65**, 1567–1582 (2015).
11. Hwang, T. J. & Kesselheim, A. S. Challenges in the Development of Novel Cardiovascular Therapies. *Clin. Pharmacol. Ther.* **102**, 194–196 (2017).
12. Dowden, H. & Munro, J. Trends in clinical success rates and therapeutic focus. *Nat.*

- Rev. Drug Discov.* **18**, 495–496 (2019).
13. Hay, M., Thomas, D. W., Craighead, J. L., Economides, C. & Rosenthal, J. Clinical development success rates for investigational drugs. *Nat. Biotechnol.* **2014 321** **32**, 40–51 (2014).
  14. Pammolli, F., Magazzini, L. & Riccaboni, M. The productivity crisis in pharmaceutical R&D. *Nat. Rev. Drug Discov.* **2011 106** **10**, 428–438 (2011).
  15. Cannatà, A., Ali, H., Sinagra, G. & Giacca, M. Gene Therapy for the Heart Lessons Learned and Future Perspectives. *Circ. Res.* **126**, 1394–1414 (2020).
  16. Rosengart, T. K. *et al.* Angiogenesis gene therapy: phase I assessment of direct intramyocardial administration of an adenovirus vector expressing VEGF121 cDNA to individuals with clinically significant severe coronary artery disease. *Circulation* **100**, 468–474 (1999).
  17. Stewart, D. J. *et al.* VEGF gene therapy fails to improve perfusion of ischemic myocardium in patients with advanced coronary disease: results of the NORTHERN trial. *Mol. Ther.* **17**, 1109–1115 (2009).
  18. Hedman, M. *et al.* Safety and feasibility of catheter-based local intracoronary vascular endothelial growth factor gene transfer in the prevention of postangioplasty and in-stent restenosis and in the treatment of chronic myocardial ischemia: phase II results of the Kuopio. *Circulation* **107**, 2677–2683 (2003).
  19. Wang, D., Tai, P. W. L. & Gao, G. Adeno-associated virus vector as a platform for gene therapy delivery. *Nat. Rev. Drug Discov.* **2019 185** **18**, 358–378 (2019).
  20. Li, C. & Samulski, R. J. Engineering adeno-associated virus vectors for gene therapy. *Nat. Rev. Genet.* **2020 214** **21**, 255–272 (2020).
  21. Jessup, M. *et al.* Calcium Upregulation by Percutaneous Administration of Gene Therapy in Cardiac Disease (CUPID). *Circulation* **124**, 304–313 (2011).
  22. Kuzmin, D. A. *et al.* The clinical landscape for AAV gene therapies. *Nat. Rev. Drug Discov.* **20**, 173–174 (2021).
  23. Saga, Y. *et al.* MesP1 is expressed in the heart precursor cells and required for the formation of a single heart tube. *Development* **126**, 3437–47 (1999).

24. Saga, Y., Kitajima, S. & Miyagawa-Tomita, S. *Mesp1* expression is the earliest sign of cardiovascular development. *Trends Cardiovasc. Med.* **10**, 345–352 (2000).
25. Buckingham, M., Meilhac, S. & Zaffran, S. Building the mammalian heart from two sources of myocardial cells. *Nat. Rev. Genet.* **2005** *6*, 826–835 (2005).
26. Waldo, K. L. *et al.* Secondary heart field contributes myocardium and smooth muscle to the arterial pole of the developing heart. *Dev. Biol.* **281**, 78–90 (2005).
27. Mjaatvedt, C. H. *et al.* The outflow tract of the heart is recruited from a novel heart-forming field. *Dev. Biol.* **238**, 97–109 (2001).
28. Nahirney, P. C., Mikawa, T. & Fischman, D. A. Evidence for an extracellular matrix bridge guiding proepicardial cell migration to the myocardium of chick embryos. *Dev. Dyn.* **227**, 511–523 (2003).
29. Maya-Ramos, L., Cleland, J., Bressan, M. & Mikawa, T. Induction of the Proepicardium. *J. Dev. Biol.* **1**, 82 (2013).
30. Männer, J., Pérez-Pomares, J. M., Macías, D. & Muñoz-Chápuli, R. The origin, formation and developmental significance of the epicardium: a review. *Cells. Tissues. Organs* **169**, 89–103 (2001).
31. CB, B. & HS, B. Neural crest contribution to the cardiovascular system. *Adv. Exp. Med. Biol.* **589**, 134–154 (2006).
32. Später, D., Hansson, E. M., Zangi, L. & Chien, K. R. How to make a cardiomyocyte. *Development* **141**, 4418–4431 (2014).
33. Schultheiss, T. M., Burch, J. B. & Lassar, A. B. A role for bone morphogenetic proteins in the induction of cardiac myogenesis. *Genes Dev.* **11**, 451–462 (1997).
34. Waardenberg, A. J., Ramialison, M., Bouveret, R. & Harvey, R. P. Genetic Networks Governing Heart Development. *Cold Spring Harb. Perspect. Med.* **4**, (2014).
35. Marvin, M. J., Di Rocco, G., Gardiner, A., Bush, S. M. & Lassar, A. B. Inhibition of Wnt activity induces heart formation from posterior mesoderm. *Genes Dev.* **15**, 316–327 (2001).
36. Vincent, S. D. & Buckingham, M. E. How to make a heart: the origin and regulation of

- cardiac progenitor cells. *Curr. Top. Dev. Biol.* **90**, 1–41 (2010).
37. Moretti, A. *et al.* Multipotent embryonic isl1+ progenitor cells lead to cardiac, smooth muscle, and endothelial cell diversification. *Cell* **127**, 1151–65 (2006).
38. Kattman, S. J., Huber, T. L. & Keller, G. M. Multipotent flk-1+ cardiovascular progenitor cells give rise to the cardiomyocyte, endothelial, and vascular smooth muscle lineages. *Dev. Cell* **11**, 723–732 (2006).
39. Zhou, B., Gise, A. von, Ma, Q., Rivera-Feliciano, J. & Pu, W. T. Nkx2-5- and Isl1-expressing cardiac progenitors contribute to proepicardium. *Biochem. Biophys. Res. Commun.* **375**, 450–453 (2008).
40. Tyser, R. C. V. *et al.* Characterization of a common progenitor pool of the epicardium and myocardium. *Science (80-. )*. **371**, eabb2986 (2021).
41. Zhang, Q. *et al.* Unveiling Complexity and Multipotentiality of Early Heart Fields. *Circ. Res.* **129**, 474–487 (2021).
42. Christoffels, V. M. *et al.* Tbx18 and the fate of epicardial progenitors. *Nature* **458**, (2009).
43. Duim, S. N., Kurakula, K., Goumans, M. J. & Kruithof, B. P. Cardiac endothelial cells express Wilms' tumor-1: Wt1 expression in the developing, adult and infarcted heart. *J. Mol. Cell. Cardiol.* **81**, 127–135 (2015).
44. Schlueter, J. & Brand, T. Epicardial Progenitor Cells in Cardiac Development and Regeneration. *J. Cardiovasc. Transl. Res.* **5**, 641–653 (2012).
45. Shen, H. *et al.* Extracardiac control of embryonic cardiomyocyte proliferation and ventricular wall expansion. *Cardiovasc. Res.* **105**, 271 (2015).
46. Lavine, K. J. *et al.* Endocardial and epicardial derived FGF signals regulate myocardial proliferation and differentiation in vivo. *Dev. Cell* **8**, 85–95 (2005).
47. Groot, A. C. G., Peeters, M.-P. F. M. V., Bergwerff, M., Mentink, M. M. T. & Poelmann, R. E. Epicardial Outgrowth Inhibition Leads to Compensatory Mesothelial Outflow Tract Collar and Abnormal Cardiac Septation and Coronary Formation. *Circ. Res.* **87**, 969–971 (2000).
48. Boezio, G. L. *et al.* The developing epicardium regulates cardiac chamber

- morphogenesis by promoting cardiomyocyte growth. *bioRxiv* 2021.08.09.455639 (2021). doi:10.1101/2021.08.09.455639
49. Eralp, I. *et al.* Epicardium-derived cells are important for correct development of the Purkinje fibers in the avian heart. *Anat. Rec. A. Discov. Mol. Cell. Evol. Biol.* **288**, 1272–1280 (2006).
  50. Vega-Hernández, M., Kovacs, A., De Langhe, S. & Ornitz, D. M. FGF10/FGFR2b signaling is essential for cardiac fibroblast development and growth of the myocardium. *Development* **138**, 3331–3340 (2011).
  51. Quijada, P., Trembley, M. A. & Small, E. M. The Role of the Epicardium During Heart Development and Repair. *Circ. Res.* **126**, 377–394 (2020).
  52. Poss, K. D., Wilson, L. G. & Keating, M. T. Heart regeneration in zebrafish. *Science* **298**, 2188–90 (2002).
  53. Wang, J., Cao, J., Dickson, A. L. & Poss, K. D. Epicardial regeneration is guided by cardiac outflow tract and Hedgehog signalling. *Nature* **522**, 226–230 (2015).
  54. Kikuchi, K. *et al.* Retinoic acid production by endocardium and epicardium is an injury response essential for zebrafish heart regeneration. *Dev. Cell* **20**, 397–404 (2011).
  55. Huang, Y. *et al.* Igf Signaling is Required for Cardiomyocyte Proliferation during Zebrafish Heart Development and Regeneration. *PLoS One* **8**, (2013).
  56. Wang, J., Karra, R., Dickson, A. L. & Poss, K. D. Fibronectin is deposited by injury-activated epicardial cells and is necessary for zebrafish heart regeneration. *Dev. Biol.* **382**, 427–435 (2013).
  57. Porrello, E. R. *et al.* Transient regenerative potential of the neonatal mouse heart. *Science* **331**, 1078–80 (2011).
  58. Wijk, B. van, Gunst, Q. D., Moorman, A. F. M. & Hoff, M. J. B. van den. Cardiac Regeneration from Activated Epicardium. *PLoS One* **7**, e44692 (2012).
  59. Huang, G. N. *et al.* C/EBP transcription factors mediate epicardial activation during heart development and injury. *Science* **338**, 1599–603 (2012).
  60. Michielon, G. *et al.* Anomalous coronary artery origin from the pulmonary artery:

- correlation between surgical timing and left ventricular function recovery. *Ann. Thorac. Surg.* **76**, 581–588 (2003).
61. Mollova, M. *et al.* Cardiomyocyte proliferation contributes to heart growth in young humans. *Proc. Natl. Acad. Sci. U. S. A.* **110**, 1446–51 (2013).
  62. Milani-Nejad, N. & Janssen, P. M. L. Small and large animal models in cardiac contraction research: advantages and disadvantages. *Pharmacol. Ther.* **141**, 235–49 (2014).
  63. Thomson, J. A. *et al.* Embryonic stem cell lines derived from human blastocysts. *Science* **282**, 1145–1147 (1998).
  64. Holden, C. & Kaiser, J. Draft stem cell guidelines please many, disappoint some. *Science* (80-. ). **324**, 446 (2009).
  65. Siegel, A. W. Temporal restrictions and the impasse on human embryonic stem-cell research. *Lancet (London, England)* **364**, 215–218 (2004).
  66. Takahashi, K. & Yamanaka, S. Induction of pluripotent stem cells from mouse embryonic and adult fibroblast cultures by defined factors. *Cell* **126**, 663–76 (2006).
  67. Takahashi, K. *et al.* Induction of pluripotent stem cells from adult human fibroblasts by defined factors. *Cell* **131**, 861–72 (2007).
  68. Yu, J. *et al.* Induced pluripotent stem cell lines derived from human somatic cells. *Science* (80-. ). **318**, 1917–1920 (2007).
  69. Omole, A. E. & Fakoya, A. O. J. Ten years of progress and promise of induced pluripotent stem cells: historical origins, characteristics, mechanisms, limitations, and potential applications. *PeerJ* **6**, 4370 (2018).
  70. Loh, Y.-H. *et al.* Generation of induced pluripotent stem cells from human blood. *Blood* **113**, 5476 (2009).
  71. Mandai, M. *et al.* Autologous Induced Stem-Cell-Derived Retinal Cells for Macular Degeneration. *N. Engl. J. Med.* **376**, 1038–1046 (2017).
  72. Deinsberger, J., Reisinger, D. & Weber, B. Global trends in clinical trials involving pluripotent stem cells: a systematic multi-database analysis. *npj Regen. Med.* **5**, 1–13 (2020).

- 
73. Yamanaka, S. Pluripotent Stem Cell-Based Cell Therapy—Promise and Challenges. *Cell Stem Cell* **27**, 523–531 (2020).
  74. De Sousa, P. A. *et al.* Rapid establishment of the European Bank for induced Pluripotent Stem Cells (EBiSC) - the Hot Start experience. *Stem Cell Res.* **20**, 105–114 (2017).
  75. Streeter, I. *et al.* The human-induced pluripotent stem cell initiative—data resources for cellular genetics. *Nucleic Acids Res.* **45**, D691 (2017).
  76. Disease-specific iPSC cells | Cell Engineering Division -CELL BANK- (RIKEN BRC). Available at: [https://cell.brc.riken.jp/en/hps/patient\\_specific\\_ips](https://cell.brc.riken.jp/en/hps/patient_specific_ips). (Accessed: 18th September 2021)
  77. WiCell. Available at: <https://www.wicell.org/>. (Accessed: 18th September 2021)
  78. Huang, C.-Y. *et al.* Human iPSC banking: barriers and opportunities. *J. Biomed. Sci.* 2019 **261** **26**, 1–14 (2019).
  79. Bellin, M. Induced pluripotent stem cells: the new patient? *Nat. Rev. Mol. Cell Biol.* **13**, (2012).
  80. Lee, G. *et al.* Large-scale screening using familial dysautonomia induced pluripotent stem cells identifies compounds that rescue IKBKAP expression. *Nat. Biotechnol.* **30**, 1244–1248 (2012).
  81. McNeish, J., Gardner, J. P., Wainger, B. J., Woolf, C. J. & Eggan, K. From Dish to Bedside: Lessons Learned While Translating Findings from a Stem Cell Model of Disease to a Clinical Trial. *Cell Stem Cell* **17**, 8–10 (2015).
  82. Wainger, B. J. *et al.* Effect of Ezogabine on Cortical and Spinal Motor Neuron Excitability in Amyotrophic Lateral Sclerosis: A Randomized Clinical Trial. *JAMA Neurol.* **78**, 186–196 (2021).
  83. Perrin, S. Preclinical research: Make mouse studies work. *Nat.* 2014 **5077493** **507**, 423–425 (2014).
  84. Burridge, P. W. *et al.* Chemically defined generation of human cardiomyocytes. *Nat. Methods* **11**, 855–60 (2014).
  85. Bao, X. *et al.* Directed differentiation and long-term maintenance of epicardial cells

- derived from human pluripotent stem cells under fully defined conditions. *Nat. Protoc.* **12**, 1890–1900 (2017).
86. Witty, A. D. *et al.* Generation of the epicardial lineage from human pluripotent stem cells. *Nat. Biotechnol.* **32**, 1026–1035 (2014).
87. Giacomelli, E. *et al.* Three-dimensional cardiac microtissues composed of cardiomyocytes and endothelial cells co-differentiated from human pluripotent stem cells. *Dev.* **144**, 1008–1017 (2017).
88. Bao, X. *et al.* Human pluripotent stem cell-derived epicardial progenitors can differentiate to endocardial-like endothelial cells. *Bioeng. Transl. Med.* **2**, 191–201 (2017).
89. Moretti, A. *et al.* Patient-specific induced pluripotent stem-cell models for long-QT syndrome. *N. Engl. J. Med.* **363**, 1397–1409 (2010).
90. Yazawa, M. *et al.* Using induced pluripotent stem cells to investigate cardiac phenotypes in Timothy syndrome. *Nature* **471**, 230–4 (2011).
91. Schweitzer, M. K. *et al.* Suppression of Arrhythmia by Enhancing Mitochondrial Ca<sup>2+</sup> Uptake in Catecholaminergic Ventricular Tachycardia Models. *JACC. Basic to Transl. Sci.* **2**, 737–747 (2017).
92. Fatima, A. *et al.* In vitro modeling of ryanodine receptor 2 dysfunction using human induced pluripotent stem cells. *Cell. Physiol. Biochem.* **28**, 579–92 (2011).
93. Lan, F. *et al.* Abnormal calcium handling properties underlie familial hypertrophic cardiomyopathy pathology in patient-specific induced pluripotent stem cells. *Cell Stem Cell* **12**, 101–13 (2013).
94. Cohn, R. *et al.* A Contraction Stress Model of Hypertrophic Cardiomyopathy due to Sarcomere Mutations. *Stem Cell Reports* **12**, 71–83 (2019).
95. Sun, N. *et al.* Patient-Specific Induced Pluripotent Stem Cell as a Model for Familial Dilated Cardiomyopathy. *Sci. Transl. Med.* **4**, 130ra47 (2012).
96. Schick, R. *et al.* Functional abnormalities in induced Pluripotent Stem Cell-derived cardiomyocytes generated from titin-mutated patients with dilated cardiomyopathy. *PLoS One* **13**, e0205719 (2018).

97. Jaffré, F. *et al.* iPSC-Derived Cardiomyocytes Reveal Aberrant ERK5 and MEK1/2 Signaling Concomitantly Promote Hypertrophic Cardiomyopathy in RAF1-Associated Noonan Syndrome. *Circulation* **140**, 207–224 (2019).
98. Miao, Y. *et al.* Intrinsic Endocardial Defects Contribute to Hypoplastic Left Heart Syndrome. *Cell Stem Cell* **27**, 574–589.e8 (2020).
99. Marchiano, S. *et al.* SARS-CoV-2 Infects Human Pluripotent Stem Cell-Derived Cardiomyocytes, Impairing Electrical and Mechanical Function. *Stem Cell Reports* **16**, 478–492 (2021).
100. Yang, L. *et al.* A Human Pluripotent Stem Cell-based Platform to Study SARS-CoV-2 Tropism and Model Virus Infection in Human Cells and Organoids. *Cell Stem Cell* **27**, 125–136 (2020).
101. Simian, M. & Bissell, M. J. Organoids: A historical perspective of thinking in three dimensions. *J. Cell Biol.* **216**, 31–40 (2017).
102. Tung, T.-C. & Kü, S.-H. Experimental studies on the development of the pronephric duct in anuran embryos. *J. Anat.* **78**, 52 (1944).
103. Weiss, P. & Taylor, A. C. Reconstitution of complete organs from single-cell suspensions of chick embryos in advanced stages of differentiation. *Proc. Natl. Acad. Sci. U. S. A.* **46**, 1177 (1960).
104. Li, M. L. *et al.* Influence of a reconstituted basement membrane and its components on casein gene expression and secretion in mouse mammary epithelial cells. *Proc. Natl. Acad. Sci. U. S. A.* **84**, 136 (1987).
105. Zimmermann, W. H. *et al.* Tissue engineering of a differentiated cardiac muscle construct. *Circ. Res.* **90**, 223–230 (2002).
106. Black, L. D., Meyers, J. D., Weinbaum, J. S., Shvelidze, Y. A. & Tranquillo, R. T. Cell-induced alignment augments twitch force in fibrin gel-based engineered myocardium via gap junction modification. *Tissue Eng. Part A* **15**, 3099–3108 (2009).
107. de Lange, W. J. *et al.* Neonatal mouse-derived engineered cardiac tissue: a novel model system for studying genetic heart disease. *Circ. Res.* **109**, 8–16 (2011).
108. Hansen, A. *et al.* Development of a Drug Screening Platform Based on Engineered

- Heart Tissue. *Circ. Res.* **107**, 35–44 (2010).
109. Hirt, M. N., Hansen, A. & Eschenhagen, T. Cardiac tissue engineering : State of the art. *Circ. Res.* **114**, 354–367 (2014).
110. Sun, X. & Nunes, S. S. Bioengineering Approaches to Mature Human Pluripotent Stem Cell-Derived Cardiomyocytes. *Front. Cell Dev. Biol.* **5**, 19 (2017).
111. Wanjare, M. & Huang, N. F. Regulation of the microenvironment for cardiac tissue engineering. *Regen. Med.* **12**, 187–201 (2017).
112. Nguyen, A. H. *et al.* Cardiac tissue engineering: state-of-the-art methods and outlook. *J. Biol. Eng. 2019 131* **13**, 1–21 (2019).
113. Atmanli, A. & Domian, I. J. Recreating the Cardiac Microenvironment in Pluripotent Stem Cell Models of Human Physiology and Disease. *Trends Cell Biol.* **27**, 352–364 (2017).
114. Clevers, H. Modeling Development and Disease with Organoids. *Cell* **165**, 1586–1597 (2016).
115. Sato, T. *et al.* Single Lgr5 stem cells build crypt–villus structures in vitro without a mesenchymal niche. *Nature* **459**, 262–265 (2009).
116. Lancaster, M. A. *et al.* Cerebral organoids model human brain development and microcephaly. *Nature* **501**, 373–379 (2013).
117. Takasato, M. *et al.* Kidney organoids from human iPS cells contain multiple lineages and model human nephrogenesis. *Nature* **526**, 564–568 (2015).
118. Wang, D. *et al.* Long-Term Expansion of Pancreatic Islet Organoids from Resident Procr+ Progenitors. *Cell* **180**, 1198-1211.e19 (2020).
119. Kim, J., Koo, B.-K. & Knoblich, J. A. Human organoids: model systems for human biology and medicine. *Nat. Rev. Mol. Cell Biol.* **21**, 571–584 (2020).
120. Drakhlis, L. *et al.* Human heart-forming organoids recapitulate early heart and foregut development. *Nat. Biotechnol. 2021 396* **39**, 737–746 (2021).
121. Hofbauer, P. *et al.* Cardioids reveal self-organizing principles of human cardiogenesis. *Cell* **184**, 3299-3317.e22 (2021).

122. Lewis-Israeli, Y. R. *et al.* Self-assembling human heart organoids for the modeling of cardiac development and congenital heart disease. *Nat. Commun.* **12**, 5142 (2021).
123. Brown, N. H. Extracellular Matrix in Development: Insights from Mechanisms Conserved between Invertebrates and Vertebrates. *Cold Spring Harb. Perspect. Biol.* **3**, a005082 (2011).
124. Gjorevski, N. *et al.* Designer matrices for intestinal stem cell and organoid culture. *Nat. Publ. Gr.* **539**, (2016).
125. Lou, Y.-R. & Leung, A. W. Next generation organoids for biomedical research and applications. *Biotechnol. Adv.* **36**, 132–149 (2018).
126. Freedman, B. S. *et al.* Modelling kidney disease with CRISPR-mutant kidney organoids derived from human pluripotent epiblast spheroids. *Nat. Commun.* **6**, (2015).
127. Berkers, G. *et al.* Rectal Organoids Enable Personalized Treatment of Cystic Fibrosis. *CellReports* **26**, 1701-1708.e3 (2019).
128. Dekkers, J. F. *et al.* A functional CFTR assay using primary cystic fibrosis intestinal organoids. *Nat. Med.* **19**, 939–945 (2013).
129. Dossena, M. *et al.* Standardized GMP-compliant scalable production of human pancreas organoids. *Stem Cell Res. Ther.* 2020 111 **11**, 1–12 (2020).
130. Jinek, M. *et al.* A programmable dual-RNA-guided DNA endonuclease in adaptive bacterial immunity. *Science* **337**, 816–21 (2012).
131. Khan, S. H. Genome-Editing Technologies: Concept, Pros, and Cons of Various Genome-Editing Techniques and Bioethical Concerns for Clinical Application. *Mol. Ther. - Nucleic Acids* **16**, 326–334 (2019).
132. Uddin, F., Rudin, C. M. & Sen, T. CRISPR Gene Therapy: Applications, Limitations, and Implications for the Future. *Front. Oncol.* **10**, 1387 (2020).
133. Ran, F. A. *et al.* Genome engineering using the CRISPR-Cas9 system. *Nat. Protoc.* **8**, 2281–308 (2013).
134. Lin, S., Staahl, B. T., Alla, R. K. & Doudna, J. A. Enhanced homology-directed human genome engineering by controlled timing of CRISPR/Cas9 delivery. *Elife* **3**, e04766

- (2014).
135. Stazio, M. Di, Foschi, N., Athanasakis, E., Gasparini, P. & d'Adamo, A. P. Systematic analysis of factors that improve homologous direct repair (HDR) efficiency in CRISPR/Cas9 technique. *PLoS One* **16**, (2021).
  136. Shen, B. *et al.* Efficient genome modification by CRISPR-Cas9 nickase with minimal off-target effects. *Nat. Methods* **11**, 399–402 (2014).
  137. Cho, S. W. *et al.* Analysis of off-target effects of CRISPR/Cas-derived RNA-guided endonucleases and nickases. *Genome Res.* **24**, 132 (2014).
  138. Porto, E. M., Komor, A. C., Slaymaker, I. M. & Yeo, G. W. Base editing: advances and therapeutic opportunities. *Nat. Rev. Drug Discov.* 2020 1912 **19**, 839–859 (2020).
  139. Komor, A. C., Kim, Y. B., Packer, M. S., Zuris, J. A. & Liu, D. R. Programmable editing of a target base in genomic DNA without double-stranded DNA cleavage. *Nature* **533**, 420–424 (2016).
  140. Anzalone, A. V. *et al.* Search-and-replace genome editing without double-strand breaks or donor DNA. *Nature* **576**, 149–157 (2019).
  141. Niemitz, E. Isogenic iPSC-derived models of disease. *Nat. Genet.* 2014 461 **46**, 7–7 (2013).
  142. Grobarczyk, B., Franco, B., Hanon, K. & Malgrange, B. Generation of Isogenic Human iPS Cell Line Precisely Corrected by Genome Editing Using the CRISPR/Cas9 System. *Stem Cell Rev. Reports* **11**, 774–787 (2015).
  143. Ruan, J. *et al.* Highly efficient CRISPR/Cas9-mediated transgene knockin at the H11 locus in pigs. *Sci. Rep.* **5**, 14253 (2015).
  144. Papapetrou, E. P. & Schambach, A. Gene Insertion Into Genomic Safe Harbors for Human Gene Therapy. *Mol. Ther.* **24**, 678–84 (2016).
  145. Depla, J. A. *et al.* Cerebral Organoids: A Human Model for AAV Capsid Selection and Therapeutic Transgene Efficacy in the Brain. *Mol. Ther. - Methods Clin. Dev.* **18**, 167–175 (2020).
  146. Meyer-Berg, H. *et al.* Identification of AAV serotypes for lung gene therapy in human

- embryonic stem cell-derived lung organoids. *Stem Cell Res. Ther.* **11**, (2020).
147. Mendjan, S. *et al.* NANOG and CDX2 pattern distinct subtypes of human mesoderm during exit from pluripotency. *Cell Stem Cell* **15**, 310–325 (2014).
  148. Bao, X. *et al.* Human pluripotent stem cell-derived epicardial progenitors can differentiate to endocardial-like endothelial cells. *Bioeng. Transl. Med.* **2**, 191–201 (2017).
  149. Moretti, A. *et al.* Somatic gene editing ameliorates skeletal and cardiac muscle failure in pig and human models of Duchenne muscular dystrophy. *Nat. Med.* **26**, 206–214 (2020).
  150. Fischer, B. *et al.* A complete workflow for the differentiation and the dissociation of hiPSC-derived cardiospheres. *Stem Cell Res.* **32**, 65–72 (2018).
  151. Efremova, M., Vento-Tormo, M., Teichmann, S. A. & Vento-Tormo, R. CellPhoneDB: inferring cell–cell communication from combined expression of multi-subunit ligand–receptor complexes. *Nat. Protoc.* **2020 154** **15**, 1484–1506 (2020).
  152. RStudio Team (2020). Integrated Development for R. RStudio, PBC, Boston, MA <http://www.rstudio.com/>.
  153. Coupé, P., Munz, M., Manjón, J. V, Ruthazer, E. S. & Collins, D. L. A CANDLER for a deeper in vivo insight. *Med. Image Anal.* **16**, 849 (2012).
  154. Niederreither, K. *et al.* Embryonic retinoic acid synthesis is essential for heart morphogenesis in the mouse. *Development* **128**, 1019–1031 (2001).
  155. Hochgreb, T. *et al.* A caudorostral wave of RALDH2 conveys anteroposterior information to the cardiac field. *Development* **130**, 5363–5374 (2003).
  156. Sirbu, I. O., Zhao, X. & Duester, G. Retinoic Acid Controls Heart Anteroposterior Patterning by Downregulating *Isl1* through the *Fgf8* Pathway. *Dev. Dyn.* **237**, 1627 (2008).
  157. De Bono, C. *et al.* T-box genes and retinoic acid signaling regulate the segregation of arterial and venous pole progenitor cells in the murine second heart field. *Hum. Mol. Genet.* **27**, 3747–3760 (2018).
  158. Bernheim, S. & Meilhac, S. M. Mesoderm patterning by a dynamic gradient of retinoic acid signalling. *Philos. Trans. R. Soc. B* **375**, 20190556 (2020).

159. Frangogiannis, N. G. The extracellular matrix in myocardial injury, repair, and remodeling. *J. Clin. Invest.* **127**, 1600–1612 (2017).
160. Risebro, C. A., Vieira, J. M., Klotz, L. & Riley, P. R. Characterisation of the human embryonic and foetal epicardium during heart development. *Development* **142**, 3630–6 (2015).
161. Tyser, R. *et al.* A spatially resolved single cell atlas of human gastrulation. *bioRxiv* 2020.07.21.213512 (2020). doi:10.1101/2020.07.21.213512
162. Ma, Q., Zhou, B. & Pu, W. T. Reassessment of Isl1 and Nkx2-5 cardiac fate maps using a Gata4-based reporter of Cre activity. *Dev. Biol.* **323**, 98–104 (2008).
163. Zhou, B., von Gise, A., Ma, Q., Rivera-Feliciano, J. & Pu, W. T. Nkx2-5- and Isl1-expressing cardiac progenitors contribute to proepicardium. *Biochem. Biophys. Res. Commun.* **375**, 450–3 (2008).
164. Nakano, A., Nakano, H. & Chien, K. R. Multipotent Islet-1 cardiovascular progenitors in development and disease. *Cold Spring Harb. Symp. Quant. Biol.* **73**, 297–306 (2008).
165. Zhou, B., von Gise, A., Ma, Q., Rivera-Feliciano, J. & Pu, W. T. Nkx2-5- and Isl1-expressing cardiac progenitors contribute to proepicardium. *Biochem. Biophys. Res. Commun.* **375**, 450–3 (2008).
166. Shen, H. *et al.* Extracardiac control of embryonic cardiomyocyte proliferation and ventricular wall expansion. *Cardiovasc. Res.* **105**, 271–8 (2015).
167. Scholzen, T. & Gerdes, J. The Ki-67 protein: From the known and the unknown. *J. Cell. Physiol.* **182**, 311–322 (2000).
168. Antzelevitch, C. Cardiac repolarization. The long and short of it. *Europace* **7**, 3 (2005).
169. Goedel, A. *et al.* Subtype-specific optical action potential recordings in human induced pluripotent stem cell-derived ventricular cardiomyocytes. *J. Vis. Exp.* **2018**, (2018).
170. Becht, E. *et al.* Dimensionality reduction for visualizing single-cell data using UMAP. *Nat. Biotechnol.* **2018 371** **37**, 38–44 (2018).
171. Asp, M. *et al.* A Spatiotemporal Organ-Wide Gene Expression and Cell Atlas of the Developing Human Heart. *Cell* **179**, 1647-1660.e19 (2019).

- 
172. Cui, Y. *et al.* Single-Cell Transcriptome Analysis Maps the Developmental Track of the Human Heart. *Cell Rep.* **26**, 1934–1950.e5 (2019).
173. Funakoshi, S. *et al.* Generation of mature compact ventricular cardiomyocytes from human pluripotent stem cells. *Nat. Commun.* **2021 121** **12**, 1–23 (2021).
174. Bedada, F. B. *et al.* Acquisition of a Quantitative, Stoichiometrically Conserved Ratiometric Marker of Maturation Status in Stem Cell-Derived Cardiac Myocytes. *Stem Cell Reports* **3**, 594–605 (2014).
175. Sedmera, D. *et al.* Spatiotemporal pattern of commitment to slowed proliferation in the embryonic mouse heart indicates progressive differentiation of the cardiac conduction system. *Anat. Rec. A. Discov. Mol. Cell. Evol. Biol.* **274**, 773–777 (2003).
176. Soysa, T. Y. de *et al.* Single-cell analysis of cardiogenesis reveals basis for organ level developmental defects. *Nature* **572**, 120 (2019).
177. Facucho-Oliveira, J., M. B. & JA, B. Ccbe1 expression marks the cardiac and lymphatic progenitor lineages during early stages of mouse development. *Int. J. Dev. Biol.* **55**, 1007–1014 (2011).
178. Li, P. *et al.* IGF signaling directs ventricular cardiomyocyte proliferation during embryonic heart development. *Development* **138**, 1795–1805 (2011).
179. Dronkers, E., Wauters, M. M. M., Goumans, M. J. & Smits, A. M. Epicardial TGF $\beta$  and BMP Signaling in Cardiac Regeneration: What Lesson Can We Learn from the Developing Heart? *Biomolecules* **10**, (2020).
180. Ieda, M. *et al.* Cardiac Fibroblasts Regulate Myocardial Proliferation through  $\beta$ 1 Integrin Signaling. *Dev. Cell* **16**, 233 (2009).
181. Artham, S. M. *et al.* Clinical impact of left ventricular hypertrophy and implications for regression. *Prog. Cardiovasc. Dis.* **52**, 153–167 (2009).
182. Meijis, M. F. *et al.* A prediction model for left ventricular mass in patients at high cardiovascular risk. *Eur. J. Cardiovasc. Prev. Rehabil.* **17**, 621–627 (2010).
183. Földes, G. *et al.* Modulation of human embryonic stem cell-derived cardiomyocyte growth: A testbed for studying human cardiac hypertrophy? *J. Mol. Cell. Cardiol.* **50**, 367 (2011).

184. Deisl, C., Fine, M., Moe, O. W. & Hilgemann, D. W. Hypertrophy of human embryonic stem cell–derived cardiomyocytes supported by positive feedback between Ca<sup>2+</sup> and diacylglycerol signals. *Pflügers Arch. - Eur. J. Physiol.* 2019 4718 **471**, 1143–1157 (2019).
185. Johansson, M. *et al.* Cardiac hypertrophy in a dish: a human stem cell based model. *Biol. Open* **9**, (2020).
186. Archer, C. R., Robinson, E. L., Drawnel, F. M. & Roderick, H. L. Endothelin-1 promotes hypertrophic remodelling of cardiac myocytes by activating sustained signalling and transcription downstream of endothelin type A receptors. *Cell. Signal.* **36**, 240 (2017).
187. Adiarto, S. *et al.* ET-1 from endothelial cells is required for complete angiotensin II-induced cardiac fibrosis and hypertrophy. *Life Sci.* **91**, 651–657 (2012).
188. Sun, X. *et al.* The extracellular matrix protein agrin is essential for epicardial epithelial-to-mesenchymal transition during heart development. *Development* **148**, (2021).
189. Gillmore, J. D. *et al.* CRISPR-Cas9 In Vivo Gene Editing for Transthyretin Amyloidosis. *N. Engl. J. Med.* **385**, 493–502 (2021).
190. Gopal, S., Rodrigues, A. L. & Dordick, J. S. Exploiting CRISPR Cas9 in Three-Dimensional Stem Cell Cultures to Model Disease. *Frontiers in Bioengineering and Biotechnology* **8**, 692 (2020).
191. Masi, C. De, Spitalieri, P., Murdocca, M., Novelli, G. & Sangiuolo, F. Application of CRISPR/Cas9 to human-induced pluripotent stem cells: from gene editing to drug discovery. *Hum. Genomics* 2020 141 **14**, 1–12 (2020).
192. Truong, D. J. *et al.* Development of an intein-mediated split-Cas9 system for gene therapy. *Nucleic Acids Res.* **43**, 6450–6458 (2015).
193. Eschenhagen, T. & Zimmermann, W. H. Engineering myocardial tissue. *Circ. Res.* **97**, 1220–31 (2005).
194. Horvath, P. *et al.* Screening out irrelevant cell-based models of disease. *Nat. Rev. Drug Discov.* **15**, 751–769 (2016).
195. Breslin, S. & O’Driscoll, L. Three-dimensional cell culture: the missing link in drug discovery. *Drug Discov. Today* **18**, 240–9 (2013).

- 
196. Günter, J. *et al.* Microtissues in Cardiovascular Medicine: Regenerative Potential Based on a 3D Microenvironment. *Stem Cells Int.* **2016**, 9098523 (2016).
  197. Fatehullah, A., Hui Tan, S. & Barker, N. Organoids as an in vitro model of human development and disease. *Nat. Cell Biol.* **18**, 246–254 (2016).
  198. Stefanovic, S. & Zaffran, S. Mechanisms of retinoic acid signaling during cardiogenesis. *Mech. Dev.* **143**, 9–19 (2017).
  199. Jenkins, K. J. *et al.* Noninherited Risk Factors and Congenital Cardiovascular Defects: Current Knowledge. *Circulation* **115**, 2995–3014 (2007).
  200. Iyer, D. *et al.* Robust derivation of epicardium and its differentiated smooth muscle cell progeny from human pluripotent stem cells. | *Dev.* **143**, (2016).
  201. Zhao, J. *et al.* Efficient Differentiation of TBX18+/WT1+ Epicardial-Like Cells from Human Pluripotent Stem Cells Using Small Molecular Compounds. *Stem Cells Dev.* **26**, 528–540 (2017).
  202. Ferrai, C. *et al.* Induction of HoxB Transcription by Retinoic Acid Requires Actin Polymerization. *Mol. Biol. Cell* **20**, 3543 (2009).
  203. Brade, T., Pane, L. S., Moretti, A., Chien, K. R. & Laugwitz, K.-L. Embryonic Heart Progenitors and Cardiogenesis. *Cold Spring Harb. Perspect. Med.* **3**, (2013).
  204. Rossi, G. *et al.* Capturing Cardiogenesis in Gastruloids. *Cell Stem Cell* **28**, 230-240.e6 (2021).
  205. Andersen, P. *et al.* Precardiac organoids form two heart fields via Bmp/Wnt signaling. *Nat. Commun.* **9**, 3140 (2018).
  206. Lee, J. *et al.* In vitro generation of functional murine heart organoids via FGF4 and extracellular matrix. *Nat. Commun.* **11**, 4283 (2020).
  207. Smits, A. M. & Riley, P. R. Epicardium-Derived Heart Repair. *J. Dev. Biol.* **2**, 84 (2014).
  208. Tuyn, J. van *et al.* Epicardial Cells of Human Adults Can Undergo an Epithelial-to-Mesenchymal Transition and Obtain Characteristics of Smooth Muscle Cells In Vitro. *Stem Cells* **25**, 271–278 (2007).
  209. Iyer, D. *et al.* Robust derivation of epicardium and its differentiated smooth muscle cell

- progeny from human pluripotent stem cells. *Development* **142**, 1528–41 (2015).
210. Guadix, J. A. *et al.* Human Pluripotent Stem Cell Differentiation into Functional Epicardial Progenitor Cells. *Stem Cell Reports* **9**, 1754–1764 (2017).
211. Witty, A. D. *et al.* Generation of the epicardial lineage from human pluripotent stem cells. *Nat. Biotechnol.* **32**, 1026–1035 (2014).
212. Acharya, A. *et al.* The bHLH transcription factor Tcf21 is required for lineage-specific EMT of cardiac fibroblast progenitors. *Development* **139**, 2139–49 (2012).
213. Katz, T. C. *et al.* Distinct Compartments of the Proepicardial Organ Give Rise to Coronary Vascular Endothelial Cells. *Dev. Cell* **22**, 639–650 (2012).
214. Weinberger, M., Simões, F. C., Patient, R., Sauka-Spengler, T. & Riley, P. R. Functional Heterogeneity within the Developing Zebrafish Epicardium. *Dev. Cell* **52**, 574-590.e6 (2020).
215. Gambardella, L. *et al.* BNC1 regulates cell heterogeneity in human pluripotent stem cell-derived epicardium. *Development* **146**, dev174441 (2019).
216. Lupu, I.-E., Redpath, A. N. & Smart, N. Spatiotemporal Analysis Reveals Overlap of Key Proepicardial Markers in the Developing Murine Heart. *Stem Cell Reports* **14**, 770–787 (2020).
217. Buenrostro, J., Wu, B., Chang, H. & Greenleaf, W. ATAC-seq: A Method for Assaying Chromatin Accessibility Genome-Wide. *Curr. Protoc. Mol. Biol.* **109**, 21.29.1 (2015).
218. Ranzoni, A. M., Tangherloni, A., Berest, I., Mohorianu, I. & Zaugg, J. B. Integrative Single-Cell RNA-Seq and ATAC-Seq Analysis of Human Developmental Hematopoiesis. *Stem Cell* **28**, 472-487.e7 (2021).
219. Ziffra, R. S. *et al.* Single cell epigenomic atlas of the developing human brain and organoids. *bioRxiv* 2019.12.30.891549 (2019). doi:10.1101/2019.12.30.891549
220. Parrotta, E. I., Lucchino, V., Scaramuzzino, L., Scalise, S. & Cuda, G. Modeling cardiac disease mechanisms using induced pluripotent stem cell-derived cardiomyocytes: Progress, promises and challenges. *International Journal of Molecular Sciences* **21**, 1–30 (2020).

- 
221. Denning, C. *et al.* Cardiomyocytes from human pluripotent stem cells: From laboratory curiosity to industrial biomedical platform. *Biochim. Biophys. Acta - Mol. Cell Res.* **1863**, 1728–1748 (2016).
222. Priori, S. G., Napolitano, C., Di Pasquale, E. & Condorelli, G. Induced pluripotent stem cell-derived cardiomyocytes in studies of inherited arrhythmias. *J. Clin. Invest.* **123**, 84–91 (2013).
223. Burnett, S. D., Blanchette, A. D., Chiu, W. A. & Rusyn, I. Human induced pluripotent stem cell (iPSC)-derived cardiomyocytes as an in vitro model in toxicology: strengths and weaknesses for hazard identification and risk characterization. *Expert Opin. Drug Metab. Toxicol.* **17**, 887–902 (2021).
224. Fujiu, K. & Nagai, R. Fibroblast-mediated pathways in cardiac hypertrophy. *J. Mol. Cell. Cardiol.* **70**, 64–73 (2014).
225. Hirt, M. N. *et al.* Increased afterload induces pathological cardiac hypertrophy: A new in vitro model. *Basic Res. Cardiol.* **107**, 1–16 (2012).
226. Redpath, A. N. & Smart, N. Recapturing embryonic potential in the adult epicardium: Prospects for cardiac repair. *Stem Cells Transl. Med.* **10**, 511–521 (2021).
227. Schneider, C. *et al.* Primate heart regeneration via migration and fibroblast repulsion by human heart progenitors. *bioRxiv* 2020.07.03.183798 (2020). doi:10.1101/2020.07.03.183798
228. Fang, M., Xiang, F. L., Braitsch, C. M. & Yutzey, K. E. Epicardium-derived fibroblasts in heart development and disease. *J. Mol. Cell. Cardiol.* **91**, 23–27 (2016).
229. Marin, T. M. *et al.* Rapamycin reverses hypertrophic cardiomyopathy in a mouse model of LEOPARD syndrome-associated PTPN11 mutation. *J. Clin. Invest.* **121**, 1026–43 (2011).
230. Wang, J. *et al.* In vivo efficacy of the AKT inhibitor ARQ 092 in Noonan Syndrome with Multiple Lentigines-associated hypertrophic cardiomyopathy. *PLoS One* **12**, e0178905 (2017).
231. Hahn, A. *et al.* Rapidly progressive hypertrophic cardiomyopathy in an infant with Noonan syndrome with multiple lentigines: Palliative treatment with a rapamycin

- analog. *Am. J. Med. Genet. Part A* **167**, 744–751 (2015).
232. Andelfinger, G. *et al.* Hypertrophic Cardiomyopathy in Noonan syndrome treated by MEK-inhibition. *J Am Coll Cardiol.* **73**, 2237–2239 (2019).
233. Wang, Y. *et al.* iTALK: an R Package to Characterize and Illustrate Intercellular Communication. *bioRxiv* 507871 (2019). doi:10.1101/507871
234. Armingol, E., Officer, A., Harismendy, O. & Lewis, N. E. Deciphering cell–cell interactions and communication from gene expression. *Nat. Rev. Genet.* **2020** *222* **22**, 71–88 (2020).
235. Rios, A. C. & Clevers, H. Imaging organoids: a bright future ahead. *Nat. Publ. Gr.* **15**, (2018).
236. Ferri, N. *et al.* Drug attrition during pre-clinical and clinical development: Understanding and managing drug-induced cardiotoxicity. *Pharmacol. Ther.* **138**, 470–484 (2013).
237. Mamoshina, P., Rodriguez, B. & Bueno-Orovio, A. Toward a broader view of mechanisms of drug cardiotoxicity. *Cell Reports Med.* **2**, 100216 (2021).
238. Caipa Garcia, A. L., Arlt, V. M. & Phillips, D. H. Organoids for toxicology and genetic toxicology: applications with drugs and prospects for environmental carcinogenesis. *Mutagenesis* **XX**, 1–12 (2021).
239. Renner, H. *et al.* Cell-Type-Specific High Throughput Toxicity Testing in Human Midbrain Organoids. *Front. Mol. Neurosci.* **14**, 149 (2021).
240. Dominguez, A. A., Lim, W. A. & Qi, L. S. Beyond editing: repurposing CRISPR-Cas9 for precision genome regulation and interrogation. *Nat. Rev. Mol. Cell Biol.* **17**, 5–15 (2015).
241. Haccin-Bey-Abina, S. *et al.* LMO2-associated clonal T cell proliferation in two patients after gene therapy for SCID-X1. *Science* **302**, 415–419 (2003).
242. Fu, Y. *et al.* High-frequency off-target mutagenesis induced by CRISPR-Cas nucleases in human cells. *Nat. Biotechnol.* **31**, 822–6 (2013).
243. Achberger, K. *et al.* Human stem cell-based retina on chip as new translational model

- for validation of AAV retinal gene therapy vectors. *Stem Cell Reports* **16**, 2242–2256 (2021).
244. Xu, X. *et al.* Engineered miniature CRISPR-Cas system for mammalian genome regulation and editing. *Mol. Cell* (2021). doi:10.1016/j.molcel.2021.08.008
245. Kim, D. Y. *et al.* Efficient CRISPR editing with a hypercompact Cas12f1 and engineered guide RNAs delivered by adeno-associated virus. *Nat. Biotechnol.* 1–9 (2021). doi:10.1038/s41587-021-01009-z
246. Zhang, D. *et al.* In vitro induction and in vivo engraftment of kidney organoids derived from human pluripotent stem cells. *Exp. Ther. Med.* **20**, 1307 (2020).
247. Daviaud, N., Friedel, R. H. & Zou, H. Vascularization and Engraftment of Transplanted Human Cerebral Organoids in Mouse Cortex. *eNeuro* **5**, (2018).
248. Litviňuková, M. *et al.* Cells of the adult human heart. *Nat.* 2020 5887838 **588**, 466–472 (2020).
249. van den Berg, C. W. *et al.* Renal Subcapsular Transplantation of PSC-Derived Kidney Organoids Induces Neo-vasculogenesis and Significant Glomerular and Tubular Maturation In Vivo. *Stem cell reports* **10**, 751–765 (2018).
250. Mansour, A. A. *et al.* An in vivo model of functional and vascularized human brain organoids. *Nat. Biotechnol.* 2018 365 **36**, 432–441 (2018).
251. Grebenyuk, S. & Ranga, A. Engineering organoid vascularization. *Frontiers in Bioengineering and Biotechnology* **7**, 39 (2019).
252. Chen, A., Guo, Z., Fang, L. & Bian, S. Application of Fused Organoid Models to Study Human Brain Development and Neural Disorders. *Front. Cell. Neurosci.* **14**, 133 (2020).
253. Xiang, Y. *et al.* Generation and Fusion of Human Cortical and Medial Ganglionic Eminence Brain Organoids. *Curr. Protoc. Stem Cell Biol.* **47**, (2018).
254. Xiang, Y. *et al.* Fusion of Regionally Specified hPSC-Derived Organoids Models Human Brain Development and Interneuron Migration. *Cell Stem Cell* **21**, 383-398.e7 (2017).
255. Bagley, J. A., Reumann, D., Bian, S., Lévi-Strauss, J. & Knoblich, J. A. Fused cerebral organoids model interactions between brain regions. *Nat. Methods* 2017 147 **14**, 743–751

- (2017).
256. Workman, M. J. *et al.* Engineered human pluripotent-stem-cell-derived intestinal tissues with a functional enteric nervous system. *Nat. Med.* **23**, 49–59 (2017).
257. Schreurs, R. R. C. E., Baumdick, M. E., Drewniak, A. & Bunders, M. J. In vitro co-culture of human intestinal organoids and lamina propria-derived CD4<sup>+</sup> T cells. *STAR Protoc.* **2**, 100519 (2021).
258. Wagar, L. E. *et al.* Modeling human adaptive immune responses with tonsil organoids. *Nat. Med.* **2021 271** **27**, 125–135 (2021).
259. Bar-Ephraim, Y. E., Kretzschmar, K. & Clevers, H. Organoids in immunological research. *Nat. Rev. Immunol.* **2019 205** **20**, 279–293 (2019).
260. Jose, S. S. *et al.* Comparison of two human organoid models of lung and intestinal inflammation reveals Toll-like receptor signalling activation and monocyte recruitment. *Clin. Transl. Immunol.* **9**, e1131 (2020).
261. Miranda, C. C., Fernandes, T. G., Diogo, M. M. & Cabral, J. M. S. Towards Multi-Organoid Systems for Drug Screening Applications. *Bioengineering* **5**, (2018).
262. Ching, T., Toh, Y. C., Hashimoto, M. & Zhang, Y. S. Bridging the academia-to-industry gap: organ-on-a-chip platforms for safety and toxicology assessment. *Trends Pharmacol. Sci.* **42**, 715–728 (2021).

---

# Appendix

## List of figures

<b>Figure 1:</b> Global deaths by cardiovascular disease.....	2
<b>Figure 2:</b> Probability of launch of new active substances by therapeutic area.....	3
<b>Figure 3:</b> Mechanisms of AAV-mediated transgene expression.....	4
<b>Figure 4:</b> Stages of heart development and the contribution of cardiac lineages.....	6
<b>Figure 5:</b> Signaling pathways involved in epicardium-myocardium crosstalk during cardiogenesis.....	8
<b>Figure 6:</b> Applications of human induced pluripotent stem cells (iPSCs) in disease modeling and clinical development.....	11
<b>Figure 7:</b> Reported human organoid systems.....	14
<b>Figure 8:</b> Signaling pathways involved in the generation of human organoids.....	15
<b>Figure 9:</b> Mechanisms of CRISPR/Cas9-mediated gene editing.....	17
<b>Figure 10:</b> Intersecting applications of hiPSCs, organoids and CRISPR/Cas9 gene editing in basic and translational biomedicine.....	19
<b>Figure 11:</b> Modulation of retinoic acid allows enrichment of FHF or SHF CPCs during in vitro cardiac differentiation of hPSCs.....	40
<b>Figure 12:</b> Retinoic acid influences spheroid morphology during 3D cardiac induction of hPSCs.....	42
<b>Figure 13:</b> Retinoic acid influences spontaneous beating behavior during 3D cardiac induction of hPSCs.....	43
<b>Figure 14:</b> Retinoic acid promotes the self-organization of an outer epicardial-like layer during 3D cardiac induction of hPSCs.....	44

<b>Figure 15:</b> The self-organization of myocardial and epicardial layers is reproducible in other hPSC lines after optimization of the starting cell number.....	45
<b>Figure 16:</b> The self-organization of the epicardial layer is dependent on CPC induction in 3D.....	46
<b>Figure 17:</b> Collagen embedding promotes the self-organization of the myocardial and epicardial layers.....	47
<b>Figure 18:</b> Early epicardioids show stepwise upregulation of primitive streak and mesoderm markers.....	48
<b>Figure 19:</b> Epicardioids show spatial segregation of ISL1 <sup>+</sup> NKX2.5 <sup>-</sup> and ISL1 <sup>+</sup> NKX2.5 <sup>+</sup> progenitors around day 5.....	50
<b>Figure 20:</b> ISL1 expression is maintained in the outer layer during epicardioid development..	51
<b>Figure 21:</b> ISL1 expression is maintained in hiPSC-derived epicardial cells.....	52
<b>Figure 22:</b> Early control organoids show different spatial organization of ISL1 <sup>+</sup> NKX2.5 <sup>-</sup> and ISL1 <sup>+</sup> NKX2.5 <sup>+</sup> progenitors than epicardioids.....	54
<b>Figure 23:</b> An ISL1 <sup>+</sup> outer layer is partially formed but not maintained in control spheroids..	55
<b>Figure 24:</b> Time course analysis of key cardiac markers in epicardioids compared to control spheroids.....	56
<b>Figure 25:</b> Time course analysis of (pro)epicardial markers in epicardioids compared to control spheroids.....	57
<b>Figure 26:</b> Time course analysis of juxta-cardiac field (JCF) markers in epicardioids compared to control spheroids.....	58
<b>Figure 27:</b> The epicardial layer is associated with the formation of a subepicardial compact zone showing increased cardiomyocyte proliferation.....	60
<b>Figure 28:</b> Epicardioids show a decrease in calcium transient duration in the subepicardial outer layer.....	62
<b>Figure 29:</b> Control spheroids do not show decreased calcium transient duration in the outer layer.....	63

---

<b>Figure 30:</b> Optical action potential imaging in epicardioid slices via a genetically encoded FRET-based voltage indicator.....	65
<b>Figure 31:</b> Epicardioids show a decrease in action potential duration in the subepicardial outer layer.....	66
<b>Figure 32:</b> hiPSC-derived epicardial cells can differentiate into smooth muscle cells and fibroblasts.....	67
<b>Figure 33:</b> The epicardial layer is a source of fibroblasts and smooth muscle cells.....	68
<b>Figure 34:</b> The epicardial layer is maintained but partially depleted over time.....	69
<b>Figure 35:</b> Endothelial lineage specification is weak in epicardioids compared to control spheroids.....	70
<b>Figure 36:</b> hiPSC-derived epicardial cells can be differentiated into endothelial cells.....	71
<b>Figure 37:</b> Time course scRNA-Seq analysis of epicardioid formation.....	72
<b>Figure 38:</b> UMAP visualization of cell clusters in the complete scRNA-Seq dataset of epicardioid formation.....	74
<b>Figure 39:</b> Expression of markers of mesoderm and endoderm during epicardioid formation.....	76
<b>Figure 40:</b> Expression of markers of first and second heart field in CPC clusters.....	77
<b>Figure 41:</b> Expression of endothelial lineage markers during epicardioid formation.....	78
<b>Figure 42:</b> Expression of ventricular markers during epicardioid formation and long-term culture.....	80
<b>Figure 43:</b> Expression of compact and trabecular markers in cardiomyocyte clusters at day 15 of epicardioid differentiation.....	81
<b>Figure 44:</b> Expression of epicardial lineage markers during epicardioid formation.....	82
<b>Figure 45:</b> Expression of canonical epicardial markers during epicardioid formation.....	83
<b>Figure 46:</b> Expression of juxta-cardiac field (JCF) markers during epicardioid formation ...	85

**Figure 47:** Cell-cell interaction analysis indicates crosstalk between the epicardium and myocardium in epicardioids.....87

**Figure 48:** Endothelin-1 induces the upregulation of hypertrophy markers and ECM genes..89

**Figure 49:** Endothelin-1 induces subepicardial fibroblast activation and ECM deposition....90

**Figure 50:** Reprogramming of hiPSCs from a Duchenne muscular dystrophy patient (DMD $\Delta$ 52) and generation of an isogenic corrected line (DMD $\Delta$ 51-52).....92

**Figure 51:** AAV-mediated CRISPR/Cas9 deletion of exon 51 restores dystrophin expression in DMD $\Delta$ 52 hiPSC-derived cardiomyocytes.....93

**Figure 52:** AAV-mediated somatic gene editing rescues calcium handling defects in DMD $\Delta$ 52 hiPSC-derived cardiomyocytes.....95

---

## List of tables

<b>Table 1:</b> Human pluripotent stem cell lines.....	21
<b>Table 2:</b> qRT-PCR primer sequences.....	27
<b>Table 3:</b> Conditions of single-cell dissociation for scRNA-Seq.....	29
<b>Table 4:</b> Primary antibodies used for immunostaining.....	32
<b>Table 5:</b> Secondary antibodies used for immunostaining.....	32
<b>Table 6:</b> CRISPR RNA nucleotide sequences for the deletion of <i>DMD</i> exon 51.....	35
<b>Table 7:</b> PCR primer sequences.....	37

## List of publications

1. **Meier, A.\***, Zawada, D.\*, *et al.* Epicardioid single-cell genomics uncover principles of human epicardium biology in heart development and disease. (under review) \*Equal contribution
2. Moretti, A.\*, Fonteyne, L.\*, Giesert, F.\*, Hoppmann P.\*, **Meier A.\***, *et al.* Somatic gene editing ameliorates skeletal and cardiac muscle failure in pig and human models of Duchenne muscular dystrophy. *Nat. Med.* **26**, 207–214 (2020). \*Equal contribution
3. Zawada, D.\*, **Meier, A.\***, *et al.* Deep characterization of early cardiovascular progenitors derived from human pluripotent stem cells. (in preparation) \*Equal contribution
4. **Meier, A.\***, Murthi, S. R.\*, Rawat, H.\*, *et al.* Cell cycle defects underlie childhood-onset cardiomyopathy associated with Noonan syndrome. *iScience* **25**, 103596 (2022). \*Equal contribution
5. Poch, C., [...], **Meier, A.**, *et al.* Migratory and anti-fibrotic programs define the regenerative potential of human cardiac progenitors. *Nature Cell Biology* (in press)
6. Zhang F., [...], **Meier, A.**, *et al.* Generation of heterozygous (MRIi028-A) and homozygous (MRIi029-A) MYH10 knockout human iPSC lines. *Stem Cell Research* **57**, 102612 (2021).
7. Zhang F., **Meier, A.**, *et al.* Generation of heterozygous (MRIi003-A-5) and homozygous (MRIi003-A-6) voltage-sensing knock-in human iPSC lines. (under review)

# Acknowledgments

Completing this thesis would not have been possible without the help and encouragement of many different people.

First and foremost, I would like to thank my advisors, Prof. Dr. Alessandra Moretti and Prof. Dr. Karl-Ludwig Laugwitz, for offering me the opportunity to complete my PhD in their group and for providing guidance every step of the way. I am especially grateful to Alessandra for her tireless support of my research and professional development.

I would like to extend my sincere thanks to Prof. Dr. Dieter Saur for his valued guidance as a member of my thesis committee. I am also thankful for fruitful discussions and collaborations with the groups of Prof. Dr. Christian Kupatt and Prof. Dr. Peter Lipp.

I would like to express my sincere gratitude to every member of our lab, past and present, for offering a helping hand whenever needed and for creating a genuinely enjoyable working environment through good and bad times. Special thanks go to Tatjana Dorn, Dorota Zawada, Gianluca Santamaria, Maria Teresa De Angelis, Christine Poch, Hilansi Rawat, Fangfang Zhang, Jessica Kornherr, Monika Nowak-Imialek, Birgit Campbell, Christina Scherb, and Svenja Laue. I also feel lucky to have gone through this journey side by side with Sarah Stenton.

Finally, to the most important people in my life – Marie-Hélène and Gerhard Meier, Elisabeth Meier, Sebastian Blaser, Emil and Felix Meier, Léa Aliperta-Mourissoux and Marina Bally, Alexandros Tsigonias-Dimitriadis – I owe my deepest gratitude. I would not have reached this point without your unwavering support.